SKIN MECHANICS, INTRADERMAL DELIVERY AND BIOSENSING WITH HOLLOW METALLIC MICRONEEDLES

by

Sahan Ranamukhaarachchi

MASc, University of Waterloo (2012)

A THESIS SUBMITTED IN PARTIAL FULFILMENT OF THE REQUIREMENT FOR THE DEGREE OF

DOCTOR OF PHILOSOPHY

in

The Faculty of Graduate and Postdoctoral Studies

(Electrical and Computer Engineering)

THE UNIVERSITY OF BRITISH COLUMBIA

(Vancouver)

April 2017

ABSTRACT

Microneedles (MNs) have gained significant attention over the past decade in drug delivery and biosensing due to their minimally-invasive and less painful nature of use compared to intramuscular/subcutaneous injections, and significant biological benefits. Several fundamental processes enabling MN functionality have not been completely understood, including mechanical interaction between MNs and skin for targeted depth penetration; and precise quantification of fluid delivery in the skin. This thesis presents novel materials, and methodologies for evaluating MN interactions with skin, and investigates the performance of hollow MNs in both intradermal fluid drug delivery and biosensing.

A micromechanical comparison between human skin and porcine skin was performed using to determine their mechanical behavior affecting MN insertions. Stratum corneum (SC) of human skin was significantly stiffer (117 ± 42 MPa) than porcine skin (81 ± 32 MPa), requiring higher force of MN insertion to rupture the SC in human skin (107 ± 17 mN) than porcine skin (96 ± 23 mN). An artificial mechanical skin model was developed layer-by-layer to simulate tough human skin (MN insertion force 162 ± 11 mN) and to study the dynamics of MN insertion. Key factors that affected MN insertions into skin, including velocity of impact and total energy delivered to the skin, were identified.

ID fluid delivery by hollow MNs was assessed using a novel method involving the low-activity radiotracer technetium-99m pertechnetate ($^{99m}TcO_4^-$). Its delivery allowed accurate quantification of fluid delivered into the skin, back-flowed to the skin surface, and total fluid ejected from the

syringes via ID devices with sub-nanoliter resolution. Hollow MNs performed more accurate ID injections than conventional needles (93% vs. 69-87% of fluid per 0.1 mL injection volume).

A MN-optofluidic biosensing platform capable of eliminating blood sampling was developed with MNs that can access dermal interstitial fluid that contains numerous drugs at concentrations comparable to blood. The MN lumen was functionalized to collect, trap and detect drugs in 0.6 nL of sample. The optofluidic components provided specific high-sensitivity absorbance measurements for drug binding using enzyme-linked assays. Streptavidin-horseradish peroxidase (LoD = 60.2 nM) and vancomycin (LoD = 84 nM) binding validated this point of care system.

PREFACE

The research presented in this dissertation was carried out primarily at the University of British Columbia, Canada in the Stoeber Laboratory in the Department of Electrical and Computer Engineering, and the Häfeli Laboratory in the Faculty of Pharmaceutical Sciences, under the co-supervision of Dr. Boris Stoeber and Dr. Urs O. Häfeli. A portion of this research was conducted at the Laboratory for Micro- and Nanotechnology in the Paul Scherrer Institute (PSI), Switzerland under the co-supervision of Dr. Victor Cadarso and Dr. Celestino Padeste.

Chapter 1 of this dissertation, conducted by myself under the supervision of Stoeber and Häfeli, provides the research motivation, relevant literature review, and objectives of this dissertation.

The section on microneedle-biosensing devices was prepared for publication as a book chapter:

> **Ranamukhaarachchi S.A.,** Häfeli U.O. Therapeutic drug and biomolecule monitoring potential for microneedle technologies in Microneedling in Clinical Practice, edited by B. Stoeber, R. K. Sivamani, and H. I. Maibach, to be published by CRC Press, 2017.

Chapter 2, conducted primarily by myself under the supervision of Stoeber and Häfeli, is based on the work published in the following journal paper:

> **Ranamukhaarachchi S.A.**, Lehnert S., Ranamukhaarachchi S.L., Sprenger L., Schneider T., Mansoor I., Rai K., Häfeli U.O., Stoeber B. A micromechanical comparison of human and porcine skin before and after preservation by freezing for medical device development. Scientific Reports 6, Article number: 32074 (2016) doi:10.1038/srep32074.

It presents a comprehensive micromechanical study comparing freshly-excised and previously-frozen human and porcine skins using a conventional mechano-analytical method (microindentation) and microneedle insertions. I received testing support from Lehnert, Sprenger, and Schneider; statistical support from Ranamukhaarachchi; device fabrication support from Mansoor; and skin handling support from Rai.

Chapter 3, conducted primarily by myself under the supervision of Stoeber and Häfeli, is based on the work published in the following journal paper:

> **Ranamukhaarachchi S.A.,** Schneider T., Lehnert S., Sprenger L., Campbell J.R., Mansoor I., Lai J.C., Rai K., Dutz J., Häfeli U.O., Stoeber B. Development and Validation of an Artificial Mechanical Skin Model for the Study of Interactions between Skin and Microneedles. Macromolecular Materials and Engineering. 2016 Mar 1;301(3):306-14.

It presents the development and validation of an artificial mechanical skin model to facilitate the development of percutaneous medical devices, such as microneedles. I received testing support from Schneider, Lehnert, and Sprenger; statistical support from Campbell; device fabrication support from Mansoor; and skin handling support from Lai, Rai, and Dutz.

Chapter 4, conducted primarily by myself under the supervision of Stoeber and Häfeli, was prepared for submission to a journal:

> **Ranamukhaarachchi S.A.,** Jayatilake H., Häfeli U.O., Stoeber B. Determining the factors affecting dynamic insertion of microneedles into skin (*in preparation*).

This chapter presents a study conducted to identify the significant factors that affect the dynamic nature of microneedle insertions. I received support from Jayatilake on data analysis to complete this study.

Chapter 5 was conducted primarily by myself under the supervision of Stoeber and Häfeli, and is based on a manuscript that was submitted to a journal:

> **Ranamukhaarachchi S.A.,** Esposito T.V., Raeiszadeh M., Stoeber B., Häfeli U.O. Precise measurement of intradermal fluid delivery using a low activity technetium-99m pertechnetate tracer (*in preparation*).

This chapter presents a novel method that was developed and validated to determine the intradermal (ID) fluid delivery potential of injection devices, including hollow microneedles. Esposito assisted with the preparation of $^{99m}TcO_4^-$ and animals for injections, while Raeiszadeh assisted with preparation of devices and performing the injections.

Chapter 6 was conducted primarily by myself under the supervision of Cadarso and Padeste, and is based on a manuscript submitted to a journal:

> **Ranamukhaarachchi S.A.**, Padeste C., Häfeli U.O., Stoeber B., Cadarso V.J. Design considerations of a hollow microneedle-optofluidic biosensing platform incorporating enzyme-linked assays (submitted on February 8, 2017).

The work presented in this chapter focuses on modifying and integrating hollow microneedles with an optofluidic sensing system for therapeutic drug monitoring using enzyme-linked assays. Häfeli and Stoeber provided advice to guide the experimental work.

Chapter 7 was conducted primarily by myself under the supervision of Cadarso and Padeste, and is based on the work published in the following journal:

> **Ranamukhaarachchi S.A.**, Padeste C., Dübner M., Häfeli U.O., Stoeber B., Cadarso V.J. Integrated hollow microneedle-optofluidic biosensor for therapeutic drug monitoring in sub-nanoliter volumes. Scientific Reports 6, Article number: 29075 (2016) doi:10.1038/srep29075.

In this chapter, the microneedle-optofluidic biosensor is further modified and assessed for its capability to analyze vancomycin, a therapeutically monitored drug, using a competitive drug binding scheme inside the sub-nanoliter volume of a single microneedle. Häfeli and Stoeber provided advice to guide the experimental work.

Chapter 8 summarizes the previous chapters and proposes future work to be done to improve the presented microneedle technologies, and make them available for commercial medical applications.

TABLE OF CONTENTS

ABSTRACT ..... **ii**

PREFACE ..... **iv**

TABLE OF CONTENTS ..... **viii**

LIST OF TABLES ..... **xi**

LIST OF FIGURES ..... **xiii**

LIST OF VARIABLES ..... **xv**

LIST OF ABBREVIATIONS ..... **xvii**

ACKNOWLEDGEMENTS ..... **xix**

DEDICATION ..... **xx**

1. INTRODUCTION **1**

1.1. Research Motivation 1

1.2. Background Information 3
1.2.1. Microneedle Applications 3
1.2.2. Structure and Mechanical Properties of Human Skin 22
1.2.3. Skin Fracture 28
1.2.4. Human Skin Substitutes 30
1.2.5. Assessing Intradermal Delivery 37

1.3. Gaps in Current Knowledge 40

1.4. Objectives of the Dissertation 42

2. MICROMECHANICAL ANALYSIS OF BIOLOGICAL SKINS FOR MICRONEEDLE INSERTION ASSESSMENT **43**

2.2. Materials and Methods 44
2.2.1. Biological Skin Preparation 44
2.2.2. Micro-indentation of Skin Samples 45
2.2.3. Microneedle Insertions 46

2.3. Results and Discussion 47
2.3.1. Young's Modulus of the Stratum Cornea 50
2.3.2. Young's Modulus of Skin Composites 52
2.3.3. Microneedle Insertion Profiling 53

2.4. Conclusions 59

3. DEVELOPMENT OF AN ARTIFICIAL MECHANICAL SKIN MODEL FOR MICRONEEDLE INSERTION ASSESSMENT .. **61**

3.1. Experimental Section 62
3.1.1. Biological Skin Preparation 62

3.1.2. Artificial Skin Preparation....62
3.1.3. Micro-indentation of Skin Samples....62
3.1.4. Tensile Testing of the Stratum Corneum....63
3.1.5. Microneedle Insertions Profiling....63
3.2. Results and Discussion....63
3.2.1. Stratum Cornea of Biological Skins....63
3.2.2. Stratum Corneum of the Artificial Skin Model....68
3.2.3. Multi-layered Skin Composites....69
3.2.4. Microneedle Insertion Profiling....71
3.3. Conclusions....74
4. KEY FACTORS INFLUENCING DYNAMIC MICRONEEDLE INSERTIONS....75
4.1. Materials and Methods....75
4.1.1. Microneedles and Skin Model....75
4.1.2. Microneedle Insertion Setups....76
4.1.3. Dynamic Microneedle Insertion Procedure....77
4.1.4. Data Processing and Analysis....78
4.1.5. Microneedle Insertion Experiments....79
4.2. Results and Discussion....81
4.2.1. Microneedle Insertion Profile....81
4.2.2. Factors Affecting the Dynamic Insertion of a Single Microneedle....83
4.2.3. Influence of Momentum....85
4.2.4. Influence of Microneedle Geometry....86
4.2.5. Dynamic Insertion of Microneedle Arrays....88
4.3. Conclusions....91
5. PRECISE MEASUREMENT OF INTRADERMAL FLUID DELIVERY....92
5.1. Materials and Methods....92
5.1.1. Materials....92
5.1.2. Ex Vivo Skin Injections....93
5.1.3. In Vivo Skin Injections....95
5.1.4. Measurement and Data Analysis....95
5.3. Results and Discussion....98
5.3.1. Device Performance Ex Vivo....98
5.3.2. Device Performance In Vivo....100
5.3.3. Comparison of Methodologies....101
5.4. Conclusions....104
6. DESIGN AND DEVELOPMENT OF A HOLLOW MICRONEEDLE-OPTOFLUIDIC BIOSENSOR INCORPORATING ENZYME-LINKED ASSAYS....106
6.1. Materials and Methods....106
6.1.1. Materials....106
6.1.2. Microneedle Surface Functionalization....107
6.1.3. 3,3’5,5’-Tetramethylbenzidine (TMB) Assay....109
6.1.4. Preparation of Masters and Molds for the Optofluidic Device....109
6.1.5. Integrating the Microneedle to Optofluidic Sensing Device....111

6.1.6. Microneedle-Optofluidic Device Performance 112
6.2. Results and Discussion 113
6.2.1. Surface Functionalization 113
6.2.2. Optofluidic Device Optimization 115
6.2.3. Performance of the Integrated Microneedle-Optofluidic Biosensor 118
6.2.4. Biosensing in the Microneedle Lumen 119
6.2.5. Additional Utility of the Biosensor 122
6.3. Conclusions 123
7. THERAPEUTIC DRUG MONITORING WITH HOLLOW MICRONEEDLE-OPTOFLUIDIC BIOSENSOR 125
7.1. Materials and Methods 126
7.1.1. Materials 126
7.1.2. Microneedle Fabrication 127
7.1.3. 3,3'5,5'-Tetramethylbenzidine Assay 127
7.1.4. Microneedle Surface Functionalization 128
7.1.5. Performance of the Microneedle-Optofluidic Sensor 130
7.2. Results 132
7.2.1. Vancomycin Binding Assay on Microneedle Base Surface 132
7.2.2. Competitive Vancomycin Binding Assay in Extremely Low Volume Microneedle Lumens 134
7.3. Discussion 135
7.4. Conclusions 140
8. SUMMARY AND FUTURE WORK 142
8.1. Summary 142
8.2. Future Work 143
8.2.1. Improvements to the Artificial Skin Model 143
8.2.2. Optimizing Microneedle Design and Insertion 144
8.2.3. Optimize Intradermal Delivery Using Hollow Microneedles 144
8.2.4. Clinical Assessment of Intradermal Delivery Using Microneedles 144
8.2.5. Clinical Assessment of the Microneedle-Optofluidic Biosensing System 145
REFERENCES 146
APPENDICES 160
Appendix A – Statistical Data Supporting Chapter 2 160
Appendix B – Skin Preparation and Testing Method in Chapter 3 166
B1 - Biological Skin Preparation 166
B2 - Tensile Testing of the Stratum Corneum 167
B3 - Statistical Analysis 168
Appendix C – Methods and statistical data supporting Chapter 4 169
C1 - MATLAB Code for Image Processing 169
C2 - Statistical Analysis 172
Appendix D – Optimization of Microneedle-Optofluidic Biosensor Supporting Chapter 7 173

LIST OF TABLES

Table 1. Published Young's moduli for human and porcine stratum corneum, dermis, and full-thickness skin. ... 27

Table 2. Anatomical and compositional differences between human and porcine skin. 31

Table 3. Effect of skin source, state, and relative humidity on the Young's modulus of the stratum corneum, epidermis/dermis composite, and full-thickness skin determined by microindentation analysis of fresh and frozen human and porcine skin layers. 50

Table 4. Effect of skin type, state, and relative humidity on the stiffness (N m^{-1}), force at insertion (N), and displacement at insertion (µm) during microneedle insertion into fresh and frozen human and porcine skins. 55

Table 5. Design of experiment to assess the impact of MN tip outer diameter on the insertion of a single microneedle with a 60, 100, and 120 µm tip OD 80

Table 6 Design of experiment to assess the impact of momentum on the insertion of a single microneedle with a 100 µm tip OD 80

Table 7. Design of experiment to assess the impact of array size on MN insertion with single (1-MN), six (6-MN), and nineteen (19-MN) microneedle arrays consisting of projections with 100 µm tip OD 81

Table 8. Effect of energy of the system (E_o) and the microneedle tip area on the force and energy required to insert a single microneedle into skin..... 87

Table 9. Effect of energy of the system (E_o) and the number of microneedles in an array on the force and energy required to insert a single microneedle into skin 89

Table 10. Comparison of volume delivery efficiency of intradermal delivery devices 103

Table 11. Performance summary for the microneedle optofluidic biosensor and the conventional biosensing assay..... 122

Table 12 Sources of variation, degree of freedom, and mean squares for the stratum corneum, epidermis/dermis composite, and full-thickness skin obtained from the analysis of variance (ANOVA) of microindentation results for human and porcine skin layers 162

Table 13. Statistically significant interactions between treatments (skin source, state, and relative humidity) influencing the out-of-plane Young's modulus of skin layers determined by microindentation analysis at a 95% confidence interval 163

Table 14. Sources of variation, degree of freedom, and mean squares for the stiffness (N m^{-1}), force at insertion (N), and displacement at insertion (μm) obtained from the analysis of variance (ANOVA) of microneedle insertion results for human and porcine skin layers..... 164

Table 15. Statistically significant interactions between treatments (skin source, state, and relative humidity) influencing the force of microneedle insertion into skin determined by microneedle insertion profiling at a 95% confidence interval 165

Table 16. Assessment of the microneedle tip outer diameter and energy on force of insertion (F_{ins}) and energy to insert (E_{ins}) 172

Table 17. Assessment of the impact of microneedle projections and energy on force of insertion (F_{ins}) and energy to insert (E_{ins}) 172

LIST OF FIGURES

Figure 1. Cross-sectional view of human skin 1

Figure 2. Common strategies for drug delivery using microneedles 4

Figure 3. Arrays of solid and hollow out-of-plane microneedles 5

Figure 4. Hollow metal microneedle fabrication process 6

Figure 5. A typical therapeutic drug monitoring profile showing the narrow therapeutic window 8

Figure 6. Concentration-time profiles for glucose and vancomycin in blood and interstitial fluid in rabbits 10

Figure 7. Hydrogel-forming microneedles for extraction of analytes from ISF 13

Figure 8. Bicomponent microneedle electrode system consisting of integrated hollow and solid microneedle arrays for glutamate monitoring 18

Figure 9. Continuous glucose monitoring biosensor 21

Figure 10. Continuous glucose monitoring by a microneedle biosensor compared to reference blood glucose ... 21

Figure 11. Structure of the human living epidermis 23

Figure 12. Stress versus strain relationship of skin resulting in a *J*-shaped curve 25

Figure 13. Tensile force versus elongation profiles for human stratum corneum 26

Figure 14. Penetration mechanism of soft solids by sharp-tipped needle and a flat-tipped needle 29

Figure 15. Basic principles and process of skin tissue engineering 34

Figure 16. Soft lithography process of fabricating an artificial mechanical skin model from silicone rubber 37

Figure 17. Microindentation of skin layers 49

Figure 18. Microneedle insertion profiling in skin layers 54

Figure 19. Microindentation of skin layers to determine their out-of-plane Young's modulus for artificial skin model development 66

Figure 20. Tensile testing of stratum cornea to determine their in-plane mechanical properties 67

Figure 21. Microneedle insertion profiling on human, porcine, and artificial skins to compare mechanical characteristics 73

Figure 22. Dynamic microneedle insertion setup 77

Figure 23. Dynamic microneedle insertion steps 78

Figure 24. Microneedle insertion force versus displacement generated from an experiment using a spring 82

Figure 25. Factors influencing the insertion of a single microneedle into skin 84

Figure 26 Impact of momentum on the insertion of a single microneedle into skin 85

Figure 27. Impact of microneedle tip area on skin insertion 88

Figure 28. Impact of the number of microneedles in an array on skin insertion 90

Figure 29. Fluid delivery and measurement methodology 97

Figure 30. Comparison of ID fluid delivery methods ex vivo for successful fluid delivery and fluid backflow resulting in wastage 99

Figure 31. In vivo delivery of $^{99m}TcO_4^-$ using ML1 single microneedle devices in Sprague Dawley rats 104

Figure 32. Microneedle surface functionalization 114

Figure 33. Conceptualization of the microneedle-optofluidic biosensor and its components 117

Figure 34. Optimization of the optofluidic device 118

Figure 35. Detection of Sav-HRP in microliter volumes in the microneedle-optofluidic biosensor 121

Figure 36. Utility of the microneedle-optofluidic sensor as an enzyme sensor 123

Figure 37. The chemical reaction scheme for the detection of vancomycin in low volume samples inside microneedle lumens 126

Figure 38. Process of conducting the biosensing process in the microneedle-optofluidic device 132

Figure 39. Detection of vancomycin in microliter-to-sub nanoliter volumes in the microneedle-optofluidic biosensor 133

Figure 40. Human stratum cornea separated from full-thickness skin specimens by mild heat treatment 167

Figure 41. Absorbance of the TMB model-dye (methyl green) in the optofluidic sensing system as a function of optical waveguide length and width; and absorbance of the TMB end-product at 635 nm due to Vancomycin-HRP activity in the microneedle base surfaces 173

LIST OF VARIABLES

$A_{Backflow}$	Radioactivity backflow
A_p	Projected area
A_{Skin}	Radioactivity from the skin
A_{Total}	Total radioactivity
D	Displacement
D_{ins}	Displacement at insertion
E	Young's modulus
E_{ED}	Young's modulus of the epidermis/dermis
E_{FT}	Young's modulus of the full-thickness skin
E_i	Young's modulus of indenter tip
E_{ins}	Energy required for skin fracture
E_k	Kinetic energy
$E_{k,imp}$	Kinetic energy at impact
E_o	Initial total energy of the system
E_p	Potential energy
E_r	Reduced Young's modulus
E_s	Young's modulus of sample
E_{SC}	Young's modulus of the stratum corneum
E_T	In-plane Young's modulus
ε_i	Given strain
ε_T	True strain
F	Force
F_{ins}	Force of insertion
k	Spring constant
m	Mass
S	Stiffness
$V_{backflow}$	Volume backflow
ν_i	Poisson's ratio of indenter tip
v_{imp}	Velocity at impact
ν_s	Poisson's ratio of sample
V_{skin}	Volume in the skin
V_{Total}	Total volume
x	Spring compression distance

σ_i	Given stress
σ_T	True stress

LIST OF ABBREVIATIONS

$^{99m}TcO_4^-$	Technetium-99m pertechnetate
AcKAA	Acetyl-lysine-d-alanine-d-alanine
AMSM	Artificial mechanical skin model
ANOVA	Analysis of variance
AU	Absorbance unit
AUC	Area under curve
BSA	Bovine serum albumin
CB	Carbon black
CGM	Continuous glucose monitoring
CV	Coefficient of variability
DRIE	Deep reactive ion etching
ED	Epidermal/dermal skin composite
ELISA	Enzyme-linked immunosorbent assay
FAA	Federal Aviation Administration
FT	Full-thickness skin composite
H_2O_2	Hydrogen peroxide
HPLC	High pressure liquid chromatography
HRP	Horseradish peroxidase
ICRP	International Commission on Radiological Protection
ID	Intradermal
ISF	Interstitial fluid
ISO	International Standards Organization
kBq	Kilobecquerel
LC	Langerhans cells
LCMS	Liquid chromatography/mass spectrometry
LoD	Limit of detection
LSCM	Laser scanning confocal microscopy
LSD	Least significant difference
MEMS	Microelectromechanical systems
MN	Microneedle
MPA	Microprojection arrays
mPEG	methoxy polyethylene glycol
MSS	Microneedle sensor system
NCRP	National Council on Radiation Protection and Measurements
NO	Nitric oxide
NS	Not significant

OD	Outer diameter
OFD	Optofluidic
OGTT	Oral glucose tolerance test
PBS	Phosphate buffered saline
PCHIP	Piecewise Cubic Hermite Interpolating Polynomial
PDMS	Polydimethylsiloxane
PEG	Polyethylene glycol
PMA	Propylene glycol monomethyl ether acetate
PMMA	Poly(methyl methacrylate)
RH	Relative humidity
Sav	Streptavidin
Sav-HRP	Streptavidin-horseradish peroxidase conjugate
SC	Stratum corneum
SD	Standard deviation
SNR	Signal to noise ratio
TDM	Therapeutic drug monitoring
TMA	Thermomechanoanalyzer
TMB	3,3’5,5’-tetramethylbenzidine
UTS	Ultimate tensile strength
UV	Ultraviolet
VAN	Vancomycin
VAN-HRP	Vancomycin-horseradish peroxidase conjugate

ACKNOWLEDGEMENTS

I would like extend my utmost gratitude to Dr. Boris Stoeber and Dr. Urs Häfeli for providing the opportunity to pursue my doctoral research, and for their constant support, guidance, and patience over the past several years. The support, dialog, and collaboration with colleagues from both the Stoeber and Häfeli Labs facilitated my research work, but more importantly led to invaluable friendships. Special thanks go to Iman Mansoor and Maziyaar Jalaal from the Stoeber Lab; and Thomas Schneider, Lisa Sprenger, Tullio Esposito, and Christian Buchwalder from the Häfeli Lab.

I would like to thank Dr. Celestino Padeste and Dr. Victor Cadarso for hosting me, providing the opportunity to conduct exciting research, and for their unprecedented support and guidance. Special thanks go to Matthias Dübner, Michael Gerspach, and other staff at the Paul Scherrer Institute.

I would like to thank my doctoral committee members – Dr. Karen Cheung, Dr. Jan Dutz, and Dr. Peter Cripton; Kristie Henrikson (ECE); Mario Beaudoin and Alina Kulpa (cleanroom); Gethin Owen (CHTP); and John Jackson (Pharmaceutical Sciences) for their time and support.

I am extremely grateful for the friendships with and encouragement from Jonathon Campbell, Jacob Gordon, Moe Wehbe, Primal Wijesekera, Hasitha Jayatilake, Dinesh Aluthge, Thamali Kariyawasam, Keheliya Gallaba, and Mehrsa Raeiszadeh. I am also thankful to Microdermics and entrepreneurship@UBC for encouraging the commercialization exploration of my research.

I am deeply indebted to my amazing supporting team at home – ammi, thaaththi, amma, appachchi, aiya, akki, nangi, and nanga. Your words of encouragement, constant support, utmost patience, and compassion to me during the past years have helped me grow as a person and succeed at my endeavors. Nanga, thank you for talking and listening to me every day, and allowing me to share my ups and downs with you throughout my studies. Finally, I am most thankful to my partner and best friend, Mayu, who was always by myside, without whom none of this would have been possible.

Lastly, I would like to thank the Vanier Canada Graduate Scholarships program, Michael Smith Foreign Study Supplement program, and the Collaborative Health Research Projects (CHRP) program with the Natural Sciences and Engineering Research Council of Canada and the Canadian Health Research Institute for financial support.

DEDICATION

To my wife, sisters, and parents.

1. INTRODUCTION

1.1. Research Motivation

The development of vaccines and therapeutics for prevention and treatment of infectious diseases has had an enormous impact on human health. The discovery and improvement of vaccines and vaccine delivery technologies to induce immune responses in humans is continually necessary to combat the threats posed by emerging pathogens. Most vaccines are currently administered via hypodermal injections into the muscle or under the skin, although the immune responses to vaccines can be greatly improved by their administration into the skin or more exactly the epidermis and dermis (Figure 1) without inducing potential toxic effects [1].

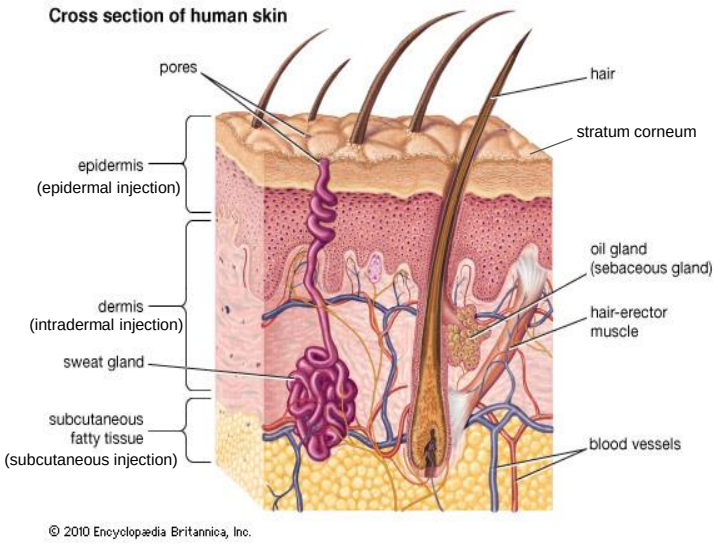

Figure 1. Cross-sectional view of human skin [2]. With permission from Encyclopedia Britannica.

The skin forms the first line of natural defense by humans to mechanical trauma and biological attack. The stratum corneum (SC) layer of skin provides a tough, mechanical barrier from external

stress, while the viable epidermis and dermis contain immune cells to engage with harmful subjects to orchestrate inflammation and immune responses. For therapeutics and biologics, targeted intradermal (ID) delivery into the dermis can potentially improve bioavailability of the drugs in the blood stream, due to the higher vasculature of the skin and efficient lymphatic drainage. Therefore, the need for ID vaccine and therapeutic delivery methods is vital.

Various commercially available products, such as skin adhesive patches that release biomolecules to the skin's surface for passive diffusion into the skin through the SC, are widely used for drug and vaccine delivery to the skin. A major challenge with ID delivery using skin patches is limited permeability of biomolecules through the SC into the subsequent layers due to its strong barrier properties [3]. Among many means tested and developed to enhance drug penetration through the SC, none have shown the potential presented by microneedles (MNs) [4-12]. Being sub-millimeter needle-like structures, MNs overcome the skin barrier by creating mechanical pathways to bypass the SC and provide direct routes for ID drug delivery that are non-invasive, less or not painful, and potentially self-administrable. MNs can be microfabricated in various designs using silicon [13, 14], polysilicon [9, 15], metal [16], and polymers [5, 17-19]. However, there are many significant drawbacks to the commercialization of MNs for drug delivery and biosensing applications, including the high cost of MN fabrication, risk of MN fracture during or after insertion, and leaking of fluid upon improper insertion. Many of these limitations pertain to the lack of knowledge of skin mechanics and MN-to-soft tissue interactions during MN insertions into skin for ID delivery and should be thoroughly investigated. Understanding MN-to-soft tissue interactions in detail will not only facilitate the development of MN devices for repeatable and successful ID delivery of fluids, but also provide access to biological fluids in the skin, such as dermal interstitial fluid (ISF)

[20], which can be used for therapeutic drug monitoring (TDM) and biosensing applications in minimally-invasive ways. A significant number of TDM drugs demonstrate a correlation drug concentrations between blood and ISF [21-23]. Thus, TDM in ISF using MNs has the potential to transform current practices, and provide attractive solutions to health care professionals and patients.

1.2. Background Information

This section presents introductions and background information to important concepts, materials, and methods to this dissertation.

1.2.1. Microneedle Applications

1.2.1.1. Intradermal Drug Delivery

A recent and promising method to enhance drug permeation through skin is the use of MNs to create mechanical pathways for drug and vaccine delivery across the SC to the epidermal and dermal regions of the skin. MNs are sub-millimeter needle-like structures with high aspect ratios. They can be categorized by arrangement (in-plane vs. out-of-plane), structural differences (solid vs. hollow, sharp-tipped vs. flat-tipped), materials (polymers, metals), and microfabrication techniques. The pores created on the skin surface by MNs are significantly larger than drug molecules, but smaller than holes created by hypodermic needles. Therefore, they would allow molecules to readily diffuse through the SC to the desired depths within or beyond the skin layers, while being safe for clinical use [24]. Other advantages of MNs include relatively higher flux of macromolecules and vaccines, lack of skin irritation, pain-free insertion, and possibility for mass production.

MNs and their designs have been greatly varied and exploited for ID delivery applications in minimally invasive manners. Four of the predominantly used methods for drug delivery using MNs are illustrated in Figure 2 [25].

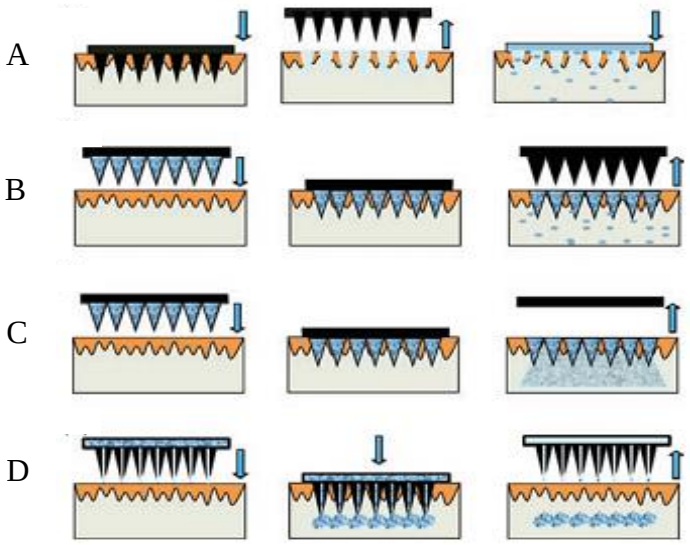

Figure 2. Common strategies for drug delivery using microneedles. (A) Solid microneedles create micro-pores in skin prior to topical drug/patch application; (B) coated solid microneedles to transfer drugs into skin; (C) dissolving solid polymeric microneedles ; and (D) hollow microneedles arrays to inject drugs and extract fluids [25]. The orange layer represents the epidermis of skin, including the stratum corneum.

Insertion and retraction of solid MNs create micro-pores in the skin (Figure 2A). Subsequent application of drug-loaded transdermal patches or topical ointments to the MN-treated site of the skin allows for enhanced drug permeation through the SC via the mechanical channels. A more recent derivation of this approach is the coating of the surface of solid MNs with a drug-loaded polymer solution (Figure 2B), which upon insertion is released from the MN surface and delivered as a bolus dose intradermally. Dissolving MNs (Figure 2C) are made with the drug-carrying polymers, and are subjected to dissolution or biodegradation after insertion and upon contact with

the skin interstitial fluid. Finally, hollow MNs (Figure 2D) allow transfer of biomolecules carried with a fluid into desired depths in the skin in a continuous and controlled manner; thereby allowing active drug delivery. They can also be used in the extraction of biological fluids, such as interstitial fluid [26].

MNs have been fabricated using a variety of materials, including silicon, metals, glass, and polymers; and microfabrication technologies, including deep reactive ion etching (DRIE), solvent casting, metal electrodeposition, and hot embossing. A few examples of solid and hollow MNs are shown in Figure 3.

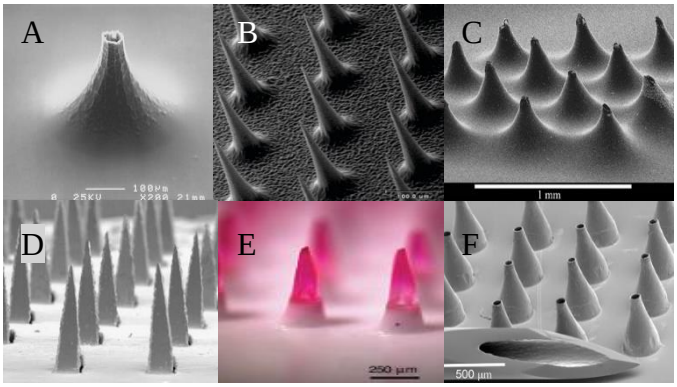

Figure 3. Arrays of solid and hollow out-of-plane microneedles. (A) Hollow silicon microneedles by deep reactive ion etching [14]; (B) solid silicon microneedles [27]; (C) clay-reinforced polyimide microneedle array by solvent casting [18]; (D) solid stainless steel microneedles by laser cutting; (E) dissolving polymeric microneedles [12]; (F) laser-machined metallic microneedle array [28].

1.2.1.2. Hollow Metallic Microneedles

In this dissertation, only hollow nickel MNs are utilized, which are fabricated using a metal electrodeposition process according to Mansoor et al. (2013) (Figure 4) [16].

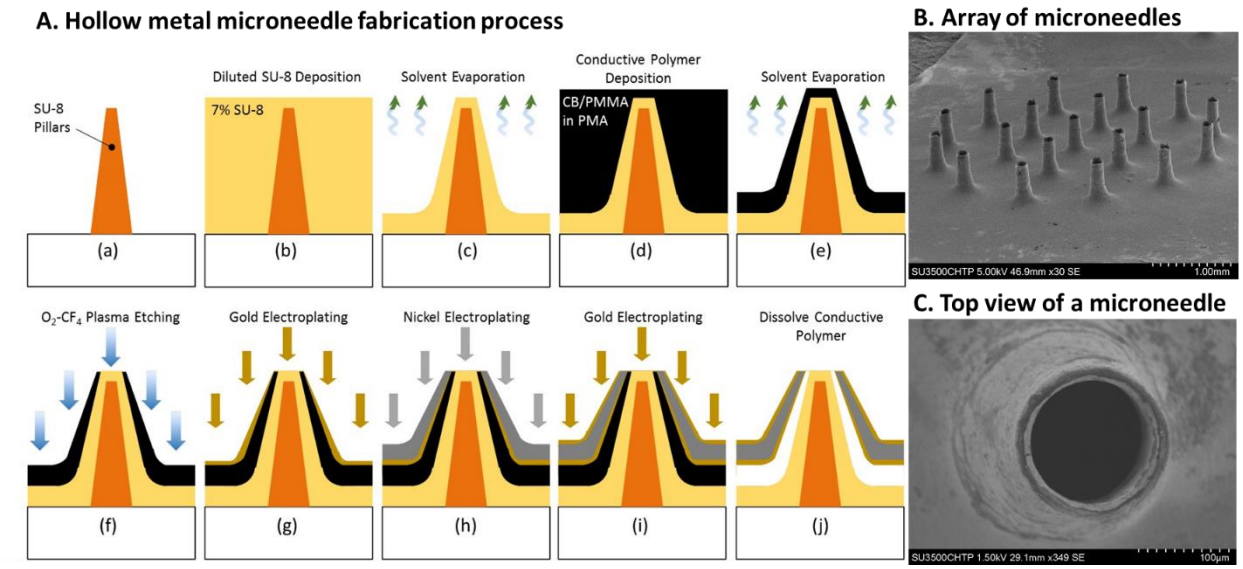

Figure 4. Hollow metal microneedle fabrication process (A) and resulting microneedles (B-C). (a) Fabrication of a mold consisting of a single or an array of cone shaped pillars (created through backside exposure of SU-8); (b) deposition of structural supporting polymer (diluted SU-8); (c) solvent casting the dilute SU-8 on the pillars; (d) deposition a conductive polymer consisting of a mixture of poly(methyl methacrylate) (PMMA) and carbon black (CB); (e) evaporation of solvent; (f) removal of the polymer coating on top of the pillars by O_2/CF_4 plasma etching or another methodology; (g-i) electrodeposition of metals on the conductive polymer coating; (j) dissolution of the conductive polymer and separation of the microneedle array from the pillars.

Briefly, arrays of 400-600 μm cylindrical and tapered pillars that maintain a volcano-shaped base were fabricated on a four-inch diameter borosilicate substrate (thickness of 500 μm) from SU-8 2150 (Microchem, MA, USA). The ultraviolet (UV) exposure of the SU-8 was performed through the glass substrate (backside exposure) to obtain tapered pillars, as shown in Figure 4a, which constituted the mold structure and defined the needle lumens. A conductive polymer layer, comprised of poly(methyl methacrylate) (PMMA; 25 kDa MW; Polysciences, PA, USA) and Vulcan XC72R carbon black (CB; 150 nm particle size; Cabot, MA, USA) mixed in propylene glycol monomethyl ether acetate (PMA) to obtain a total solids content of 7.5 wt%. Prior to the

conductive polymer deposition, the mold was plasma treated to clean the surface, improve adhesion, and decrease the contact angle. A volume of 155 μL was deposited on the mold, which was heated at 85 ºC for 15 minutes to cast the PMMA/CB composite (Figure 4 d-e). Then, the device was subjected to O_2/CF_4 plasma etching (O_2: 80 sccm, CF_4: 20 sccm, pressure: 500 mTorr, temperature: 25ºC, power: 200 W, and duration: 200 s) to open the MN tips, followed by electroplating with nickel and gold. During the electroplating step, the MN mold with the conductive polymer layer was used as the cathode, while a four-inch diameter pure nickel piece was used as the anode, positioned parallel to each other approximately 2 cm apart. The nickel electroplating was performed at a constant current density of 5 mA cm^{-2} for 180 min to obtain a 20 μm wall thickness on the microneedle. Post-electroplating lift-off was performed by dissolving the underlying conductive polymer layer to separate the electroplated nickel from the SU-8 pillars to produce hollow nickel MNs. Several modifications made to the process developed by Mansoor et al. (2013) included replacing Figure 4f with deposition of a metal conductive layer on the CB/PMMA layer, and depositing a non-conductive polymer on the tip of the MN prior to electroplating.

1.2.1.3. Biosensing and Therapeutic Drug Monitoring

Emerging clinical biosensor concepts promise significant improvements to TDM, disease diagnostics, and treatment planning. Over the past decades, many clinical biosensing systems have been developed and commercialized for TDM (i.e., glucose monitoring in diabetic patients [29]), early detection of disease (i.e., HIV [30] and malaria [31]) bodily changes (i.e., pregnancy [32]), and for other diagnostics applications, as summarized by [33]. TDM is the process of measuring the concentration of biomolecules, often active pharmaceutical ingredients, in blood that, with

proper interpretation, will influence therapy and future medical procedures [34]. TDM is of utmost importance when drug candidates with a narrow therapeutic window is administered (Figure 5), since outside of this window, a patient could be over-dosed to cause potentially life-threatening side-effects or under-dosed to provide ineffective therapy [35]. Similarly, there are biomolecules that become available in the blood after intake with food and beverages, such as glucose, that are not therapeutic drugs, but rather metabolic and/or disease causing agents that need to be monitored. Ability for continuous monitoring of such biomolecules provide information for timely and effective treatment to ensure health and wellbeing of patients [36]. Elevated levels of certain biomolecules and analytes, such as nitric oxide, can indicate the occurrence of physiological changes in the human body, like development of cancer; and monitoring of such biomolecules will lead to early diagnosis of health issues for medical attention and treatment [37-39].

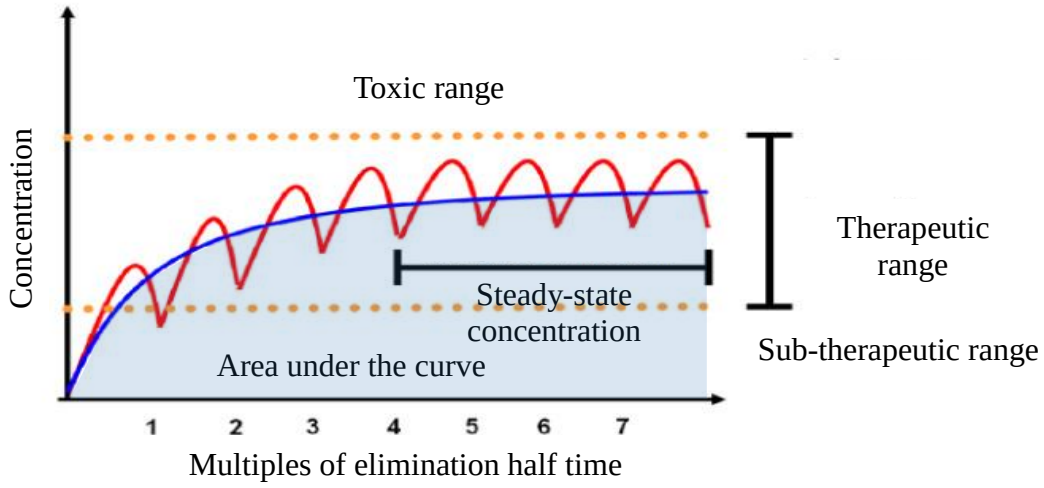

Figure 5. A typical therapeutic drug monitoring profile showing the narrow therapeutic window [35]. The red line indicates the blood concentration profile of the drug during multiple dosing, while the ideally provided blood concentration required for therapy is given in blue. The total dose delivered by the blue curve is given as the light blue area and is called the area under the curve (AUC).

TDM and diagnostic testing are conventionally conducted in blood samples withdrawn from patients at regular intervals to guide treatments [40]. Blood sampling utilizes an invasive needle or another sharp device, such as a lancet, to access blood for extraction from capillaries or veins. At least 100 µL of whole blood is required at a time for most TDM assessments [41]. Whole blood typically requires processing, such as centrifugation to extract serum, before analysis is performed. Most analytes in the blood are separated and quantified using expensive and time-consuming laboratory processes, including chromatography and mass spectrometry techniques like liquid chromatography/mass spectrometry (LCMS) [40]. Delays are observed from these involved TDM analysis techniques and present significant opportunities to improve TDM and diagnostics procedures in medical practice. As a concrete example, vancomycin (VAN), an antibiotic that acts against gram-positive bacteria, is a TDM drug. It is clinically used as a last resort to treat methicillin-resistant *Staphylococcus aureus* infections, which cannot be treated with most other antibiotics [42, 43]. VAN is administered intravenously, and peak therapeutic levels range between 20-40 µg mL^{-1}, with trough levels being 3-10 µg mL^{-1} [23, 44]. Above therapeutic levels, VAN can cause severe side-effects such as nephrotoxicity (renal failure) and ototoxicity (irreversible deafness) [44]. Several assay kits are commercially available to monitor the concentration of VAN in patients under treatment. This includes the VANC Flex® cartridge (Siemens Healthcare Diagnostics Ltd., UK), the QMS® Vancomycin (VANCO) assay (Thermo Fisher; Microgenics Corp., Fremont, CA, USA), and the Emit® 2000 Vancomycin assay (Beckman Coulter Inc., Brea, CA, USA). All these tests require the use of large volumes of serum, between 50-100 µL, collected from blood samples (typically > 1 mL) drawn from the patient. This procedure needs to be repeated as frequently as 3-4 times daily to guide therapy and prevent side effects. Not only do these TDM

kits result in high costs and use of laboratory equipment, but they also expose the patients to an invasive procedure and require their hospitalization during the whole treatment. The availability of point-of-care TDM systems to be used by the patient directly could be extremely valuable and reduce healthcare expenses associated with VAN treatment.

An exciting field of research related to TDM and diagnostics involve the exploration of ISF and other biological fluids for biosensing of biomolecules that correlate with blood concentrations. A number of comprehensive studies on TDM for antibiotics (i.e., vancomycin, gentamicin), immunosuppressants (i.e., mycophenolic acid, tacrolimus), anticonvulsants (i.e., valproic acid), chemotherapeutics (i.e., carboplatin, methotrexate), and other drugs have found strong correlations in many drug concentrations between ISF and blood/serum (Figure 6) [21-23]. With the development of technologies that allow access to ISF, such as MNs for minimally-invasive medical applications, novel concepts have already begun to emerge in efforts to replace conventional TDM and point-of-care diagnostic methods.

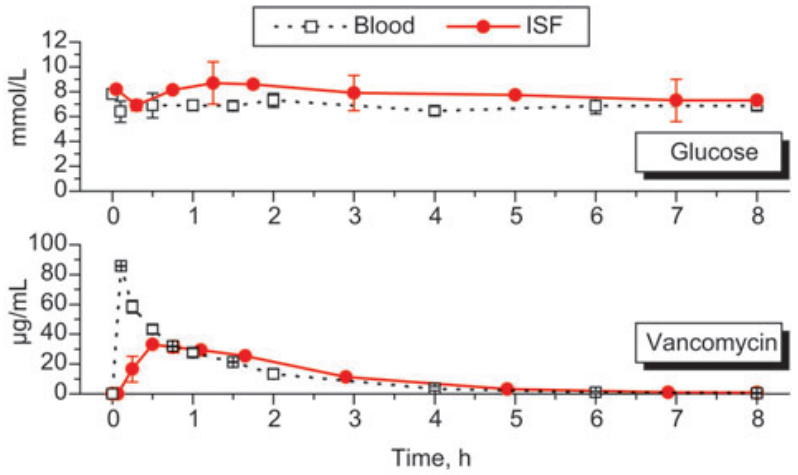

Figure 6. Concentration-time profiles for glucose and vancomycin in blood and interstitial fluid in rabbits [21].

1.2.1.3.1. Microneedle Technologies for TDM

MN technologies have been developed, prototyped, and evaluated *in vitro* and *in vivo* for their respective TDM, diagnostics, and physiological health monitoring, as described in this section. Work performed to date has explored many strategies to employ MN devices for minimally-invasive diagnostics and monitoring activities creatively and uniquely. These strategies include point-of-care diagnostics devices using MNs for ISF extraction followed by off-device analysis, ISF extraction followed by on-device analysis, and without ISF extraction at all; and continuous monitoring systems using MNs. As the area of MN-integrated biosensors for TDM and diagnostics improve and continue to develop, it is likely that more unique and creative approaches will emerge to change the ways current TDM procedures are conducted.

ISF Extraction Device for Off-Device Analysis

ISF, which is abundant in the skin layers, is tightly trapped in its extracellular matrices [20] presenting challenges to successful and repeatable extraction for biosensing applications. Considering that ISF is present at ~ 20 nL mm^{-2} in the epidermis and ~ 800 nL mm^{-2} in the dermis [20], extracting large volumes of ISF for quantitative biomolecule analyses appears to be a major roadblock in developing biosensors for ISF extraction. However, several studies have successfully demonstrated various techniques for ISF extraction from the skin, followed by analysis of its content outside the ISF collecting MN device (termed off-device analysis hereforth).

In one of the first studies exploring the potential of ISF extraction using MNs, Wang et al. (2005) used a glass MN device to penetrate 0.7-1.5 mm into the skin in hairless rats and healthy adults, and collect ISF using a 200-500 mm Hg vacuum for 2-10 min [45]. They collected 1-10 µL of ISF and measured ISF glucose concentrations, and compared to blood glucose collected from the tail

vein of rats and finger sticks in humans. ISF glucose levels correlated well with blood glucose levels in rats and human subjects, although a 20 min time lag was observed. Several practical challenges faced during implementation of this method included multiple steps required to conduct the analysis, requirement of transferring the fluid out of the collection device for analysis, and evaporation of the collected fluid leading to measurement variability and error. Nonetheless, Wang et al. provided the first indication of ISF extraction through pores created through MNs on the skin.

To overcome the need for vacuum-assisted extraction of fluid and risk of ISF evaporation, Sakaguchi et al. (2012) developed an alternative approach to poke-and-collect [46]. Sakaguchi et al. utilized solid MN arrays to create micropores on the skin surface of human subjects through an applicator-driven insertion. Upon removal of the MN arrays, a hydrogel patch was placed on the MN treated area of the skin to facilitate the collection of ISF from the skin by swelling action. Glucose and sodium ion concentrations were determined from the hydrogel matrix to generate the area under the curve (AUC) for ISF (as shown in Figure 5), and compare to plasma glucose from the oral glucose tolerance test (OGTT). Sakaguchi et al. found strong correlations between the ISF and plasma glucose levels, providing a simple solution for glucose measurements without requiring blood. While they could extract and assess multiple analytes from ISF through one process, drawbacks of the proposed process included prolonged measurement time compared to the standard measurement, large number of steps required to obtain a measurement, and variability in the rate of fluid collection during sampling.

Combining the approaches used by Sakaguchi et al., Donnelly et al. (2014) developed a hydrogel-forming MN array, which increased its mass upon skin insertion, due to uptake of ISF from the skin by the hydrogel [47]. These MNs were fabricated using blends of hydrolyzed poly(methyl-vinylether-co-maleic anhydride) and polyethylene glycol (PEG) crosslinked by esterification. Initially, it was shown that the mass of the MN array increased by 30% after 6 h of being inserted in the skin. In a subsequent study, Caffarrel-Salvador et al. (2015) demonstrated ISF extraction by swelling action of these hydrogel-forming MNs during insertion for 1-2 h *ex vivo* into excised porcine skin, and *in vivo* into rats and human subjects (Figure 7) [48]. Theophylline and caffeine were extracted from the hydrogel MNs and assessed using high performance liquid chromatography (HPLC), while glucose concentration was determined using a glucose assay kit.

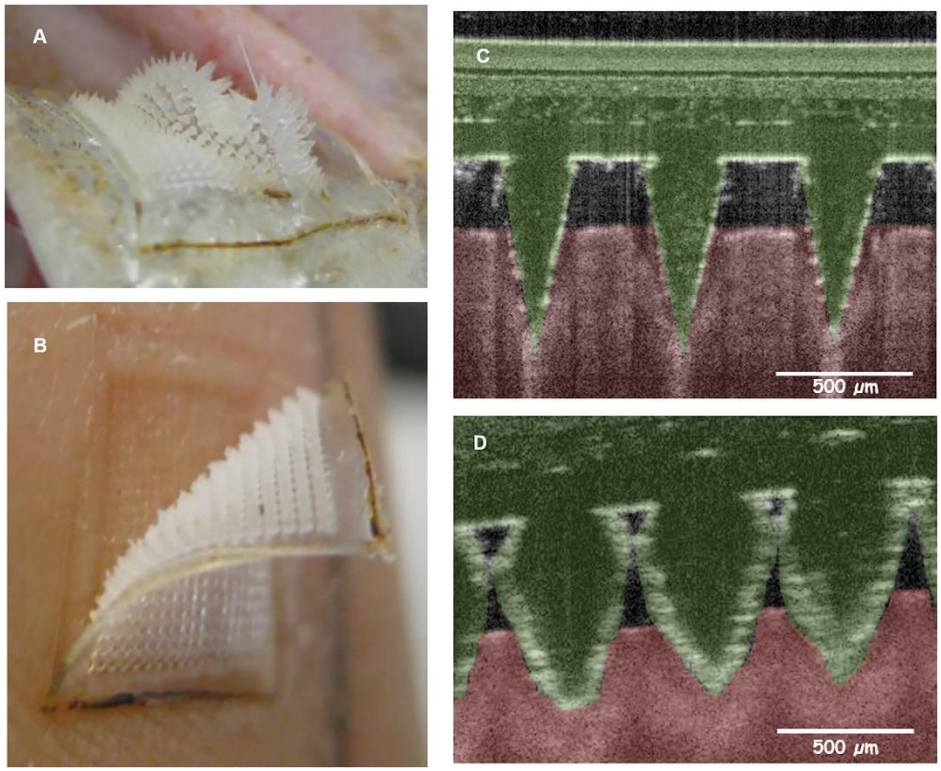

Figure 7. Hydrogel-forming microneedles for extraction of analytes from ISF [48].

In a similar development, Romanyuk et al. (2014) developed solid MN patches with cross-linked hydrogels composed of poly(methyl vinyl ether-alt-maleic acid) and PEG, and demonstrated ISF uptakes up to 50 times the original array volume [49]. These patches were manually inserted by pressing into rat skin *in vivo* for 1 h to extract ISF, followed by wetting the MN patch with 0.1 mL of water and ultracentrifugation to extract the collected ISF from the hydrogel matrix. Though the ability to extract ISF was demonstrated through hydrogel-forming MN arrays, there were major limitations that need to be overcome for these devices to be commercially viable. These limitations include, but are not limited to, prolonged ISF collection periods, a need to extract the ISF and its content from the hydrogel matrix, the requirement of large volumes (microliter-range) of ISF for sample evaluation, and the requirement for large and expensive laboratory equipment to conduct measurements.

ISF Extraction for On-Device Analysis

Due to the limited volume of ISF that could be extracted from the skin, MN-integrated biosensing systems were developed to extract ISF and perform the biomolecule analysis on-device, without being transferred to a separate instrument. In most on-device examples, the collected ISF is transferred out of the MNs to a different compartment of the same biosensing system, such as a fluid reservoir or a sensing chamber.

In the earliest demonstration of the capability of ISF extraction using MNs, Mukerjee et al. (2004) designed an integrated biosensing system with a hollow MN array for transdermal biological fluid extraction and sample analysis, all in one integrated device [26]. Hollow silicon MN arrays were fabricated using a combination of DRIE, diamond blade circular sawing, and wet chemical etching techniques. MN lumens were connected to a microfluidic chip located at the backside of the MN

array, where continuation of the MN lumens to microfluidic channels ensured the flow of fluid by capillary action to the desired location in the chip. Mukerjee et al. demonstrated the ability of the MN biosensing system to collect non-biological and biological fluids, such as water, glycerol, ISF and whole blood using this system. They demonstrated the ability of their hollow MN system with a "snake fang" tip design to extract ISF *in vivo* from human earlobe skin over a 15-20 min period. The extracted ISF was analyzed qualitatively for glucose by placing components of a commercial blood glucose test strip on the fluid reservoir behind the MN array in the chip, and observing a color change in the test strip that indicated a glucose concentration between 80-120 mg dL^{-1}. The drawbacks of the sensor developed by Mukerjee et al. were the needs for microliter-level volumes of ISF for analysis, prolonged time to collect ISF, and transfer of ISF to the backside of the MN for analysis.

In a similar, but potentially more advanced approach for glucose sensing, Zimmerman et al. (2004) developed a hollow silicon MN array to be integrated into an enzymatic glucose sensor with a porous dialysis membrane [50]. Using this glucose sensor, Zimmerman et al. demonstrated a significant sensor response after exposure to ISF suggesting the capability and potential for glucose sensing.

A decade later, Strambini et al. (2014) developed a similar glucose sensing MN device with hollow silicon-dioxide MN arrays, containing projections at 100 µm height, 4 µm tip diameter and 1 x 10^6 needles cm^{-2} [51]. These MN projections were an order of magnitude smaller than other MN technologies that have been used for biosensing. A 10 µL volume reservoir on a chip is integrated to the backside of the MN array for ISF collection via capillary action through the MN lumens. A

screen-printed enzymatic glucose sensor was integrated to the chip located at the back of the MN array. The MN sensor was assessed for glucose in MN-extracted simulated ISF from a reservoir in a petri dish, where the volume uptake was estimated gravimetrically as the mass loss in the petri dish. This MN sensor could determine glucose at a detection range between 0-35 mM at an accuracy within ± 20% of the actual glucose concentration in sample, a sensitivity of 0.46 μA mM^{-1} and a limit of detection (LoD) of 0.6 mM. Compared to Mukerjee et al. and Zimmerman et al., Strambini et al. showed that their device can perform rapid and quantitative analysis of glucose in ISF, although no *in vivo* evaluation was conducted. Besides that, similar drawbacks were seen in Strambini's system compared to Mukerjee et al., including the need to move the sample outside of the MN array for detection and micro-liter level of fluid for biomolecule analysis.

Microneedle-Biosensors without ISF Extraction Requirements

Considering the challenges of extracting ISF, several research groups have developed MN-integrated biosensors for TDM and diagnostics purposes that did not require ISF extraction.

Corrie et al. (2010) developed a point-of-care diagnostic device to selectively extract biomarkers directly from the skin using solid microprojection arrays (MPAs), made by deep reactive ion etching of silicon, to eliminate the need for blood draws for diagnostics [38]. The diagnostic device was evaluated on its capability to capture anti-FluVax®-IgG antibody, 21 days after administration of the FluVax® from the epithelia. Corrie et al. surface-functionalized the MPAs with thiolated PEG after coating the surface with a layer of gold, and grafted anti-FluVax®-IgG capture proteins. After applying the MPAs for a period of 10 mins in serum and *in vivo* in mice ear skin, fluorescence intensity measurements on the MPA surfaces were determined by confocal microscopy. Further,

the functionalized MPAs were assessed by an enzyme-linked immunosorbent assay (ELISA) method for anti-FluVax®-IgG capture after insertion in mouse ear skin for 10 min. Sensitive detection capability of the anti-FluVax®-IgG biomarker showed promise for the solid MN-based minimally-invasive diagnostic devices. In addition, Muller et al. (2012) modified the surface of the MPAs to immobilize anti-NS1 monoclonal capture antibody to bind the NS1 antigen, which is a biomarker for dengue fever, in mice over a 20 min duration [52]. Using an ELISA assay in a 96-wellplate, the captured concentration of the NS1 biomarker was quantified at a detection limit of 8 μg mL^{-1}. Development of surface-functionalized MPAs has eliminated the need for a set volume of ISF collection for analysis, which is a significant advantage, given the limited availability of ISF in the skin. However, the prolonged duration for biomarker capture (10-20 min) and the need for expensive and large laboratory equipment, such as a confocal microscope and 96-wellplate readers for measurement present drawbacks to using MPAs for diagnostics.

Windmiller et al. (2011) designed and developed an electrochemical biosensor using a two-component MN system, which included solid and hollow MN devices, for monitoring glutamate and glucose (Figure 8).

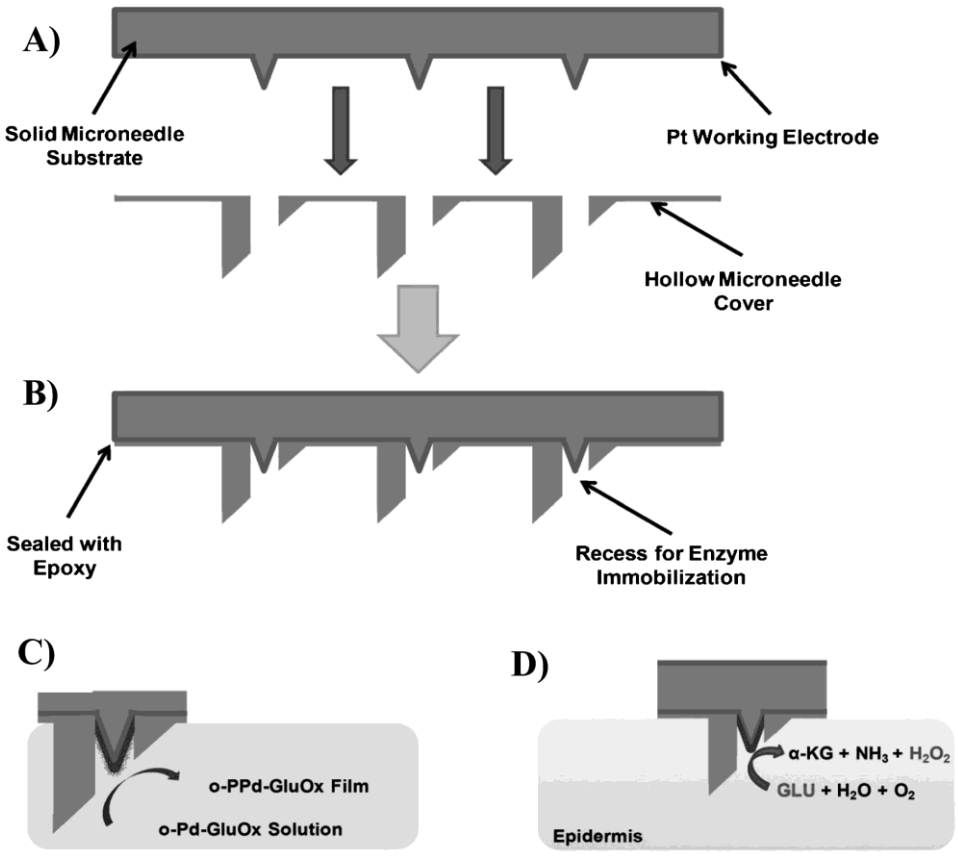

Figure 8. Bicomponent microneedle electrode system consisting of integrated hollow and solid microneedle arrays for glutamate monitoring [53].

The solid MNs were positioned inside the hollow MN, closing the lumen of the hollow MN and providing microcavities, where analyte recognition enzymes (glutamate oxidase and glucose oxidase) were entrapped in a poly(*o*-phenylenediamine) film by an electropolymeric process [53]. This entrapment ensured the rejection of interfering electroactive compounds in the sample. The electrochemical sensor was assessed for detection of glutamate and glucose *in vitro* in a buffer solution and in undiluted human serum. The sensor measured the pathophysiological glutamate concentration range (0-140 µM) at a sensitivity of 8.1 nA μM^{-1} and a LoD of 21 µM. Similarly, the sensor detected glucose over its pathophysiological range from 0-14 mM at a sensitivity of 0.353 µA mM^{-1}, a LoD of 0.1 mM, and a signal-to-noise ratio (SNR) of 3. Similar to Keum et al.

and Corrie et al. the major benefit of this technology is the lack of need for extraction and sampling of biological fluids in monitoring and diagnostics applications.

Similarly, Miller et al. (2012) devised an all-in-one MN-based sensor for *in vitro* amperometric detection of pH, glucose, and lactate to monitor metabolic acidosis and presence of tumors [39]. Hollow MNs in an array were aligned with a well, which was filled with a carbon paste for sensing either pH, glucose, or lactate, and electrically isolated from one another. Change in pH, glucose concentration, and lactate concentrations in ISF-like physiological conditions (between pH 5-8) was detected by the carbon electrode in 0.1 M phosphate buffer against an external Ag/AgCl reference and Pt counter electrodes. However, the sensitivity of detection using this sensor (2.5 nA mM^{-1} glucose) was significantly lower than previously mentioned approaches. In addition, Miller et al. demonstrated the potential of a cell-resistant coating, called Lipidure®, to prevent biofouling of the sensors by macrophage adhesion, which is expected to increase the lifetime of the sensor *in vivo* when implanted as an array of sensing electrodes.

Keum et al. (2015) developed a MN sensor system (MSS) using a solid MN array connected to an endomicroscope for detection of colon cancer [37]. The MSS was fabricated using polycaprolactone, with coatings of polydopamine and poly(3,4-ethylenedioxythiophene), followed by functionalization of hemin molecules on the surface for nitric oxide (NO) binding and detection. Keum et al. confirmed the performance of the MSS for NO detection *in vitro* in simulated biological fluids and cell culture media, and *in vivo* in melanoma tissue. Further, when the MSS combined with the endomicroscope was inserted into mice melanoma polyp regions, a sudden drop in the current detected by the electrical sensor was observed, compared to lack of significant

change in the current in normal tissue. The MSS, operating at 100 mV, demonstrated detection of NO at a high sensitivity of 1.44 μA cm^{-2} μM^{-1} with a LoD of 1 μM NO to detect and distinguish cancer tissues *in vivo* from normal tissue in real-time. Further developments to this MSS system for clinical applications will contribute significantly to improve early detection of cancers.

Continuous Monitoring Microneedle Devices

One of the most promising applications for MN-integrated biosensors is continuous monitoring of biomolecules from the skin's ISF. Though some approaches described previously hinted at the possibility of continuous monitoring, this area of research and development remains to be explored in greater detail.

The first ever MN-based continuous monitoring device that could be partially implanted in the epidermis was developed by Jina et al. (2014), who developed a hollow MN-integrated continuous glucose monitoring (CGM) biosensor [54]. They demonstrated its capability accurately and continuously measured glucose concentrations in the body using ISF. The first prototype of this CGM biosensor consisted of a silicon MN array (~200 hollow projections), a glucose sensor, an electronics module, and a fluid flow system. The sensing chamber in Figure 9, which was located outside the cross-section of the skin, was filled with a proprietary buffer solution containing phosphate and citrate ions to perform mutarotation of glucose and reduce the rate of wound healing in the skin due to the tissue damage caused by the MN insertion, respectively. In doing so, this CGM biosensor was designed to be inserted into the epidermal layer of skin to allow glucose present in the ISF to passively diffuse to an external glucose sensor that is located behind the MN array. This approach was unique from other MN-integrated biosensors, since ISF extraction was not required as a primary function of the device.

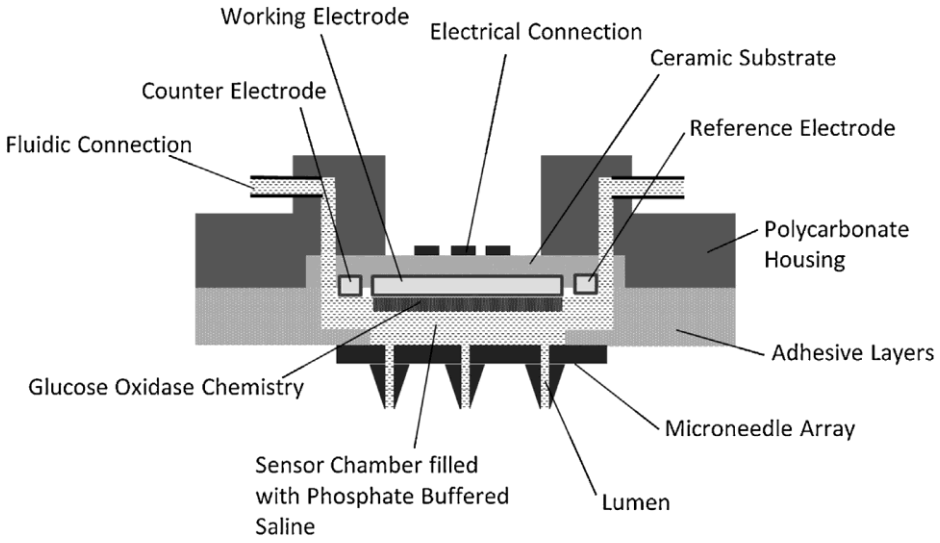

Figure 9. Continuous glucose monitoring biosensor [55].

The biosensor, which is currently being commercialized by Arkal Medical (Fremont, CA, USA), was clinically evaluated in 10 patients, who have received insulin treatment for over 16 years. CGM was done over periods of 48 h and 72 h (Figure 10), and measurements were compared to finger stick blood glucose levels [54].

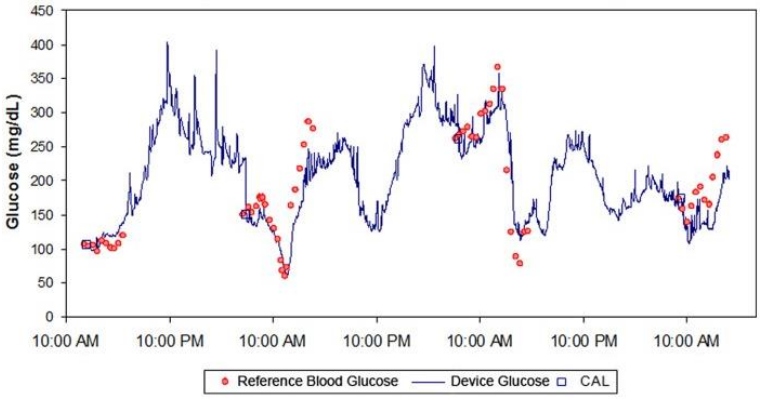

Figure 10. Continuous glucose monitoring by the microneedle biosensor compared to reference blood glucose [54].

A lag time of 17 min was found between the ISF glucose measurements and the blood glucose measurements, but this lag time was comparable to other commercialized subcutaneously implanted glucose sensors [56]. The method introduced and validated by Jina et al. for monitoring analytes in the ISF using hollow MNs can be applicable and useful for other TDM candidate drugs to obtain real-time data to guide therapy.

1.2.2. Structure and Mechanical Properties of Human Skin

The human skin is a multilayered structure, which consists of the SC, the viable epidermis, the underlying dermis, and the hypodermis. Figure 1 depicts a cross sectional view of the human skin [2]. The SC, the top most layer of skin and part of the epidermis, forms the organ's impermeable barrier against the external environment. It is a 10-20 μm thick layer made of dead cornified cells, known as corneocytes (terminally differentiated keratinocytes), produced by the underlying viable epidermis. These corneocytes are flat hexagonal cells with diameters of approximately 30 μm. Partial overlapping and mechanical coupling of corneocytes via protein rivets, along with lipid layers, allow the formation of a mechanical scaffold in the SC [57]. Therefore, the SC is tougher and stiffer than the other layers of the skin [58], and it is predominantly responsible for the hydrophobic nature of the skin [59].

The viable epidermis is approximately 50-150 μm in thickness depending on the location of the skin in the body. It is mainly composed of keratinocytes, which are constantly regenerating cells, and antigen-presenting Langerhans cells (LC). The primary functions of the epidermis are to rebuild and repair the SC, which is continuously subjected to external stresses and damages. The regeneration process of the epidermis is shown in Figure 11 [60].

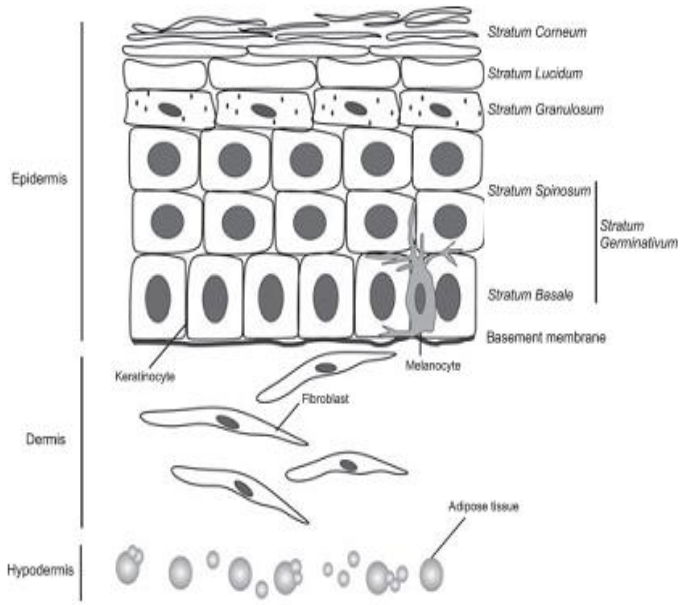

Figure 11. Structure of the human living epidermis, containing melanocytes and keratinocytes that differentiate and establish unique strata [60].

Briefly, mitosis of keratinocytes commences in the innermost epidermal layer of the *stratum germinativum*, the *stratum basale*. Resulting daughter keratinocytes are pushed upwards towards the *stratum spinosum*, where a cell density increase is observed. These cells eventually arrive at the *stratum granulosum*, where they accumulate lipid granules to establish the hydrophobic characteristic to maintain the water barrier. Continued differentiation of keratinocytes in the *stratum granulosum* leads to the loss of the nucleus and therefore a flattened morphology in the *stratum lucidum*. Melanin, a pigment produced by melanocytes in the *stratum germinativum* is transferred to the keratinocytes in the *stratum lucidum* to impart pigmentation. The final product, the SC, is made of completely differentiated dead keratinocyte (corneocytes) combined with intercellular lipids [61]. Due to the absence of nerve or vascular networks in the epidermis, it relies on the dermis layers of skin for nutrients to remain functional [62].

The dermis layer, a major constituent of the skin as an organ, is composed of collagen and elastin fibers, fibroblasts, fibronectin, proteoglycans, and glycosaminoglycans [63]. It is 1-2 mm in thickness, depending on the location of the skin in the body. It hosts and supports nerve endings, hair follicles, and blood vessels, while providing energy and nutrition to the epidermis [58]. Fibrous collagen networks of the dermis contribute to the skin's tensile strength and elasticity, while supporting nerve and vascular networks. The dermis layer has two different regions, namely papillary and reticular regions. The collagen fibers are small and loose in the papillary region, whereas they are tightly and densely packed in the reticular region [59].

1.2.2.1. Mechanical Properties

Quantitative analyses of structural and mechanical properties of skin are difficult to perform for a given population, as these properties are dependent on many factors, including age, race, skin type, relative humidity (RH), temperature, location in the body, and the individual itself. In general, skin is a non-linear viscoelastic, heterogeneous, and anisotropic material [64]. A typical stress-strain curve for full-thickness skin follows a "J-shape", which can be described as non-linear stiffening, as depicted in Figure 12 [65].

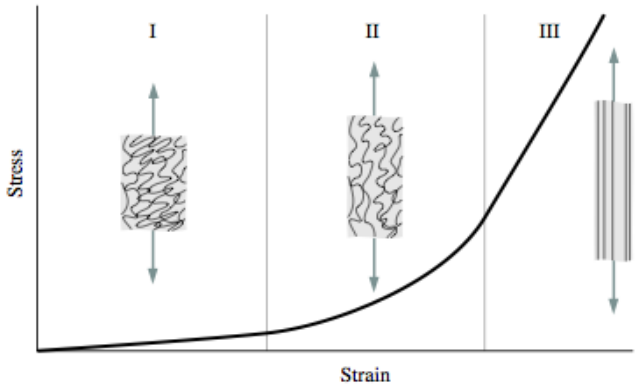

Figure 12. Stress versus strain relationship of skin resulting in a *J*-shaped curve. Regions marked I-III represent low to high modulus responses, respectively[65].

The observed relationship is believed to be a result of the change in collagen fiber arrangement and behavior in the dermis as a function of strain, as illustrated in Figure 12 [66]. At low strain levels (region I), the collagen fibers are in a relaxed condition (not mechanically active), and as a result they appear wavy [65]. The unstretched skin in region I displays isotropic behavior, like a soft rubber sheet, and conforms to Hooke's law, which describes that force

$$F = k\,x \qquad (1)$$

required to displace a spring or a linear-elastic material by a distance x is directly proportional to that distance, where k is the material stiffness. The Young's modulus (E) is used to characterize elastic materials based on the ratio of stress to strain along an axis in a stress range where Hooke's law holds true (Hookean region). It provides a measure of material stiffness. As the strain increases (region II), collagen fibers begin to stretch to line up and bare the load, producing a non-linear response. Further increase in the strain (region III) leads to complete stretching of the collagen fibers, and enhancing the tensile stress on the fibers. A linear stress-strain relationship is observed in region III. Beyond region III, increasing the strain will eventually cause breakage of fibers [65].

Though Figure 12 represents the strain-stress relationship to describe mechanical properties of full-thickness skin, individual skin layers possess distinct and unique properties from one another, which may be more relevant to transdermal applications. The SC, being the stiffest layer of the skin, has shown an estimated range of Young's modulus between 6 MPa (at 100% RH) to over 8,900 MPa (at RH < 30%) depending on the patient-to-patient variability, location in the body, temperature, RH, and the method of analysis [67]. The effect of RH on tensile properties of the SC were examined by Wildnauer et al. (1971), as shown in Figure 13 [68].

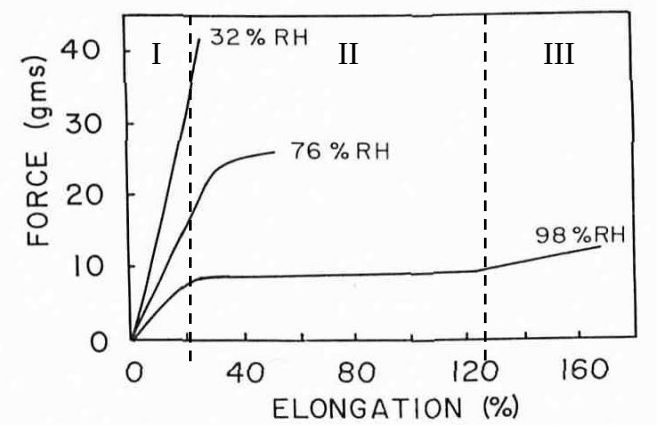

Figure 13. Tensile force versus elongation profiles for human stratum corneum at different relative humidity conditions. Regions I-III represent Hookean, yielding, and strain-hardening regions, respectively. Stratum corneum sample size was 8 mm (length) x 2 mm (width) [68].

At low RH, the elongation profile was limited to the Hookean region (region I, where strain is proportional to applied stress), and fracture occurred at less than 25% elongation at high loads, resulting in a high Young's modulus response. As the RH increased, the elongation to fracture increased (~103%) and the load to fracture decreased, while yielding (plastic deformation) was observed. As the hydration approached 100% RH, all three regions were observed: a Hookean region with elongation up to 10%, yielding between 20-125% elongation, and strain-hardening,

prior to fracture at ~190% elongation. The combined lower epidermal (below the SC) and upper papillary dermal regions have shown significantly less stiffness compared to the lower reticular region of the dermis closer to the subcutaneous fat layer [69].

Table 1 summarizes the Young's moduli of full thickness skin and individual layers determined using many methods and models [70].

Table 1. Published Young's moduli for human and porcine stratum corneum, dermis, and full-thickness skin. Young's moduli were determined by numerous mechano-analytical methods (± estimated standard deviation, where data available) [70].

Skin	Skin Source	Method	Young's Modulus
Stratum Corneum	Forearm and dorsal hand skin from human subjects	Sonic Velocity	13 MPa ± ~19%[71]
	Human cadaveric skin from the thorax/abdomen of subjects 60+ years of age	Tensile *in vitro*	210 MPa ± ~7% (76% RH) [72]
	Human cadaveric skin from the thigh, abdominal, and lower back of three female Caucasian subjects between 76-88 of age		1,000 MPa ± ~120% (32% RH) 5 MPa ± ~85% (100% RH) [73]
	Porcine stratum cornea extracted via trypsin digestion	Indentation *in vitro*	10 MPa ± ~56% (wet) 100 MPa ± ~13% (dry) [74]
Dermis	Inner forearm of Caucasian men	Indentation *in vivo*	35 kPa ± ~16%[75]
	Forearm of 13 human male subjects from 29-47 years of age	Suction *in vivo*	35 – 56 kPa[69]
Full Thickness	Inner forearm of Caucasian men	Indentation *in vivo*	4.5 – 8 kPa ± ~12%[75]
	Inner forearm of 20-year old female subject	Indentation *in vivo*	5.7 kPa[76]
	Forearm of individuals from 3-89 years of age	Torsion *in vivo*	420 kPa ± ~50%[77]
	Forearm of individuals from 6-61 years of age		41 kPa ± ~44% [78]

Skin	Skin Source	Method	Young's Modulus
	61 normal subjects of both genders and various ages	Uniaxial Strain *in vivo*	300 kPa ± ~20%[79]
	Calf of several human subjects of both genders	Uniaxial Strain + Suction *in vivo*	0.6 – 4 MPa[80]
	Forearm of healthy human volunteers (54 men and 69 women) from 8-90 years of age	Torsion *in vivo*	1.1 MPa ± ~20%[81]

1.2.3. Skin Fracture

Penetration of MNs and other devices through the skin SC results in rupture and reversible deformation of the tissue [82]. According to Griffith's theory, which describes the general principle of fracture mechanics of elastic materials [83], the energy required for skin fracture

$$\delta W_C = P\,\delta l - \delta\phi \qquad (2)$$

with the displacement δl of some load P into skin, and $\delta\phi$ is the stored strain energy in the skin when forming the crack with a needle-like structure. As the pressure required to force the load P to form a crack increases, $\delta\phi$ increases, which consequently increases the potential for the crack to close upon retraction of needles from the skin.

There are two penetration mechanisms for needle structures in skin and soft solids – mode-I and mode-II crack propagations. These mechanisms depend on the geometry of the needle tips, as shown in Figure 14 [82].

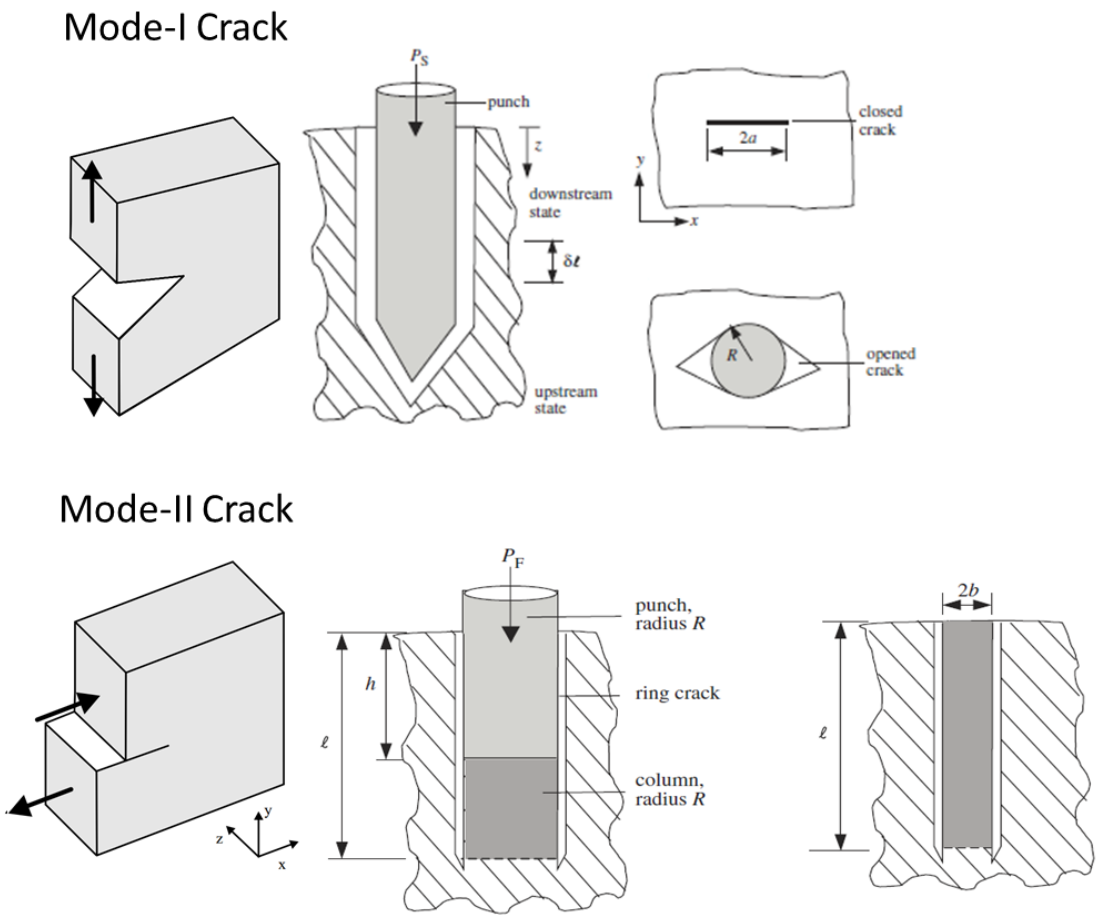

Figure 14. Penetration mechanism of soft solids by a sharp-tipped punch/needle leading to a mode-I crack and a flat-tipped punch/needle leading to a mode II crack and a compressed column of tissue [82].

It has been previously proposed that the crack propagation in skin occurs when the energy delivered by a needle structure exceeds the energy required to create a tear in the soft tissue, and that the skin penetration force for a needle structure depends linearly on its tip area [84]. This assumption was used to predict the force of needle insertion into skin by Davis et al. (2004). A mode-I crack (Figure 14), typically observed with sharp-tipped needles, occurs because of perpendicular tensile stress on the penetration target. Increasing the sharpness of the needle tip leads to a decrease in the penetration force and therefore the stored strain energy, allowing easier

expansion of the crack [82, 84]. Mode-II cracks (Figure 14) are formed by shear stress parallel to the crack plane, and are often observed with flat-tipped, hollow needles [85]. A higher penetration force is required for flat-tipped needles to form a mode-II crack (relative to sharp-tipped needles for mode-I cracks). A compressed column of solid material is formed ahead of the flat-tipped needle in mode-II cracks. Chua et al. (2013) explored the mechanics of MN insertion using sharp-tipped and blunt-tipped silicon hollow MNs to cause mode-I and mode-II crack formation, respectively [55]. Chua et al. (2013) found that the minimum applied pressure required to cause fracture in the SC using a sharp-tipped MN was 9-fold lower compared to a blunt-tipped MN, confirming the difference between mode-I and mode-II crack formation based on MN geometries. The type of tissue influenced the force of incision of an object. For example, higher penetration forces have been reported in pig skin compared to human skin [86], as well as in skin and muscle compared to fatty tissue [87].

1.2.4. Human Skin Substitutes

The low availability or lack of freshly excised human skin specimens for biophysical and biomechanical research involving skin, including bite mark research [88], wound healing [89] and transcutaneous device testing of MNs for example [70], can be challenging for technological developments in many disciplines. Potential reasons for the difficulty in acquiring human skin for research and development work range from ethical considerations [88] to a lack of donors. Mechanical properties of human skin can vary as a function of source (i.e., race, gender, age, and body location), state (i.e., fresh/live, frozen, and immersed in solution), and environmental conditions (i.e., temperature and RH). The measured properties can also depend on the testing protocol which typically measures force versus distance relationships during tension, compression,

and indentation. Much work over many decades has assessed the mechanical properties of human skin to identify the factors affecting the mechanical behavior of skin as a whole, as well as individual layers [68, 69, 75, 77, 90-92]. Mechanical properties have been tabulated previously [70, 93] to illustrate the large variability in the mechanical responses of skin.

Table 2. Anatomical and compositional differences between human and porcine skin.

Skin Layer	Attribute	Human Skin	Porcine Skin
Stratum corneum	Total lipid content (% weight)	10 [98]	8 [98]
	Polar lipid content (% weight of total lipids)	70 [98]	64 [98]
	Non-polar lipid content (% weight of total lipids)	30 [98]	36 [98]
	Thickness	20-40 μm [99]	12-31 μm [100, 101]
Viable Epidermis	Thickness	50-120 μm [102]	30-100 μm [103]
	Differentiating corneocyte layers	4 (stratum germinativum, spinosum, granulosum, lucidum) [89]	3 (stratum germinativum, spinosum, granulosum) [89]
Dermis	Relative elastic fiber level	High [89]	Low [89]
Full-thickness	Moisture content (% volume)	24-67 [104]	35-68 [99]

Animal skins, especially from small mammals, have served as common substitutes for human skin [91, 94]. However, different animal skin types possess significant anatomical and physiological differences compared to human skin [95]. The most accurate model for human skin was found to be porcine skin, from the perspectives of anatomy and physiology [88, 89], immunogenicity, cellular composition, and morphology [96]. This led to the assumption that porcine skin would

also have similar mechanical properties to human skin. Many studies thus used porcine skin as a substitute for human skin [73, 74, 97] without confirming the mechanical similarities of both skin types in controlled experiments. Though similar in anatomy and composition, subtle differences in the porcine skin structure may contribute to mechanical differences, as listed in Table 2.

1.2.4.1. Impact of Skin Storage

For storage, skin is typically frozen to preserve the skin's mechanical properties without inducing biological decomposition and structural changes [93]. Compared to other skin preservation methods, such as using formaldehyde for histology or embalming dead bodies, freezing induces the least structural and mechanical changes to skin. Micozzi (1986) showed that freezing causes mechanical disruption of skin and connective tissues leading to a decrease in stiffness in rat skin [105]. Foutz et al. (1992) showed that freezing at -70 °C did not affect the in-plane Young`s modulus, loading response and the ultimate tensile strength of rat skin, but significantly lowered its fracture strength [94]. More recently, in a non-mechanical characterization of skin, Mansoor et al. (2015) showed that freezing increases the diffusivity of drugs in porcine skin, most likely due to ice crystal formation during the freezing process, which subsequently leads to structural damage, increased porosity, and possible changes in the mechanical properties of the skin. The diffusion coefficient of doxorubicin was higher in frozen and thawed porcine skin compared to freshly excised porcine skin. The observations by Mansoor et al. (2015) agreed with the findings of Kasting and Bowman (1990), who found that the permeability of sodium ions in fresh human skin was significantly lower than in previously frozen human skin [106, 107]. Since most indications on the likelihood of mechanical changes in human skin due to freezing were derived from small

animal and non-mechanical studies, there is a need to determine the effect of freezing on the mechanical properties of human skin directly.

The mechanical properties of skin have a significant impact on how MNs can be applied to the skin surface. MNs are insertion-tested on skin as a quality control measure and to demonstrate successful penetration through the SC. Only a small number of MN insertion tests were conducted over the past decade directly in alive humans [55, 84] due to challenges in accessing these human skin tissues. The majority of other skin indentation tests have been conducted using human cadaver skin [108, 109], frozen and thawed human skin [110], fresh porcine skin [106], frozen and thawed porcine skin [16, 111], and other animal skins [18, 112]. Thus, the MN insertion characteristics from these studies are difficult to compare with each other and were not able to fill the gaps in the knowledge surrounding the interactions between skin and MNs.

1.2.4.2. Artificial Skin Models

Artificial human skin, made typically in laboratories using tissue engineering and/or various polymer scaffolds, is mostly designed for use in skin replacement during surgical procedures, testing pharmacological effects of therapeutic agents, and to replace the use of animals in pre-clinical testing. Due to the complexity of human skin, both in structure and function, an accurate and fully functional artificial skin replacement has not been developed to date. Various skin and soft-tissue models have been fabricated using biomaterials and cell sources, as described below. More recently, microfluidic patterning devices to fabricate polymer composite soft-tissue models using multiple hydrogels carrying biomolecular payloads have been developed [113].

1.2.4.2.1. Tissue-Engineered Models

Tissue engineered skins are used to improve and replace biological functions of skin by using a combination of cells, engineered materials, and biochemical and physiochemical factors. Tissue engineered skins, including cell-free and allogeneic cell-containing substitutes, are primarily used to prevent fluid loss; protect from contamination; deliver dermal components, growth factors, and cytokines to the wound; enhance the wound's healing process; and as temporary coverings for wounds until an autograft is available. Cell-free skin substitutes can also be used in combination with autografts for further surface protection. Tissue engineered skin models are especially advantageous, compared to autografts, in terms of availability, manufacturing costs and mass production. An illustration of the basic process of producing tissue-engineered skin models is shown in Figure 15 [60].

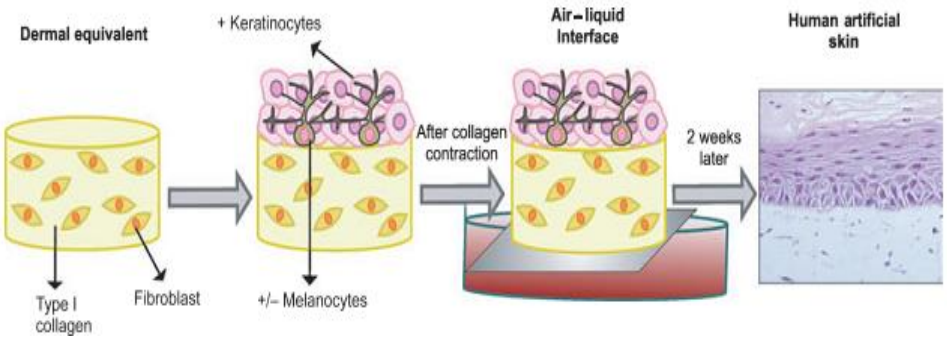

Figure 15. Basic principles and process of skin tissue engineering [60].

Briefly, keratinocytes, fibroblasts and type-I collagen are isolated from the human donor tissues and cell cultured for expansion. Fibroblasts and type-I collagen are seeded in an appropriate scaffold material (typically hydrogels) and allowed to proliferate to establish the dermal equivalent in a tissue-engineered skin model. Keratinocytes and melanocytes are plated on top of the dermal

compartment of the model to grow the epidermal substitute. Approximately 24 hours post-plating, the entire full-thickness skin is transferred to a steel grid (to an air-liquid interface) to allow further development of the epidermal layer into a multilayered stratified tissue [60]. These skin models can be categorized per the structure and function of the skin that they are made to represent and replace, including epidermal, dermal, and full-thickness substitutes.

1.2.4.2.2. Mechanical Skin Models

There are needs for artificial skin models that do not require extensive cell culturing and tissue regeneration, but instead possess similar mechanical properties to human skin. Such applications include the testing of percutaneous medical devices *in vitro* and the development of transdermal drug delivery methods. In recent years, a number of artificial mechanical skin models (AMSMs) have been suggested in the literature, based on polydimethylsiloxane, polyurethane, and hydrogels [114-118]. Many of the suggested models have not been originally designed to simulate the mechanics of human skin, and none of them have been scientifically validated against human skin to be an adequate mechanical representation thereof.

A full-thickness skin can be considered as being composed of three layers: a SC, a viable epidermis, and a dermis. Though the SC is the upper portion of the epidermis, they do not share the same mechanical properties. Therefore, the SC must be stronger and stiffer than the subsequent two layer, and must be isotropic and viscoelastic. For the fabrication of such a model using polymers, several options are available. For example:

- Biopolymers, such as polyaspartates, are water-insoluble, flexible, and biodegradable. A drawback for their utility is the high cost.

- Hydrogels are highly water absorbing networks of hydrophilic polymer chains. Low compressive strengths of hydrogels may limit their utility in modeling skin layers. Cross-linking hydrogels can increase their strength, which improves their potential use in artificial skin models, especially to represent the hydrophilic dermal compartment.
- Soft rubbers, such as polydimethylsiloxane (PDMS) elicit viscoelastic material properties, can be easily fabricated, and spread easily over a surface.

PDMS is a type of silicone oil belonging to a group of polymeric organosilicon compounds, which is frequently used in soft lithography processes to produce microelectromechanical systems (MEMS) devices [119]. PDMS products can be used to fabricate the SC and epidermis with the desired viscoelasticity, hydrophobicity, and high tensile strength. Transparency of PDMS in skin models also allows visualization of percutaneous devices during *in vitro* testing. The choice of mixing proportions of silicone rubber products allows to achieve desirable mechanical and optical properties of the resulting mixture. These silicone rubber layers can be stacked together to form a skin composite model, as performed by Passot and Cabodevila (2010) and depicted in Figure 16. This model was designed and fabricated to simulate the heel of an infant for blood sampling. This final full-thickness model was not compared to human skin for mechanical similarity.

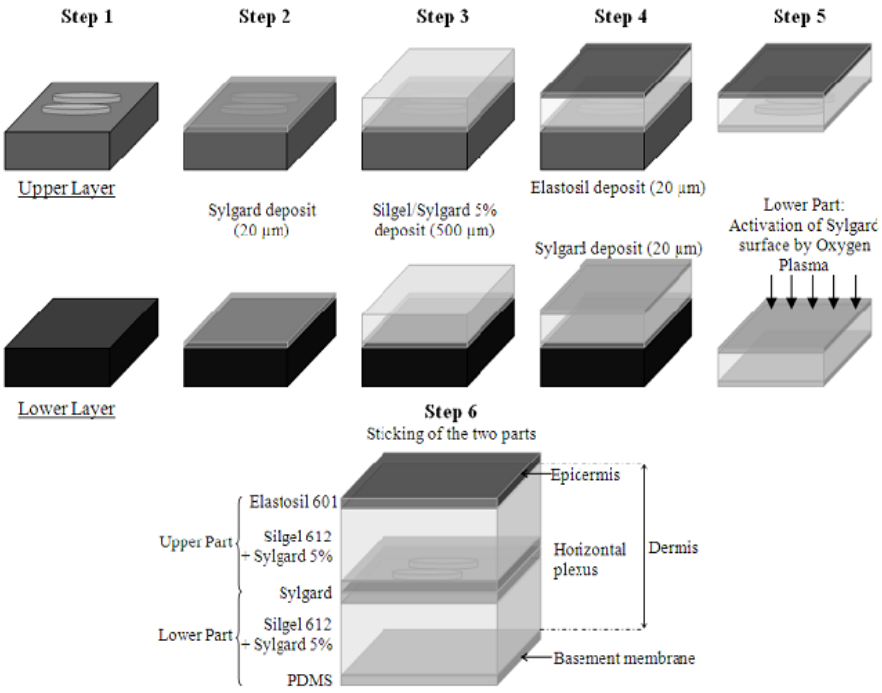

Figure 16. Soft lithography process of fabricating an artificial mechanical skin model from silicone rubber products [114].

Koelmans et al. (2013) described a bi-layer mechanical skin simulant with a commercial polyurethane foil and 3% (w/w) agarose gel to characterize the insertions of "large" MNs (> 1mm in height) and 30-gauge sharp hypodermic needles (30G) [115]. Though the mechanical properties of polyurethane foils were not examined by Koelmans et al. (2013), they typically possess an ultimate tensile strength and a Young's modulus of 17 MPa and 22 MPa, respectively [120], which fall in the ranges of the human SC and PDMS. A justification for mechanical similarity between the polyurethane-agarose skin simulant and the human skin was not provided.

1.2.5. Assessing Intradermal Delivery

The performance of ID devices during the delivery of liquid formulations into the skin is assessed for dose accuracy and fluid wastage. The latter is typically assessed as backflow, the leakage of

fluid from the injection site back onto the surface of the skin due to the skin's resistance to expansion [106, 121]. In the past, gravimetric, volumetric, and several imaging techniques have been used to assess ID fluid delivery during product development [106, 121-123]. Gravimetric analysis has been the go-to method used to determine dose accuracy (fluid delivery potential), fluid wastage, and syringe/ID device dead-space according to ISO 7886-1:1993 and ISO 11608-1:2000 standards published by the International Standards Organization (ISO) [124]. Gravimetric analysis has yielded relatively higher accuracy measurements of fluid delivery using hypodermic needle/syringe devices compared to volumetric analysis [122]. During gravimetric analysis, the delivery device is weighed without filling the fluid, after filling and priming the fluid, and after injecting the fluid into the skin [122]. The difference in the mass of the syringe before and after the injection provides the mass of fluid delivered into the skin, which can be converted to volume of fluid delivered to determine the dose accuracy [122]. However, for ID product development, the gravimetric method provides a number of challenges measuring the typical small delivery volumes, including lack of measurement sensitivity, evaporation of fluid prior to measurement and the inability to accurately capture fluid backflow as interfering liquids on the surface of the skin, such as oil and sweat, can contribute to errors in measurement [125, 126]. Electronic balances are used for measurement of mass of the syringe at various time points during dose accuracy determinations with a typical accuracy of 0.0001 g, corresponding to 0.1 µL accuracy for water [126]. For dead-space determination in hypodermic syringes per ISO 7886:1 1993, the gravimetric measurement capability requirements are even weaker with listed sensitivity being 0.2 g (200 µL) at an accuracy of 7 mg (7 µL). Therefore, an alternative, highly sensitive method for characterizing ID fluid delivery is needed.

Several imaging techniques that are described below have been used to assess, characterize, and quantify fluid flow during ID fluid delivery, but they are inferior in performance to the gravimetric analysis. Injection of X-ray contrast media into the skin using ID delivery techniques, capture of top-view images of the skin at the injection site with an X-ray camera, followed by categorical assessment of the resulting X-ray images based on a clinical scoring scale have been used previously to determine the delivery location of fluid into the skin [121]. The X-ray imaging mechanism did not provide direct measurements of the fluid delivered and fluid backflow. Laser scanning confocal microscopy (LSCM) has been used for visualization of the skin [127] and quantification of intradermal injections [106], but with significant drawbacks. These drawbacks of LSCM include limited range of lasers to excite fluorophores, requirement of high intensity lasers to penetrate into desired depths of skin for imaging, photo-bleaching of fluorophores and destruction of viable tissues due to exposure to high intensity laser, and auto-fluorescence of skin [127]. Thus, performing quantitative fluid flow assessments from ID injections in the skin using LSCM has not been a feasible technique. A three-dimension ultrasound echography method has been used to determine and locate fluid depositions in the skin using ID delivery techniques [121], but was not a high sensitivity method for fluid flow quantification, due to the low resolution nature of ultrasound imaging [128]. The ultrasound echography method provided bleb and fluid flow profiles within the skin layers, alongside histology cross-sections.

A more powerful methodology involving coating a radio-labelled tracer protein (^{14}C-ovalbumin) to the payload of a solid MN array was explored by Pearson et al. [129]. The use of ^{14}C-ovalbumin allowed accurate measurement of the payload delivered to the skin and left on the solid, coated

MN array; however, this method was only suitable for use with solid matrices, and not with the injection of liquid formulations.

1.3. Gaps in Current Knowledge

Much research has been conducted on characterizing MN insertions into skin, but a large variability in penetration forces and a non-reproducibility of results are challenges that have not been addressed effectively. MN insertion forces from different authors are hardly comparable, due to the differences in the MN geometries and insertion parameters (i.e., velocity and applicator devices); the skin specimens (i.e., type, race, gender), skin location in the body, and preservation state (i.e., frozen, or freshly excised); and external factors, such as RH and temperature. Comprehensive and controlled mechanical assessments and MN insertion profiling in human skin are necessary to understand the factors that influence the most important MN functionality – their ability to penetrate through the SC layer.

To further facilitate the understanding of MN performance, development and validation of standardized materials and protocols to evaluate the dynamic processes involved during MN insertion into skin is necessary. Design and fabrication of skin models, which behave similarly to human skin under compression and tension in controlled environmental conditions, would prove invaluable to standardize the testing, evaluation, and comparison of MN devices. Such a substrate will facilitate the study and understanding of the dynamics of MN insertions, which has not been evaluated thoroughly to date. Understanding the dynamics of MN insertions will contribute to the design and development of MN devices and applicators that can improve the ease of performance,

increase the likelihood of success, and reduce the human error of MN insertion through the SC layer.

MN devices are assessed for drug delivery performance into the skin. Presently, gravimetric analysis is used to determine metrics, such as dose accuracy or fluid delivery potential, and fluid wastage per ISO 7886-1:1993 and ISO 11608-1:2000 standards. However, due to the lack of sensitivity of gravimetric and other methods used to assess MN performance, more precise and sensitive methods are needed to determine how accurate MNs are during drug delivery. Low dose requirements for medicine delivery using MNs compared to conventional intramuscular and subcutaneous delivery demands more sensitive performance assessment methods for MN devices.

Most of the current TDM and biosensing practices involve blood extraction using hypodermic needles or lancets. Correlations in drug concentrations between blood and the skin's ISF makes MN technologies particularly attractive for TDM applications, and might replace conventional and invasive techniques. Most MN biosensing technologies that involve the extraction of ISF are faced with the difficulty of extracting sufficient volumes for *in situ* analysis due to the lack of ISF in the skin. This leads to challenges with repeatability of measurement, and transferring collected ISF to analytical and measurement sites, typically outside of the MNs. Novel and creative designs and modifications to MN technologies would help to overcome the difficulties with ISF collection, leading to accurate and reliable biosensing.

1.4. Objectives of the Dissertation

The research documented in this thesis aims to improve the understanding of MN functionality for drug delivery and biosensing. The key objectives of this dissertation are to:

1 Determine how human skin and porcine skin, its closest biological substitute, behave under mechanical stress and during MN insertion in different states and environmental conditions.
2 Develop an artificial mechanical skin model that simulates the mechanical properties of human skin to provide a standardized platform for *in vitro* testing of MN insertions.
3 Determine the factors influencing MN insertion, including geometry and array design, to develop MN insertion protocols to achieve repeatable insertions.
4 Determine the injection performance of hollow MNs, compared to conventional ID fluid delivery techniques; and develop a precise method to evaluate MN performance.
5 Develop a MN-biosensing device to collect, trap and detect biomolecules directly in the hollow MN with extremely low volumes of fluid.

2. MICROMECHANICAL ANALYSIS OF BIOLOGICAL SKINS FOR MICRONEEDLE INSERTION ASSESSMENT

Obtaining human skin samples for medical research, including developing MN-based medical devices, is challenging. Researchers rely on human skin substitutes and skin preservation techniques, such as freezing, to overcome the lack of skin availability. Porcine skin is considered the best substitute to human skin, but their mechanical resemblance has not been fully validated. This chapter provides a direct mechanical comparison between human and porcine skin samples using a conventional mechano-analytical technique (microindentation) and a medical application (MN insertions), at 35% and 100% RH. Human and porcine skin samples were tested immediately after surgical excision from subjects, and after one freeze-thaw cycle at -80 °C to assess the impact of freezing on their mechanical properties. This mechanical comparison between human and porcine skin will serve as a reference for mechanical studies involving the two skin types, and assist in identifying the conditions where human skin can be simulated using porcine skin.[1]

[1] A version of chapter 2 has been published:

Ranamukhaarachchi S.A., Lehnert S., Ranamukhaarachchi S.L., Sprenger L., Schneider T., Mansoor I., Rai K., Häfeli U.O., Stoeber B. A micromechanical comparison of human and porcine skin before and after preservation by freezing for medical device development. Scientific Reports 6, Article number: 32074 (2016) doi:10.1038/srep32074.

2.2. Materials and Methods

2.2.1. Biological Skin Preparation

The study obtained and utilized fresh human skin excised from the abdomen region in four abdominoplasty patients under informed consent; and porcine skin excised from the abdomen of four female miniature Yucatan pigs weighing 20-30 kg (Sinclair Bio-resources, Columbia, MO). The use of discarded human skin samples for this study has been approved by the University of British Columbia's Clinical Research Ethics Board and was performed per Canada's Tri-Council Policy Statement (TCPS-2: 2014) and the chapter about the use of Human Biological Materials. The use of animals for this study was approved by the University of British Columbia's Animal Care Committee and all experimental protocols conformed to the Canadian Council on Animal Care guidelines.

In this study, excised tissues that were labeled as fresh skin samples were used approximately 2-3 hours after excision from the subject. All freshly excised skin samples from human and porcine subjects were assumed to retain their mechanical properties from immediately after excision to three hours after excision, when all mechanical tests were conducted. However, possible degradation of mechanical properties of skin over the 3 hour period was not evaluated herein. A portion of the freshly excised skin was immediately frozen at -80 ^{o}C for 48 hours, and thawed for 1 hour before testing. The freezing conditions at -80 ^{o}C were used to rapidly freeze the skin samples and to minimize the impact of ice-crystal formation on the specimens. Samples were thawed for 1 hour at room temperature to ensure all ice formed during freezing melted rapidly without damaging the skin composition. All skin samples were re-stretched to their original dimensions, cut, and mounted on a rigid flat substrate prior to testing, since skin contracted rapidly from its natural

dimensions. For example, the area of porcine abdominal skin samples obtained for this study contracted by 50-64% post-excision. The SC layers were separated from the subsequent layers by a mild heat treatment at 60^{o}C for 180 s in a sealed plastic bag in a water bath [72, 130]. The SC, epidermal/dermal composite (ED) after the SC was removed, and full-thickness skin composite (FT) layers were stretched to their original dimensions. Skin samples were incubated at 35% and 100% RH conditions for 20 minutes before testing in glass petri-dishes. The 35% RH condition represented a physiologically-relevant humidity level for skin, and was achieved by adjusting the RH of the ambient air, which typically ranged between 32-38% RH. The 100% RH condition was reproducibly attained for skin testing by placing wetted paper towel around the skin samples in a closed petri-dish for 20 minutes; and had shown influence on skin mechanical properties in previous analyses [74, 131]. As shown in Figure 13, the skin mechanical properties changed significantly between 32% RH and 98% RH.

2.2.2. Micro-indentation of Skin Samples

Micro-indentation tests were performed using a Q400 TMA instrument at 35% and 100% RH, and at 22 ^{o}C. The Q400 "penetration" probe (cylindrical tip, diameter of 0.89 mm) was loaded onto and unload from the skin samples at a rate of 1 N min^{-1} normal to the skin surface to a maximum force of 0.1 N for the SC samples. For ED and FT skin samples, loading and unloading was performed at 0.5 N min^{-1} to a maximum force of 0.05 N (maximum displacement less than 10% of the total thickness of the skin sample [132]. The load-displacement data were recorded at 10 Hz during the test to generate load-displacement profiles (as shown in Figure 17B). According to Doerner et al. (1986), the initial one-third of the unloading data can be used to determine stiffness (S) of the material during a flat-punch indentation [133]. In this study, for each load-displacement

plot obtained, the initial linear portion of unloading plot was used to determine the *S*, which was related to a reduced Young's modulus

$$E_r = \left(\frac{1}{\beta}\right)\left(\frac{\sqrt{\pi}}{2}\right)\left(\frac{S}{\sqrt{A_p}}\right) \qquad (3)$$

where *ß* was a tip geometrical constant (*ß* =1 for flat-ended cylindrical punch, as present in the micro-expansion probe) and A_p was the projected area at maximum depth of indentation. In this analysis, a flat-ended cylindrical punch was used as the indenter tip. Thus,

$$A_p = \pi\left(\frac{890\ \mu\text{m}}{2}\right)^2 = 6.22\text{x}10^{-7}\ \text{m}^2 \qquad (4)$$

corresponds to the surface area of the tip of the probe. The estimated E_r is related to the Young's modulus of the sample E_s through

$$\frac{1}{E_r} = \frac{(1-\nu_i^2)}{E_i} + \frac{(1-\nu_s^2)}{E_s}\ , \qquad (5)$$

where E_i and ν_i were the Young's modulus and Poisson's ratio of the indenter tip (E_i = 71 GPa and ν_i = 0.17 for the quartz micro-expansion probe tip), and ν_s was the Poisson's ratio of the sample (ν_s = 0.49 for skin). Therefore, Young's modulus of skin, which is a material property, was calculated from stiffness, which is a structural response of the material to deformation. Each microindentation test was performed eight times per subject per RH condition.

2.2.3. Microneedle Insertions

Single hollow nickel MNs, fabricated according to Mansoor et al. (2013) [16], were insertion-tested under quasi-static conditions at 22 ^{o}C in FT skin samples using the Q400 TMA instrument

at 35% RH and 100% RH. Though skin is a viscoelastic material, quasi-static MN insertion conditions (MN impact velocity ~ 0 m s^{-1}) at 22 ^{o}C were selected over dynamic conditions (MN impact velocity > 0 m s^{-1}) and human physiological temperature, due to the ease of control of the test conditions and similarity of quasi-static insertion to practical manual MN insertions. A single hollow MN (30 μm tip diameter, 450 μm height) was mounted onto the TMA micro-expansion probe (cylindrical tip with a diameter of 2.54 mm) and applied perpendicular to the skin surface at 10 N min^{-1} to a maximum force of 2 N. Force exerted on the skin by the MN as a function of its displacement into skin were recorded during the test at 10 Hz to generate force-displacement profiles (Figure 18A). As shown by Davis et al. (2004), the location where the insertion force decreases briefly for increasing MN displacement indicates the point where the MN ruptures the SC [84]. It is at this point that force of insertion (F_{ins}) and displacement at insertion (D_{ins}) are determined. Further, the stiffness, S of the skin was determined from the slope of the linear elastic region of the force-displacement plot. Each MN insertion test was performed four times per subject per RH condition. Due to the complexity in the mechanical properties of skin layers, and the primary interest in the rupture of the SC layer, the influence of subcutaneous tissue and underlying muscle on the MN insertion process was not assessed.

2.3. Results and Discussion

Microindentation and MN insertion profiling were used to assess and compare the mechanical properties of skin (Figure 17A). Skin samples were distinguished by source (human vs. pig), state (freshly excised vs. frozen and thawed), and the RH condition used during testing and analysis. Microindentation and MN insertion provided completely different mechanical characteristics of the skin, and provided greater insight into the anisotropic and heterogeneous nature of skin. During

microindentation, the skin layers (individually or composite) are compressed by the microindenter; and the compressive strength (out-of-plane) of the skin layer dominantly impacts the resulting Young's modulus measurement. In contrast, during MN insertion, tensile strength (in-plane) of the skin layers impart a dominant effect on the resulting mechanical properties, as described later.

The Young's moduli of the SC (E_{SC}), of the viable epidermis/dermis (E_{ED}), and of the full-thickness skin (E_{FT}) are shown in Figure 17 for skin specimens from all human and porcine subjects in this study. Due to inherent and significant subject-to-subject variability among human and porcine subjects, analysis of variance with a three-factor factorial experiment in complete randomized arrangement of treatments (ANOVA; Table 12 provided on page 160) and Fischer's Protected Least Significant Difference analysis (LSD; Table 3) were conducted by pooling data from all four subjects per skin source (i.e., human vs. pigs) into individual data sets.

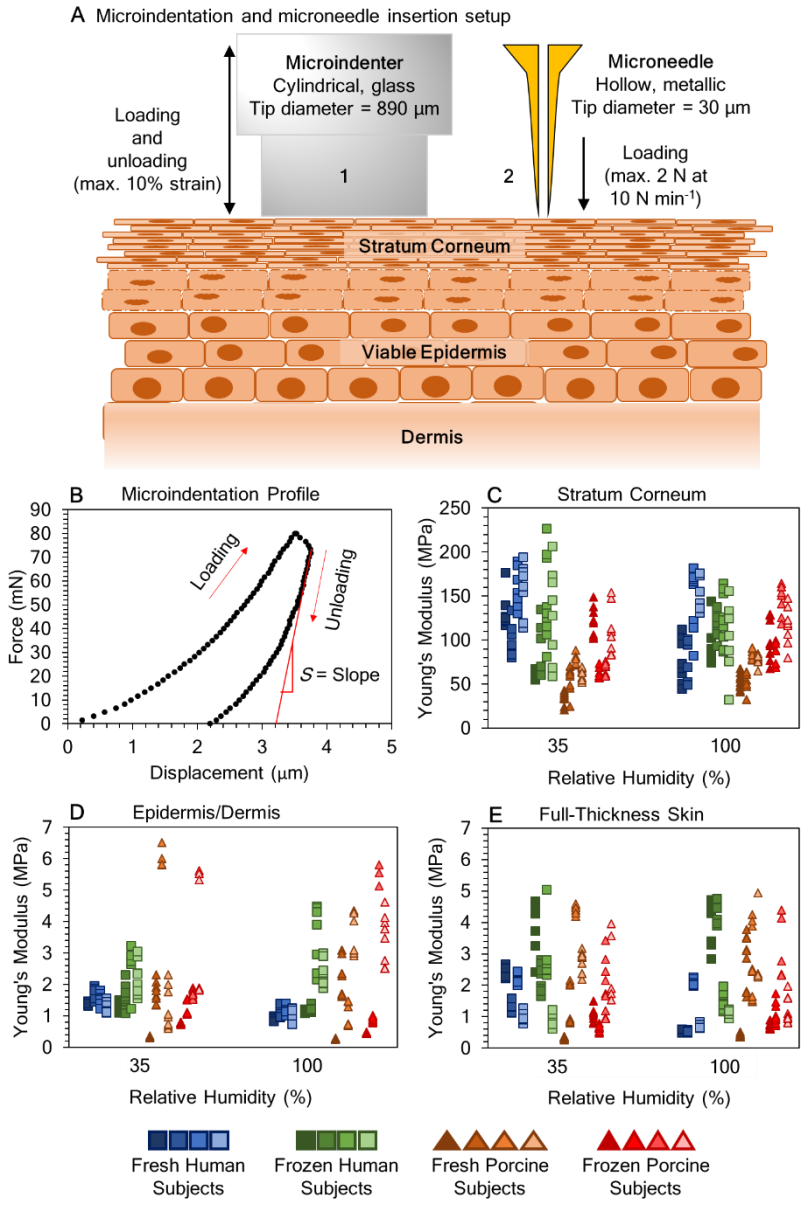

Figure 17. Microindentation of skin layers. A cylindrical microindentation tip (A-1; 0.89 mm diameter) loaded and unloaded a force into/from the skin surface. A hollow microneedle (A-2; 30 µm tip diameter) was inserted into skin at 10 N min^{-1} to a load of 2 N. The initial slope of the microindenter unloading (B), for example, of fresh human stratum corneum at 100% RH, was used to estimate the stiffness of the skin layer to determine the Young's modulus. The out-of-plane Young's moduli of stratum corneum (C), epidermal/dermal composite (D), and full-thickness skin (E) were determined for human and porcine skin before and after freezing at -80 °C for 48 hours (four human, four porcine subjects tested at 35% and 100% RH; n=8 per subject per condition). Hysteresis of the human stratum corneum can be seen in figure B.

Table 3. Effect of skin source, state, and relative humidity on the Young's modulus of the stratum corneum, epidermis/dermis composite, and full-thickness skin determined by microindentation analysis of fresh and frozen human and porcine skin layers. The least significant difference (LSD, P = 0.005) value is provided for the treatments that significantly influenced the Young's modulus of skin at a 95% confidence interval (indicated by superscripted a and b next to the mean value). The LSD is not provided if the F-value of treatment is not significant (NS).

Treatments		**Stratum Corneum** (MPa)		**Epidermis/Dermis** (MPa)		**Full-Thickness Skin** (MPa)	
		Mean	**SD**	**Mean**	**SD**	**Mean**	**SD**
Source	Human	117.12^{a}	41.74	1.61^{a}	0.74	1.88	1.23
	Porcine	81.28^{b}	31.63	2.06^{b}	2.18	1.74	1.28
	LSD	8.16		0.39		NS	
State	Fresh	93.36^{a}	44.92	1.55^{a}	1.23	1.71	1.22
	Frozen	105.05^{b}	36.28	2.12^{b}	1.93	1.91	1.29
	LSD	8.16		0.39		NS	
Relative Humidity	35%	98.69	45.42	1.77	1.27	1.87	1.19
	100%	99.71	36.6	1.9	1.94	1.75	1.33
	LSD	NS		NS		NS	
CV (%)		33.43		87.10		63.83	

2.3.1. Young's Modulus of the Stratum Cornea

The mean E_{SC}, extracted from microindentation profiles (Figure 17B), ranged between 108-139 MPa for human skin and 56-111 MPa for porcine skin, which is comparable to other mechanical studies of skin where the E_{SC} ranged from 5-1,000 MPa [72, 74]. In general, the E_{SC} was found to be significantly higher in human skin compared to porcine skin in our study (Figure 17C, Table 3). The E_{SC} of fresh human skin decreased from 139 MPa (35% RH) to 111 MPa (100% RH), but the E_{SC} of fresh porcine skin increased from 56 MPa (35% RH) to 67 MPa (100% RH). This opposite effect of decrease/increase in E_{SC} of human and porcine skin for increasing RH

indicated potential structural, compositional, and/or functional differences between human and porcine skin that influence moisture retention of the skin (especially at low RH) and its consequential mechanical properties (see Table 12 in page 160; $P = 0.007$. (2015). According to Silva et al. (2007), moisture is predominantly retained by the corneocytes of the SC at low RH, yielding a higher E_{SC}; whereas, both corneocytes and SC lipids swell substantially at high RH yielding a lower E_{SC} due to softening of the SC. This behavior was observed in human SC, but not in porcine SC (Table 3) [97].

Freezing affected human and porcine SC in different ways, highlighting potential structural and compositional differences between the two skin sources. A strong statistical significance was identified between skin source and state (Table 12 in page 160; $P < 0.0001$), as freezing decreased the mean E_{SC} for human skin from 124 MPa to 109 MPa; but increased the mean E_{SC} for porcine skin from 62 MPa to 101 MPa. After freezing, human and porcine skin yielded a similar mean E_{SC} at high RH (~111 MPa; Figure 17C), and that was also similar to the E_{SC} of fresh human skin, showing that porcine SC became a closer model to the human SC after freezing. The E_{SC} of most human skin samples decreased at 35% RH after freezing, but not at 100% RH. A possible explanation for the decrease in the E_{SC} of human skin due to freezing is structural damage caused by ice crystal formation to the SC, leading to disruption of the cell membranes and weakening of the intra-cellular bonds in the SC. The E_{SC} of porcine skin increased at both RH conditions after freezing, yielding a weak statistically significant relationship between the state of skin and RH (P=0.0194). The RH conditions did not influence the E_{SC} of human skin post-freezing, possibly due to the impact of the freeze-thaw cycle on the nature of and components involved in moisture handling by the SC. In contrast, the E_{SC} of porcine skin increased with freezing under both RH

conditions, which is likely due to differences in freeze-damage compared to human skin. A possible impact of ice crystal formation may be the rupturing of porcine corneocyte cell membranes during freezing, which hinders the water-retaining ability and reduces water-soluble hygroscopic materials in cells. According to Park and Baddiel (1972), such a destruction of the cell membrane resulting in loss of hygroscopic material can lead to the collapse of protein networks in the SC, providing a more compact structure with a higher elastic modulus [131]. More information on the statistically significant interactions between the different treatment methods tested in our study can be found on page 160.

2.3.2. Young's Modulus of Skin Composites

Microindentation of ED composites (SC layer removed) showed a significant difference in the E_{ED} between the human and porcine skin (Table 3; P=0.024). The RH did not affect the E_{ED} significantly when all human and porcine samples were considered (Table 3). However, increasing RH did appear to decrease the E_{ED} of only human skin from 1.46 MPa at 35% RH to 1.06 MPa at 100% RH (P<0.0001). Freezing increased the E_{ED} of human skin at 35% RH (P<0.001) and at 100% RH (P<0.0001), and of porcine skin samples at 100% RH (P=0.02); but not at 35% RH (P=0.95).

The $E_{FT,}$ which was similar in magnitude to previously published results [77, 80, 81], was not significantly influenced by skin type, state, or RH. A strong statistical significance was observed for the interaction between skin source and state on the E_{FT} (P < 0.0001). The E_{FT} of human skin increased from 1.31 MPa to 2.46 MPa after freezing; but decreased in porcine skin from 2.11 MPa to 1.37 MPa after freezing (Figure 17E). Although RH did not impact the E_{FT} across all skin

samples, a significant decrease in the E_{FT} from 1.69 MPa (35% RH) to 0.93 MPa (100% RH) was observed in fresh human skin ($P < 0.0001$), which followed a similar trend as fresh human SC (Figure 17C). The E_{FT} of human skin increased due to freezing, while the opposite was observed for the E_{FT} of porcine skin, indicating differences in the structural changes undergone in human and porcine skin during freezing.

The E_{ED} (Figure 17D) for fresh human skin followed the same trend as E_{SC} (Figure 17C) and E_{FT} (Figure 17E) as a function of RH, but the magnitude of change for E_{ED} was smaller. Thus, it is likely that the SC was dominant in the out-of-plane mechanical property of the FT skin. Similarly, in fresh porcine skin, the E_{SC} appeared to have a more prominent influence (compared to E_{ED}) on the E_{FT}, as E_{SC} and E_{FT} followed a similar trend as a function of RH. The E_{ED} of frozen human skin was lower than its E_{FT} by ~21% at both RH conditions (Figure 17E), directly showing the impact of the SC on the E_{FT}. The comparable trends for $E_{SC,}$ E_{ED}, E_{FT} of frozen human skin as a function of RH showed that freezing affected the skin layers in the same manner, and resulted in samples with out-of-plane mechanical properties that were unaffected by RH in their elastic range. In contrast, the E_{ED} of frozen porcine skin was higher than its E_{FT} by ~32% at 35% RH, and ~103% at 100% RH. Unlike for fresh porcine skin, the impact of the SC on the mechanical behavior of full-thickness frozen porcine skin remained unclear.

2.3.3. Microneedle Insertion Profiling

Quasi-static MN insertions into human and porcine skin provided key metrics to assess the in-plane mechanical behavior of skin (Figure 18A), including 1) stiffness S during initial contact between the skin and the MN; 2) force required to break the SC by a MN (F_{ins}), which correlated

with the ultimate tensile strength (UTS) of the SC [70]; and 3) D_{ins} of a MN from the skin surface until SC rupture (including the skin deflection during stress application). Quasi-static insertion of hollow metallic MNs led to the formation of mode-II cracks in the skin, which was confirmed by histopathological evaluation of the skin cross-section at the site of insertion (data not shown). A characteristic compressed column of tissue under the crack formed by the MN indicated a mode-II on the skin by blunt-tipped MNs.

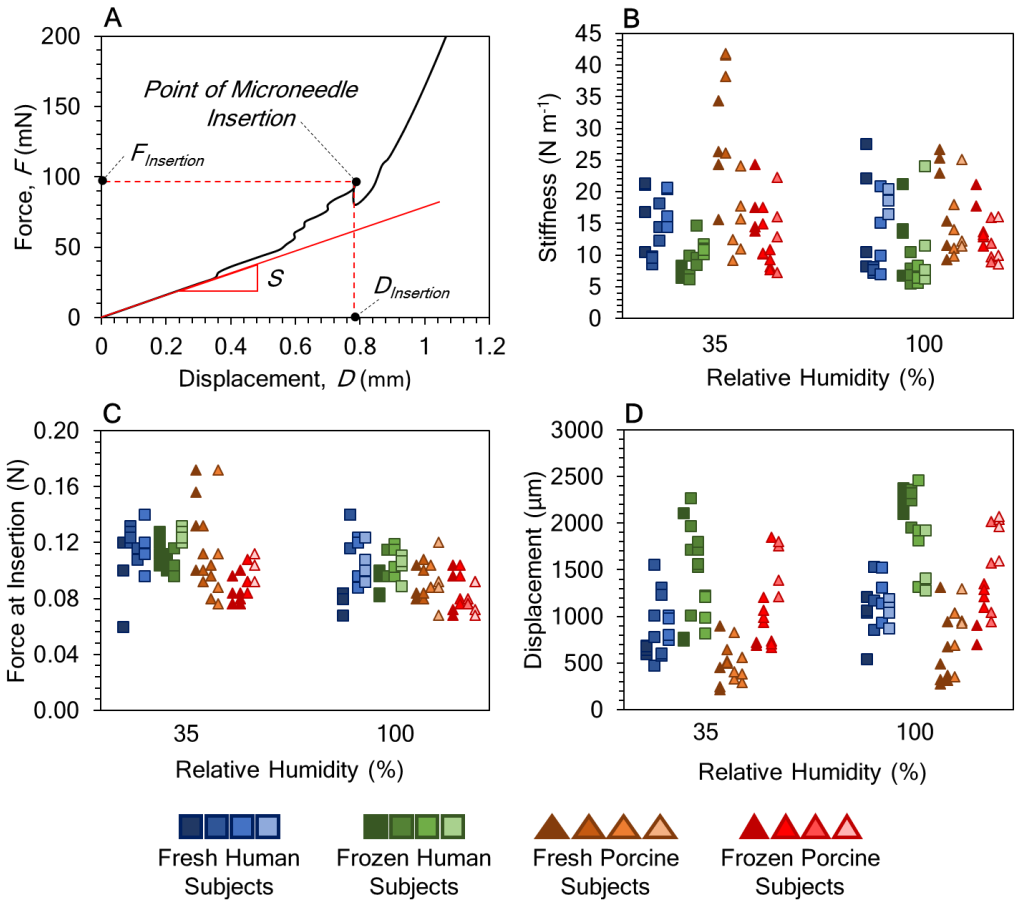

Figure 18. Microneedle insertion profiling in skin layers. (A) Force versus displacement data from a typical microneedle insertion profile was evaluated for stiffness (B), force of insertion (C), and displacement at insertion (D) parameters for human and porcine skin before and after freezing at -80 °C for 48 hours (four human and four porcine subjects tested at 35% and 100% RH; n=4 per subject per condition).

The integral of force over displacement at insertion yielded the work performed by a MN on skin to break the SC. The S, F_{ins}, and D_{ins} results obtained from MN insertions were plotted in Figure 18 for all skin specimens employed in this study. Due to significant subject-to-subject variability among human and porcine subjects, a three-factor factorial ANOVA (Table 14 in page 160) and a LSD analysis (Table 4) were conducted by pooling data from all four subjects per skin type into individual data sets.

Table 4. Effect of skin type, state, and relative humidity on the stiffness (N m^{-1}), force at insertion (N), and displacement at insertion (μm) during microneedle insertion into fresh and frozen human and porcine skins. The least significant difference (LSD, P=0.005) is provided for the treatments that significantly impacted the stiffness, force, and displacement values at a 95% confidence interval (indicated by superscripted a and b next to the mean value). The LSD is not provided if the F-value of treatment is not significant (NS).

Treatments		Stiffness (N m^{-1})		Force (N)		Displacement (μm)	
		Mean	**SD**	**Mean**	**SD**	**Mean**	**SD**
Source	Human	16.96^{a}	0.52	0.107^{a}	0.017	1343.40^{a}	550.93
	Porcine	12.33^{b}	8.31	0.096^{b}	0.023	912.40^{b}	500.24
	LSD	2.17		0.007		130.87	
State	Fresh	17.55^{a}	8.24	0.107^{a}	0.025	793.40^{a}	355.06
	Frozen	11.74^{b}	5.03	0.096^{b}	0.015	1462.40^{b}	542.88
	LSD	2.17		0.007		130.87	
Relative Humidity	35%	15.65	8.46	0.107^{a}	0.023	969.78^{a}	498.25
	100%	13.64	6.60	0.096^{b}	0.019	1286.02^{b}	590.82
	LSD	NS		0.007		130.87	
CV (%)		43.32		18.18		33.51	

Major differences between microindentation and MN insertion lie in the scale of the indentation devices and orientation of deformation yielding mechanical responses. Both MN and microindentation tip impart a compressive stress onto the skin sample in a region similar to their

contact area. As the skin is being compressed, an in-plane tensile stress develops in the skin around the circumference of the indentation devices, in particular in the SC. Due to their very different diameters of 30 μm for the MN and 890 μm for the microindentation probe, the surface area-to-circumference ratios of the microindentation probe is 30 times larger than that of the MN (Figure 17A). Hence, the mechanical response measured by the MN corresponds more to the tensile stress in the SC around its circumference while the response measured by the microindentation probe is mainly caused by skin compression achieved with its relatively larger contact surface. It is suspected that during MN insertion, the impact of corneodesmosomes, a class of proteins responsible for ensuring cell-to-cell adhesion in the skin, on the mechanical strength of skin were more likely captured by the MN tip than during microindentation [134]. A MN tip likely deformed the skin directly on or very close to tight junctions that are formed by corneodesmosomes between corneocytes in the SC to contribute immensely to its mechanical and extreme-barrier properties [135]. They undergo degradation due to proteolytic activity of enzymes and inhibitors, affecting the localized mechanical properties of skin that impact MN insertions. Their degradation is dependent on surrounding humidity and moisture content in skin, and can be facilitated by freezing [136].

The mean S of human skin tested during MN insertions was significantly higher (16.96 N m^{-1}) than that of porcine skins (12.33 N m^{-1}; Table 4; $P<0.0001$), which agreed with the E_{SC} results (Figure 17C). In fresh porcine skin, S decreased by 36% (from 24.4 N m^{-1} at 35% RH to 16.1 N m^{-1} at 100% RH; $P<0.01$), due to swelling of corneocytes and SC lipids during hydration; such a significant decrease was not observed in fresh human skin. The stiffness S of fresh human and porcine skin was significantly different at lower RH (9.1 N m^{-1} difference; $P=0.0044$), but not at

higher RH (1.7 N m^{-1} difference; P=0.45), showing that high RH facilitated similar localized behavior in both fresh human and porcine skin. RH did not impact *S* in frozen skins. Freezing decreased the *S* of human and porcine skins from 17.55 N m^{-1} (fresh) to 11.74 N m^{-1} (frozen), clearly indicating freezing-induced disruption of the SC structure. In contrast, freezing increased the E_{SC} during microindentation (Table 3), which suggested that there are major differences between in-plane and local mechanical responses versus out-of-plane and bulk mechanical responses of the skin due to freeze-damage. The decrease in the localized stiffness of skin after freezing is attributed to corneodesmosomal degradation, which compromised the integrity of cellular junctions in the SC.

The mean F_{ins} obtained in this study ranged between 0.104-0.111 N for human skin and 0.083-0.118 N for porcine skin, and was similar in magnitude (0.1-3 N) to a number of previous studies [84, 110, 112]. This F_{ins} was significantly affected by all sample attributes explored in this study – skin type, state, and RH (Table 14**;** P<0.0001). A significant interaction between the skin type and state (P=0.02) showed that freezing decreased the F_{ins} in porcine skin from 0.105 N (fresh) to 0.086 N (frozen), but did not affect the F_{ins} in human skin. F_{ins} decreased significantly as a function of RH for all skin samples from 0.107 N (35% RH) to 0.096 N (100% RH); but, in individual skin groups, decreases in F_{ins} with increasing RH were not significant. The overall decrease in F_{ins} for fresh human and porcine skin followed similar trends as those measured for *S* (Figure 18C) and was correlated with the UTS of fresh human and porcine skin [70]. The influence of RH on in-plane mechanical properties of skin differed from out-of-plane properties. Since MN insertions applied in-plane stress (tension) on the skin, and corneocytes in the viable epidermis and the SC are naturally stacked on top of each other in an out-of-plane orientation (similar to a brick-mortar

structure; Figure 17A), the layers appear to provide lower rigidity and more flexibility in-plane. This arrangement of the corneocytes allowed them to slide on and pass each other during in-plane deformation (during MN insertion), which is facilitated by hydration [73]. In human samples, the F_{ins} of frozen skin remained unaffected by RH compared to the fresh state, while the F_{ins} decreased slightly in frozen pig skin by ~21% (35% RH; P=0.003) and ~24% (100% RH; P=0.09). This could be attributed to the slightly higher moisture retention in porcine skin (35-68% by volume [99]) compared to human skin (24-67% by volume [104]) especially at physiological, low-humidity conditions and the effect of freezing on the degradation of corneodesmosomes in the SC [136].

The D_{ins} of a MN was significantly affected by skin type, state and RH condition (P<0.0001 for all treatments; Figure 18D; Table 4**).** The D_{ins} were significantly higher for human skin (1343 μm) than porcine skin (912 μm). Freezing of skin yielded a higher D_{ins} (1462 μm) across all skin samples compared to the fresh state (793 μm), resulting in softening of the skin (lower *S*, F_{ins}, and D_{ins} compared to fresh skin). Similarly, the D_{ins} increased as a function of RH for all skin types, due to the swelling of cells in the skin structure, leading to softening of the skin. The relationship between the *S*, F_{ins}, and D_{ins} was mostly that the skin sample with the highest *S* required the highest F_{ins}, and the lowest D_{ins}. As the skin sample with the highest *S* and F_{ins}, fresh porcine skin yielded the lowest D_{ins} range (0.49-0.72 mm). Similarly, the order of D_{ins} from low to high followed fresh human skin (0.86-1.11 mm), frozen porcine skin (1.09-1.35 mm), and finally frozen human skin (1.53-1.97 mm).

The work or energy (E_{ins}) required to break the SC of the skin (estimated as one half of the product of F_{ins} and D_{ins}) showed that E_{ins} increased due to freezing in human and porcine skin. In fresh

human skin, the mean E_{ins} were 0.05 mJ (35% RH) and 0.06 mJ (100% RH); while freezing increased the E_{ins} to 0.09 mJ (35% RH) and 0.10 mJ (100% RH). Similarly, in fresh porcine skin, the E_{ins} were 0.03 mJ (35% RH) and 0.04 mJ (100% RH); while freezing increased the E_{ins} to 0.05 mJ (35% RH) and 0.06 mJ (100% RH). In all skin samples, the E_{ins} decreased with increasing RH, indicating an overall softening of the skin due to hydration facilitating the MN insertion process. In all conditions, human skin yielded higher E_{ins} compared to porcine skin, demonstrating differences in the mechanical properties between the two species.

A limitation of this MN insertion study was the lack of utility of the subcutaneous and subsequent soft tissue layers beneath the skin that may impact MN insertion. It is suspected that a softer tissue underneath the skin will impact the force-displacement profile during MN insertion, likely by reducing the F_{ins} and increasing D_{ins}. This needs to be experimentally tested in the future. Skin mechanical properties were characterized under quasi-static conditions at 22 ^{o}C; therefore, it is expected that under dynamic conditions and human physiological temperature (37 ^{o}C) , mechanical responses by the skin to deformation may be different.

2.4. Conclusions

This study aimed for the first time to show a direct comparison of the mechanical properties of human and porcine skin before and after freezing, demonstrating the impact of freezing on mechanical changes that occur in skin, such as decreasing the stiffness and increasing the total energy required to break the SC. The methods used (microindentation and MN insertion profiling) helped to identify and to compare both bulk and localized mechanical properties of skin layers, while also providing insight into how human and porcine skin behave at different moisture levels,

which is one of the key external stimuli influencing skin mechanics. The use of low and high RH conditions to assess the mechanical characteristics of each skin sample provided information on potential avenues to manipulate skin mechanical properties to match that of fresh human skin. The findings suggested that for MN research, in the absence of fresh human skin, using fresh porcine skin at high humidity conditions might present a more suitable skin model (with more comparable mechanical properties to fresh human skin) than frozen human skin. This study provides a reference for mechanical studies involving skin that are challenged by difficulties obtaining fresh human skin, and aids in selecting the appropriate specimens for various mechanical tests.

3. DEVELOPMENT OF AN ARTIFICIAL MECHANICAL SKIN MODEL FOR MICRONEEDLE INSERTION ASSESSMENT

It is extremely challenging to obtain tissue with repeatable mechanical properties for mechano-analysis. AMSMs, especially non-biological polymeric models that can mimic the mechanical characteristics of human skin, are beneficial to address the challenges and drawbacks associated with studies with biological skins, including the limited availability of fresh human skin, the need for skin stretching to its in vivo configuration, and concerns regarding the safety of handling. The purpose of this chapter is to develop an AMSM using polymeric materials, which can be used in place of human skin.[2] The AMSM is validated by comparing its mechanical characteristics to fresh human skin and porcine skin (the closest biological substitute for human skin), and by comparing the interaction between MNs and the skin model. The main goals for the AMSM in this study are: i) a high repeatability of mechanical characteristics, ii) the ease of access to materials and fabrication, and iii) high resistance of the AMSM to the insertion of MNs when compared to the highest forces required for human and porcine skins, such that it represents tougher skin samples. The AMSM presented in this chapter will allow the development of repeatable and optimized MN insertion methods into skin at controlled depths, speeds, and forces as they relate to MN design and insertion parameters. Furthermore, the availability of a validated AMSM will provide a

[2] A version of chapter 3 has been published:

Ranamukhaarachchi S.A., Schneider T., Lehnert S., Sprenger L., Campbell J.R., Mansoor I., Lai J.C., Rai K., Dutz J., Häfeli U.O., Stoeber B. Development and Validation of an Artificial Mechanical Skin Model for the Study of Interactions between Skin and Microneedles. Macromolecular Materials and Engineering. 2016 Mar 1;301(3):306-14.

standardized substrate to compare the performance of different MNs and other skin puncturing devices made using different technologies.

3.1. Experimental Section

3.1.1. Biological Skin Preparation

Biological skin samples were prepared as described in Section 2.2.1.

3.1.2. Artificial Skin Preparation

Two PDMS kits were used to prepare the AMSM: the two-component Sylgard 184 kit (Dow Corning, MI, USA) for the SC, and the three-component TC-5005 A/B/C (BJB Enterprises Inc.; Tustin, CA, USA) for the ED layers. Sylgard 184 PDMS base: cross-linker weight ratios of 5:1, 10:1 and 20:1 were used during film preparations for the SC. Each PDMS composition was spin coated on glass substrates at 250-3,000 rpm, and incubated at 65^{o}C for 3 h for curing. A TC-5005 A/B/C base: cross-linker weight ratio of 10:1 was used to prepare the films, with the third part (part C) being added up to 50% *w/w* to partially inhibit the curing process of the films, which increases the compliance of the film. PDMS mixtures were poured onto previously surface-silanized glass substrates to achieve 200 µm thick films, and cured at room temperature for 24 hours.

3.1.3. Micro-indentation of Skin Samples

Micro-indentation tests were performed as described in section 2.2.2. Each micro-indentation experiment on a skin sample from one subject was repeated nine times at different indentation locations (n=9).

3.1.4. Tensile Testing of the Stratum Corneum

The SC layer of human and porcine skins was subjected to tensile testing to determine their in-plane Young's modulus (E_T) and the UTS. Tensile testing was performed according to the ASTM D412 protocol at 35% RH and 100% RH, and at 22 ^oC using a Q400 TMA instrument with a film/fiber probe. Each tensile experiment was repeated five times per skin sample (n=5). Quasi-static tensile conditions at 22 ^oC were selected over dynamic conditions and human physiological temperature, due to the ease of control of the test conditions.

3.1.5. Microneedle Insertions Profiling

Single MN insertions onto FT skin samples were performed as described in Section 2.3.3. Each MN insertion experiment was repeated five times (n=5).

3.2. Results and Discussion

3.2.1. Stratum Cornea of Biological Skins

The SC is the most important layer of the skin for applications using MNs. Thus, identifying an artificial material similar in its mechanical properties to the SC layer and with subsequent layers acting as support material is therefore a priority in this work. The Young's modulus provides an indication of a material's stiffness (resistance to deformation under stress), and is one of the most important mechanical properties of a material. Skin layers are heterogeneous materials and are assessed under stress perpendicular (out-of-plane) and parallel (in-plane) to the surface to determine their Young's moduli.

The E_{SC} of human skin (140 MPa ± 38 MPa at 35% RH and 112 MPa ± 51 MPa at 100% RH MPa) was greater than porcine skin (57 MPa ± 23 MPa at 35% RH, and 67 MPa ± 19 MPa at 100% RH)

at both RH conditions tested (Figure 19C). The E_{SC} for both human and porcine skins reported herein were comparable to those found in literature (Table 1) and in chapter 2. In human SC, an increase in the RH led to a significant decrease in the mean E_{SC}, but a significant change in the mean E_{SC} is not observed in porcine skin with increasing RH.

The in-plane Young's modulus, E_T, was measured as 7.3 MPa ± 6 MPa (100% RH) and 43.8 MPa ± 51 MPa (35% RH) for human SC, and 18.8 MPa ± 16 MPa (100% MPa) and 19.6 MPa ± 15 MPa (35% RH) for porcine SC (Figure 20B). The E_T of human SC was influenced by the RH conditions in a similar way as the E_{SC} – as the RH decreases, the Young's modulus increased as well (see later discussion). This observation did not hold true for porcine SC, which appeared to be unaffected by the RH. The E_T for human SC reported herein were comparable to values reported in the literature (Table 1) [72, 73].

The ultimate tensile strength, UTS, ranged between 0.3-5.1 MPa at 35% RH and 0.5-3.9 MPa at 100% RH for human SC; and between 0.5-6.4 MPa at 35% RH and 1.1-4.3 MPa at 100% RH for porcine SC (mean UTS values shown in Figure 20C). The UTS of both human and porcine SC appeared unaffected by RH conditions. The strain at break (Figure 20A) increased with RH for both human and porcine SC.

The human skin samples displayed a wide range in E_{SC} (34.1-223.4 MPa across 72 measurements from four human subjects at 35-100% RH) and E_T (1-179 MPa across 40 measurements from four human subjects at 35-100% RH). The inter-subject variability in the data was large and unavoidable due to innate variability in the human skin samples. Therefore, we pooled all data for each skin source (i.e., human and pig) into individual data sets at a given RH condition. Although

the range of E_T of human SC is similar to the E_{SC}, assessing the mean E_T and E_{SC} confirmed the anisotropy of the human SC.

The RH affected the E_{SC} and E_T (high RH decreased the modulus) of human SC, which was in good agreement with chapter 2 and previous work[73, 137, 138] The prominence of the decrease in the modulus due to hydration is more visible in E_T (Figure 20B) than E_{SC} (Figure 19C) for human SC, which suggested a softening of the skin with increasing humidity. It can be argued that the effects of hydration on structural changes to the SC were more drastic in-plane when compared to out-of-plane, including the disruption of the intercellular lipid structure and increasing the mobility and sliding of corneocytes past each other [73, 139] Other reasons for softening of skin due to humidity includes swelling of corneocytes, degradation of corneosome proteins, and potentially fluidizing the lipids surrounding the cells.

Porcine SC samples yield relatively narrow ranged values for the E_{SC} (13.2-113.9 MPa across 72 measurements from four pigs at 35-100% RH) and the E_T (4.0-57.0 MPa across 20 measurements from the same 4 pigs) compared to human SC. These narrower ranges were expected due to the similarity among the different porcine skin samples tested, which were obtained from pigs of the same age, grown under similar environments, and from the same location within the pig (abdomen). The E_{SC} of porcine and human skin was higher than the E_T (confirming the anisotropy), due to extremely compact stacking of terminally-differentiated corneocytes on top of each other. Naturally-occurring out-of-plane orientation of corneocytes provided higher rigidity and lower flexibility compared to the in-plane orientation of the corneocytes, where corneocytes can slide on each other to facilitate elastic and inelastic deformations. The RH did not influence the E_{SC} and

the E_T of porcine SC significantly, which agreed with Wu et al. (2006), who showed that a combination of temperature and RH (rather than RH alone) affected the mechanical properties of porcine SC in-plane. This also hinted at the differences between human and porcine SC in their interactions with moisture and how moisture is absorbed onto the tissue, as described in chapter 2.

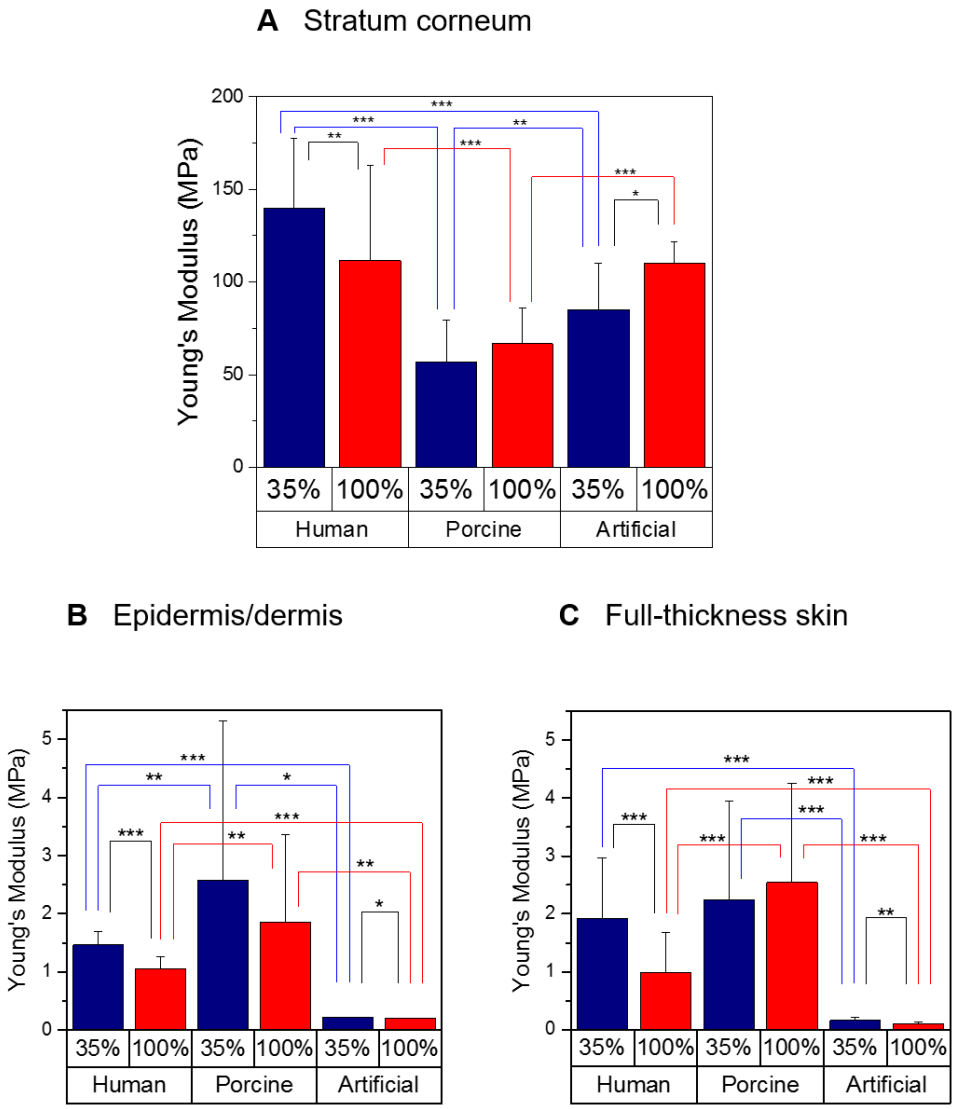

Figure 19. Microindentation of skin layers to determine their out-of-plane Young's modulus for artificial skin model development. Out-of-plane Young's moduli of stratum corneum (A), epidermis/dermis composites (B) and full-thickness skin composites (C) from fresh human upper abdominal skin samples (n=36 across 4 human subjects), fresh porcine abdominal skin

(n=36 across 4 pigs), and artificial mechanical skin model (n=9) at 35% and 100% RH conditions (error bars represent standard deviations; level of significance and significant differences at α = 0.05 between means of groups are identified with asterisks and brackets, respectively; P<0.05 *, P<0.01 **, P<0.001 *).**

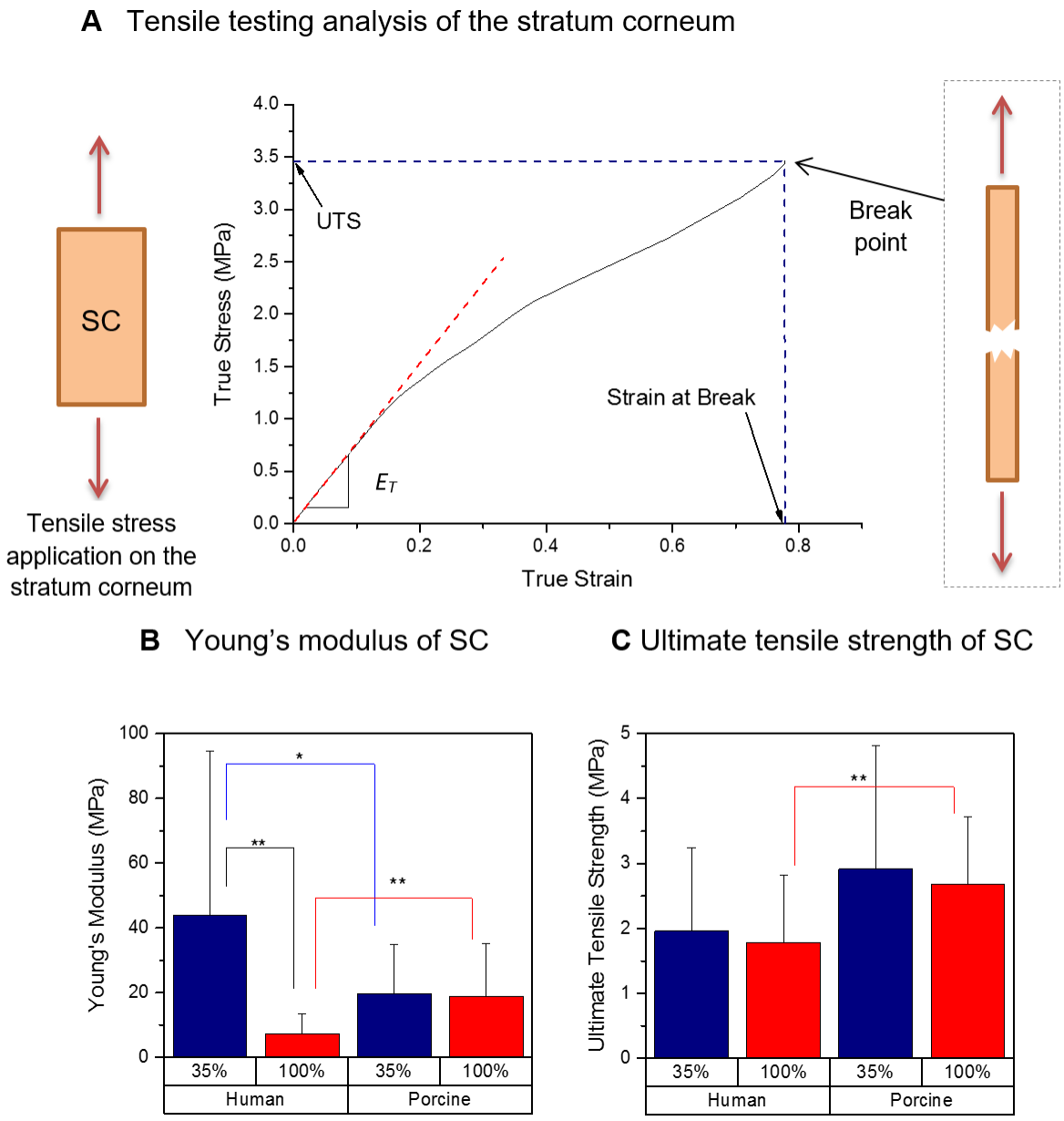

Figure 20. Tensile testing of stratum cornea to determine their in-plane mechanical properties. Orientation of tensile stress application, data collection, and analysis using a true stress-true strain plot (A); mean in-plane Young's moduli (B); and ultimate tensile strength (C) of stratum corneum from fresh human upper abdominal skin samples (n=20 across 4 human subjects), and

fresh porcine abdominal skin (n=20 across 4 pigs) at 35% and 100% RH conditions (error bars represent standard deviations; level of significance and significant differences at α=0.05 between means of groups are identified with asterisks and brackets, respectively; P<0.05 *, P<0.01 **, P<0.001 *). See Supporting Information for more on the analysis.**

3.2.2. Stratum Corneum of the Artificial Skin Model

PDMS was selected as artificial material to simulate the mechanics of the human SC due to its availability, low cost, ease of fabrication, hydrophobicity, transparency, and the ability to change the mechanical properties over a wide range of Young's moduli by varying the material composition. Other material candidates considered for the artificial SC included polyurethane [115] and Parafilm M®[116] Using the two-component Sylgard 184 PDMS kit, a 18 μm film was prepared at a 10:1 ratio (base: cross-linker) to represent the human SC due to mechanical similarity and for repeatability during processing and curing.

The mean E_{SC} of PDMS at the 10:1 composition ranged from 85 MPa ± 25 MPa at 35% RH to 110 MPa ± 11 MPa at 100% RH (Figure 19C) and was similar in the range to human SC. The mean E_T of the 10:1 PDMS mixture ranged between 0.45 MPa (1 mm thickness) to 1.34 MPa (18 μm), which were in agreement with Liu et al. (2009) [140]. The anisotropy of PDMS films at ~20 μm thickness was similar to biological SC and it was imparted by spin-coating. Spin coating of PDMS subjected its polymer chains to shear forces, which led to the reordering of chain alignment to straightened chains, providing stronger cross-linked networks and higher modulus responses [140].

The UTS of the 10:1 PDMS composition ranges from 4.2-5.6 MPa (18 μm), which was similar to human and porcine SC (Figure 20C). The UTS is an important parameter for simulating the SC as it is the stress at which the SC fails. It is related to the point at which a MN exerts sufficient stress

on the SC to form a crack to pierce through the skin layer, characterized by determining the MN insertion force (see later discussion, in Figure 21C). To simulate tougher human skin with the AMSM, a PDMS-based SC with UTS comparable to the highest value measured for human SC was chosen, as reflected in Figure 21C, where AMSM required higher MN insertion forces than those found with average human and porcine skins.

3.2.3. Multi-layered Skin Composites

The three-component TC-5005 A/B/C PDMS kit allowed simulation of the mechanical properties of the viable epidermal and dermal layers of human skin (Table 1). As the viable epidermal and dermal layers in skin could not be individually isolated without the utility of chemicals or enzymes, their individual E_{OP} were not experimentally determined in this study. Thus, literature values were used to compose the simulant layers using the three-component PDMS kit. The Young's modulus of the viable epidermis had not been adequately quantified in literature, and the only estimation of approximately 0.66 kPa was provided by Hendriks et al. (2006) using a finite element model [69]. Since the viable epidermis is significantly lower in stiffness compared to the SC and dermis, it was considered to have a negligible effect on the overall skin mechanics [141]. The viable epidermis was recreated using a 200 µm film made of 52 wt% part C of the PDMS kit, providing a Young's modulus of ~9 kPa (lowest possible stiffness achieved). The dermal layer was simulated using a 1 mm film of 47 wt% part C, providing a Young's modulus of ~60 kPa, similar to the human

dermis [69, 75]. Other materials considered for the ED composite includes agarose- and gelatin-based hydrogels.

Human ED composite samples resulted in E_E between 1.1 MPa ± 0.2 MPa (100% RH) and 1.5 MPa ± 0.2 MPa (35% RH), while porcine ED samples resulted in E_{ED} between 1.9 MPa ± 1.5 MPa (100% RH) and 2.6 MPa ± 2.7 MPa (35% RH), as shown in Figure 19D. Increasing the RH decreased the E_{ED} of both human and porcine ED samples. In comparison, the ED composite of the AMSM (without the SC layer) yielded a mean E_{OP} between 206 kPa ± 1.1 kPa (100% RH) and 227 kPa ± 1.8 kPa (35% RH), which were significantly lower than both human and porcine ED.

E_{FT} of human full-thickness skin composite were 1.9 MPa ± 1.0 MPa (35% RH) and 1.0 MPa ± 0.7 MPa (100% RH), while porcine ED samples resulted in E_{FT} between 2.2 MPa ± 1.7 MPa (35% RH) and 2.5 MPa ± 1.7 MPa (100% RH), which were comparable to chapter 2. The FT composite of the AMSM yielded E_{FT} between 161 kPa ± 50 kPa (35% RH) and 97 kPa ± 37 kPa (100% RH), which were significantly lower than both human and porcine FT (Figure 19E), but were comparable to values presented in Table 1 [77-79]. The presence of SC in the FT skin composite did not influence the E_{FT} of human and porcine skins in the tested samples, even though the effect of the SC on FT mechanics was observed previously in chapter 2.

The ability to separate the viable epidermis and the dermis into two separate layers from biological skin samples without the use of chemical means would have allowed adjustments of the AMSM's ED composite to reflect biological skins more accurately. Given that the application of MN insertions was mainly focused on the mechanics of the SC layer (not the ED or FT skins), it was important to verify that the AMSM performs similar to biological skins in MN insertion profiling.

3.2.4. Microneedle Insertion Profiling

The AMSM yielded higher mean F_{ins} compared to human and porcine skins, which were similar under the tested RH conditions (Figure 21Ci). However, observing individual F_{ins} data points suggested that the forces required to pierce the SC of the AMSM (132-188 mN force range) by a single MN were at the higher end of the force range for human skin (60-176 mN) and in the mid-range for porcine skin (68-333 mN), which successfully represented a tougher human skin sample. This is a key advantage of the AMSM as a simulant for tough human skin, because the ability of a MN to penetrate through the SC of the AMSM would ensure that the MN will pierce the SC of biological skins successfully, which is vital to MN performance. The F_{ins} values reported herein were similar to the ones reported in chapter 2. The F_{ins} followed a similar trend to the UTS of their corresponding SC. This similarity confirms the correlation between the mechanical characteristic of the SC (UTS) and how it is reflected during the transdermal MN application (MN insertion force).

The D_{ins} (considering the deflection of skin due to stress application by the MN and the distance travelled by the MN into the skin) in human skin and AMSM ranged between 0.46-1.85 mm and 0.38-1.74 mm, respectively (mean D_{ins} provided Figure 21Cii); and were similar to the D_{ins} presented in chapter 2. These ranges overlapped each other, demonstrating the overall similarity of the AMSM to human skin. The D_{ins} was influenced by the RH conditions for porcine skin and for the AMSM, but not for human skin. As the skin absorbed moisture at high RH, it was expected that skin softening would lead to its increased flexibility and, thus, the skin would deform more prior to fracture (Figure 21A). A decrease in RH was expected to stiffen the skin, causing the point of MN insertion to shift horizontally to the left from the point indicated in Figure 21B, with or

without affecting the force of insertion, because the UTS of human and porcine SC was not affected by the RH. For porcine and artificial skins, this assumption held true, as increasing the RH (hydration) led to higher D_{ins}, even though RH did not affect the F_{ins}. Such a result was not observed for human skin, even though E_T and E_{SC} of human skin decreased due to hydration. The mean D_{ins} were significantly different between AMSM and human skin at 35% RH, but not between AMSM and porcine skin. Porcine skin and human skin were different at 35% RH, but not at 100% RH.

The *S* response during the initial contact of the MN with skin showed that there was no significant difference between AMSM (11-15 N m^{-1} range) and human skin (14-15 N m^{-1} range), and between AMSM and porcine skin (16-24 N m^{-1} range; mean *S* shown in Figure 21Ciii). The only significant difference in stiffness was seen between human and porcine skins at 35% RH, which further suggested differences in mechanical responses perpendicular to the surface between the two skin types. The difference between the *S* and out-of-plane Young's modulus using the microindentation approach was simply the indenter dimensions, as described in section 2.3.3.

Since biological and artificial skin mechanical properties were characterized under quasi-static conditions at 22 ^{o}C; it is expected that mechanical responses by the skin to deformation may be different under dynamic conditions and human physiological temperature (37 ^{o}C).

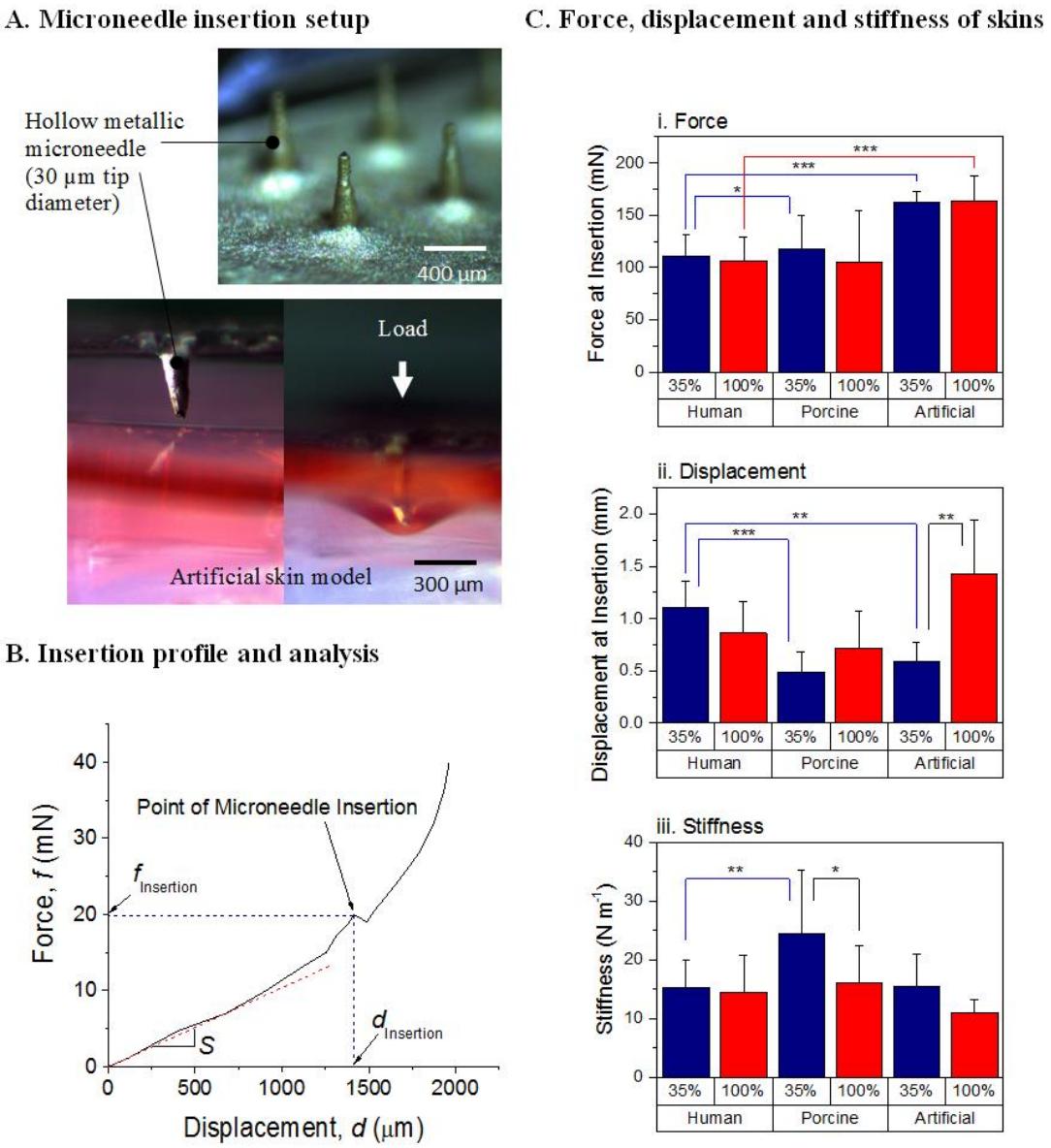

Figure 21. Microneedle insertion profiling on human, porcine, and artificial skins to compare mechanical characteristics. The skin structure and the experimental setup for microneedle insertions (A); microneedle insertion profiling and analysis where force-displacement data were collected, and microneedle insertion points were identified (B); and mean force at insertion, displacement at insertion, and stiffness during impact (C) of a single hollow metallic MN onto full-thickness skin from human upper abdomen (n=20 across 4 human subjects), porcine abdomen (n=20 across 4 pigs), and artificial mechanical skin model (n=5) at 35% and 100% RH conditions (error bars represent standard deviations; level of significance and significant differences at α = 0.05 between means of groups are identified with asterisks and brackets, respectively; P<0.05 *, P<0.01 **, P<0.001 *).**

3.3. Conclusions

The mechanical measurements reported herein (E_{OP} and E_T, UTS, MN insertion force, displacement, and stiffness) validate the AMSM as a suitable mechanical model for fresh human skin for material characterization and MN application. This is the first skin model reported that has its mechanical properties carefully compared to fresh human and porcine skin samples, and that has been validated by mechano-analysis and application-driven analysis to be similar to tough human skin. Selected materials for modelling the skin layers and the actual biological skin layers are characterized using multiple, yet identical mechanisms (instrument, technique, conditions, and protocol) for validation. The polymeric materials produce lower mechanical variability and higher mechanical repeatability compared to biological skins. The validated AMSM with respect to human skin provides a much-needed substrate to replace the use of biological skins in transdermal medical device design, development, and performance evaluation. The AMSM can now be used as a standardized substrate to test and compare the insertion profiles of other available MN devices, which will provide great insight into the development and performance of transdermal drug delivery devices.

4. KEY FACTORS INFLUENCING DYNAMIC MICRONEEDLE INSERTIONS

A number of studies have been conducted to date to study MN insertions [55, 84, 115], but have not assessed several key parameters that affect successful and repeatable MN injections, including energy and velocity required to insert the MNs. The main objectives of this chapter are to assess the dynamics of MN insertion, and to determine the key factors that contribute to successful penetration of MN into the ASMS from chapter 3.[3] The force and energy required to break the SC are evaluated using a spring-loaded MN applicator at large input energies and velocities of impact. In addition, the influence of MN geometry (i.e., tip diameter) and number of projections in an array on the insertion process into skin are assessed. The findings from this study will provide guidelines for successful MN insertion into human skin.

4.1. Materials and Methods

4.1.1. Microneedles and Skin Model

Hollow metallic MNs were fabricated as described in section 1.2.1.2, using a metal electrodeposition process to obtain single MN devices (1-MN) with heights of 700 ± 38 µm and tip outer diameters (OD) of 60 ± 11 µm, 100 ± 14 µm, and 120 ± 15 µm [16]. Further, hollow MN arrays consisting of 6 MNs (6-MN) of 700 ± 38 µm height and 100 ± 14 µm OD arranged in a

[3] A version of chapter 4 has been prepared for publication:

Ranamukhaarachchi S.A., Jayatilake H., Häfeli U.O., Stoeber B. Determining the factors affecting dynamic insertion of microneedles into skin.

hexagonal fashion and 19 MNs (19-MN) of 700 ± 38 µm height and 100 ± 14 µm OD arranged in a concentric layout (central MN surrounded by two rings of 6 and 12 MNs) were fabricated. The MNs were bonded to a plastic female Luer connector, which can be mounted to standard syringes with male Luer connectors.

An artificial mechanical skin model, previously designed and validated against human and porcine skin samples in chapter 3, was employed to assess MN insertions.

4.1.2. Microneedle Insertion Setups

Quasi-static MN insertions were performed using a Q400 thermomechanoanalyzer (TMA; TA Instruments, DE, USA) as described in 2.2.3.

Dynamic MN insertions into the skin model was performed using a custom-built setup (Figure 22). The spring-loaded MN insertion device included a Luer attachment for MN arrays (1-MN, 6-MN, or 19-MN). A locking mechanism (Figure 22) with grooves allowed setting different spring compression levels at the beginning of an experiment with compression levels ranging from 4 to 20 mm at 4 mm increments to set different levels of total energy for the insertion system. The spring used in this study (spring #111; k=266 N m^{-1}) was purchased from WB Jones Springs Co. Inc. (KY, USA).

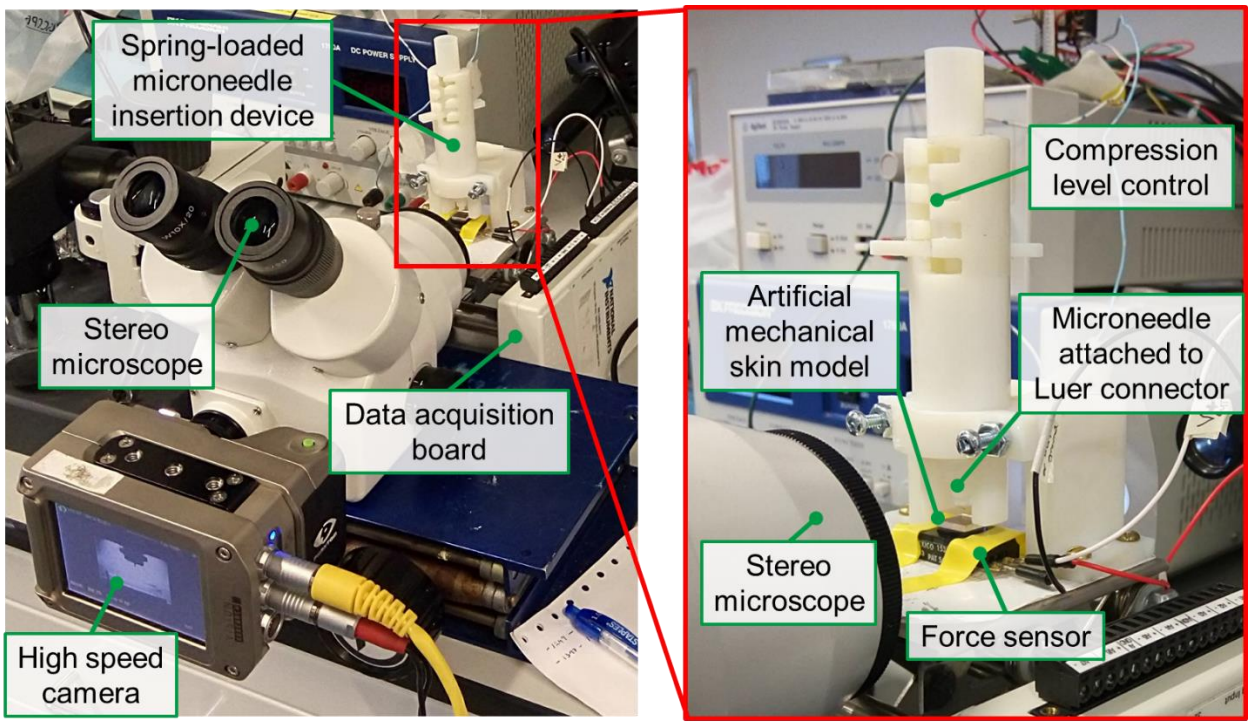

Figure 22. Dynamic microneedle insertion setup. The setup includes a high-speed camera connected to a stereo microscope for image acquisition; a spring-loaded device for MN insertion; an artificial mechanical skin model on a force sensor that is connected to a data acquisition board to acquire and save force data during MN insertion. The spring-loaded MN insertion device consists of multiple levels of spring compression providing control for the energy introduced to the MN insertion. The MN-Luer device is attached to the spring-loaded insertion device.

4.1.3. Dynamic Microneedle Insertion Procedure

Prior to MN insertion, the insertion device was aligned with the surface of the skin model on the force sensor (FS01 piezo-resistive force sensor, Honeywell, NJ, USA). This was done to ensure that the resting position of the spring occurred where the MN was fully inserted into the skin, while the MN base was barely in contact with the skin model. The spring was then compressed to a pre-defined level on the device between 4 mm to 20 mm (Figure 23A), and released to actuate the MN onto the skin model to perform the insertion (Figure 23B). When releasing the spring, data capture

from the force sensor was started at a frequency of 100 kHz using a LabVIEW virtual instrument (National Instruments, TX, USA), along with image capture (208x200-pixel image size) at 10,000 fps using a Phantom Miro 310 high-speed camera and the Phantom Camera Control software (Vision Research, NJ, USA). A light source, illuminating the MN device and the AMSM from the back, provided a silhouette view of the MN insertion, as shown in the bottom left corner of Figure 22, in the view finder of the high-speed camera. The force data capture was triggered by the image acquisition, which provided synchronization of the data from the two sources.

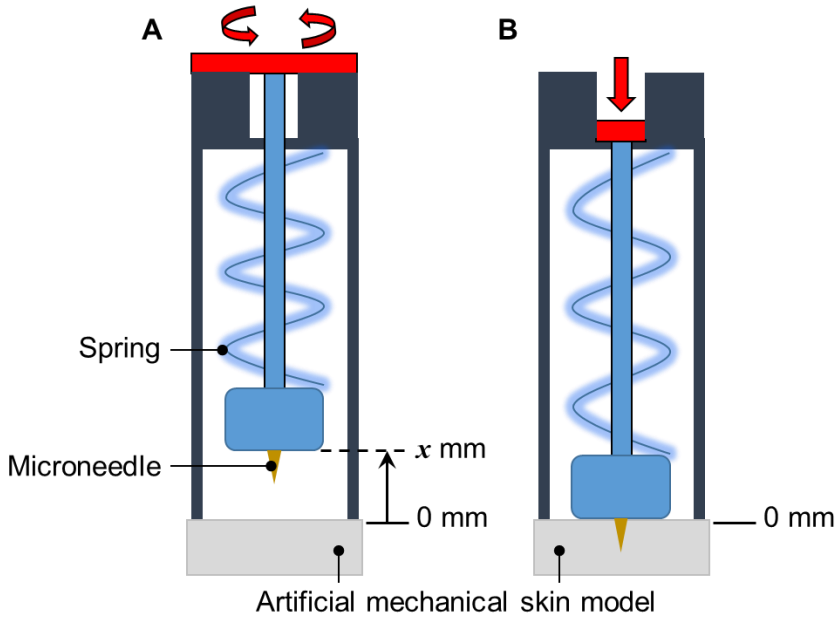

Figure 23. Dynamic microneedle insertion steps. (A) The spring inside the insertion device is compressed to a pre-defined level (x) to input energy into the system and locked in position by a rotation mechanism. (B) The spring is released by rotation causing microneedle actuation on to the artificial mechanical skin model.

4.1.4. Data Processing and Analysis

The force data recorded was used as-is during the analysis, while the captured images were further processed using MATLAB (MathWorks, MA, USA), and used to determine the MN displacement

as a function of time. Each image, captured originally in grayscale, was converted to a binary image based on a threshold of 0.25, which was determined based on the sensitivity of image artifacts to the binary threshold. All pixels in the grayscale image with brightness values greater than the 0.25 threshold were replaced with 1 (white), while all other pixels were replaced with 0 (black). As the MN moved towards the skin frame-by-frame, the reduction in the total number of white pixels allowed direct calculation of pixel displacement. The displacement in pixels were converted to millimeters using a calibration measurement. Since force data was captured at a 10-fold higher frequency than the image acquisition, the displacement data was interpolated to match the force data using the piecewise cubic hermite interpolating polynomial (PCHIP) function on MATLAB. Velocity was calculated from the difference in displacement as a function of time.

4.1.5. Microneedle Insertion Experiments

4.1.5.1. Effect of Velocity and Energy on Microneedle Insertion

Several MN insertion experiments were conducted per the factorial design (Table 5). The 120 µm OD 1-MN device was predominantly used to identify the key factors affecting MN insertions. Using the energy balance equation, the initial energy of the system (E_o) was calculated from the spring constant *k* and spring compression (*x*) distance:

$$E_o = \frac{1}{2} kx^2 \quad (6)$$

The expected velocity at impact (v_{imp}) was calculated from the kinetic energy at impact ($E_{k,imp}$) and moving mass (*m*):

$$E_{k,imp} = \frac{1}{2} m {v_{imp}}^2 \quad (7)$$

$$v_{imp} = \sqrt{\frac{2E_{k,imp}}{m}} \qquad (8)$$

Table 5. Design of experiment to assess the impact of MN tip outer diameter on the insertion of a single microneedle with a 60, 100, and 120 µm tip OD (*m*=6 g).

Microneedle tip OD (µm)	Insertion	Spring Compression, *x* (mm)	Energy of the system, E_o (mJ)	Expected velocity at impact, v_{imp} (m s^{-1})	Trials per device (n)
60, 100, 120	Quasi-static	N/A	0	0	4
	Dynamic (*k*=266 N m^{-1})	12	19.2	2.5	4
		20	53.2	4.2	4

4.1.5.2. Effect of Momentum on Microneedle Insertion

The impact of the momentum on the force and energy required for successful MN insertion was assessed at constant total energy (E_o=1.2 mJ), using the design of experiment in Table 6.

Table 6 Design of experiment to assess the impact of momentum on the insertion of a single microneedle with a 100 µm tip OD (*k*=266 N m^{-1}; *x*=4 mm).

Energy of the system, E_o (mJ)	Moving mass, *m* (g)	Expected velocity at impact, v_{imp} (m s^{-1})	Expected momentum at impact, p_{imp} (kg m s^{-1})	Trials per device (n)
1.2	6	0.64	0.004	4
	21	0.34	0.007	4
	36	0.26	0.009	4

4.1.5.3. Effect of Microneedle Tip Outer Diameter on Insertion

The impact of MN tip OD on insertion dynamics was assessed using 1-MN devices with 3 different tip ODs: 60 µm, 100 µm, and 120 µm. Each 1-MN device was inserted into the skin model using

the quasi-static insertion test and spring 111 at 12 mm and 20 mm spring compression levels, per Table 5.

4.1.5.4. Effect of the Microneedle Array Size on the Insertion

The effect of the number of MNs on the MN insertion dynamics was assessed using 1-MN, 6-MN and 19-MN devices. Each device was inserted into the skin model using spring 111 at 12 mm and 20 mm spring compression levels, per Table 7. The single MN was also assessed using quasi-static insertion tests.

Table 7. Design of experiment to assess the impact of array size on MN insertion with single (1-MN), six (6-MN), and nineteen (19-MN) microneedle arrays consisting of projections with 100 µm tip OD (k=266 N m^{-1}).

Microneedle array size	Spring Compression, x (mm)	Energy of the system, E_o (mJ)	Expected velocity at impact, v_{imp} (m s^{-1})	Trials per device (n)
1, 6, 19	12	19.2	2.5	4
	20	53.2	4.2	4

4.2. Results and Discussion

4.2.1. Microneedle Insertion Profile

The force versus displacement curves were generated for each MN insertion until maximum force and displacement values were reached. The maximum force (ranged between ~8-17 N) recorded for each insertion resulted from the maximum displacement (~0.7 mm) of the MN into the skin, which corresponded to the height of the MN. An example of a MN insertion force versus displacement curve is provided in Figure 24. Since the force sensor was located directly under the skin model sample, the first response from the force sensor only appeared at the initial point of impact of the MN on the skin model. As observed previously [70] the force drops slightly as the

needle breaks the SC. The data acquisition rate is not sufficiently high to measure this drop in force due to the high velocity of the needle, and the force-displacement graph only shows a temporary change in slope.

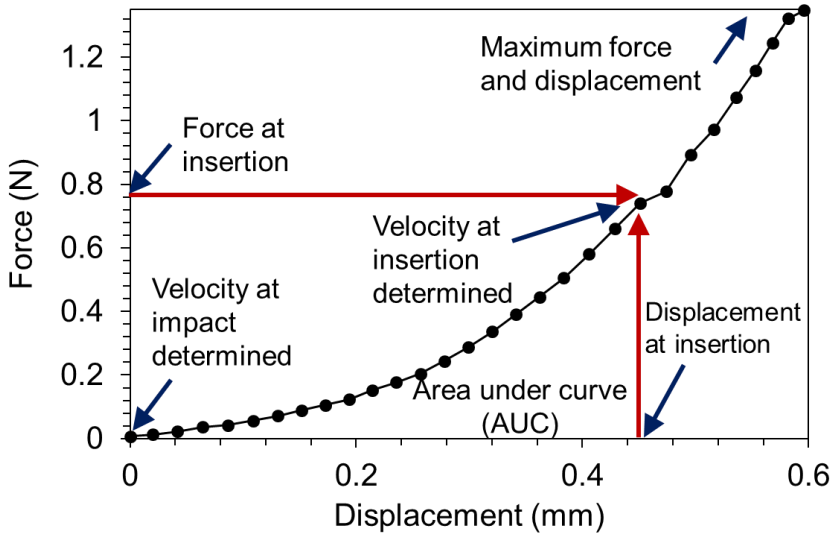

Figure 24. Microneedle insertion force versus displacement profile generated from an experiment using spring #30 (k=152 N m^{-1}, x=4 mm, E_o=1.2 mJ, and estimated v_{imp}=0.6 m s^{-1}) collected from the high-speed camera (at 10 kfps) and the FS01 force sensor (at 100 kHz).

From each MN insertion experiment, the following main independent variable defined was E_o, tip OD, and number of MNs in an array. The velocity at impact v_{imp}, the velocity at insertion v_{ins}, the momentum at impact $p_{imp}=m \cdot v_{imp}$ with the moving mass m, the momentum at insertion $p_{ins}=m \cdot v_{ins}$, the kinetic energy at impact $E_{k,imp}$ and the kinetic energy at insertion $E_{k,ins}$ were determined as covariates or predictors. From each MN insertion, the main dependent variables were the force of insertion F_{ins}, the energy required for insertion E_{ins} corresponding to the area under the force-displacement curve until the point of insertion, and the displacement at insertion D_{ins}, as previously shown in chapters 2 and 3.

4.2.2. Factors Affecting the Dynamic Insertion of a Single Microneedle

MN insertions were conducted using a single MN consisting of a 120 µm tip OD to determine if the process of rupturing the SC was a dynamic process. The impact of E_o and v_{imp} on F_{ins} and E_{ins} was evaluated. A decrease in the F_{ins} was observed as a function of v_{imp}, p_{imp}, and $E_{k,imp}$, which were manipulated by changing the E_o of the spring-loaded applicator. The mean percent difference between the estimated v_{imp} and measured v_{imp} across 84 measurements was calculated to be 1.1% ± 0.25%, according to:

$$\% \text{ Difference in } v_{imp} = \left(\frac{\text{estimated } v_{imp} - \text{measured } v_{imp}}{\text{estimated } v_{imp}}\right) \text{x } 100 \qquad (9)$$

The F_{ins} decreased from 0.66 N to 0.12 N as v_{imp} increased from 0 to 4.2 m s^{-1}. The main variable in p_{imp} and $E_{k,imp}$ was v_{imp}, since the mass of the moving object was kept constant at 6 g in the design of experiment in Table 5. Therefore, v_{imp} of the MN on the skin model was identified as the driving factor influencing the F_{ins} (Figure 25A). This decrease in the F_{ins} as v_{imp} increased confirmed the dynamic nature of the MN insertion, which agreed with the observations by Heverly et al., who showed that F_{ins} of hypodermic needles into tissue also decreased with increasing v_{imp} up to a critical value. Heaverly et al. further showed that above the critical v_{imp}, the F_{ins} became independent of the v_{imp} [142]. Similarly to F_{ins}, the E_{ins} also decreased from 0.04 mJ to 0.01 mJ as v_{imp} increased from 0 to 4.2 m s^{-1} (Figure 25B). The impact of E_o and v_{imp} on F_{ins} and E_{ins} was also confirmed in single MNs with 60 µm and 100 µm tip OD data not shown).

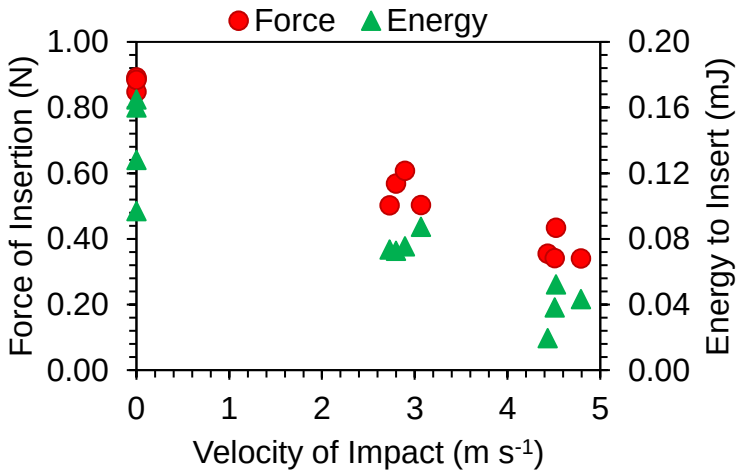

Figure 25. Factors influencing the insertion of a single microneedle into skin. Force and energy required to insert a single microneedle of outer tip diameters of 120 µm (n=12), into the artificial skin model, as a function of the microneedle's velocity at impact against the skin.

A possible reason for decreasing F_{ins} and E_{ins} as a function of v_{imp} was the development of a critical strain concentration in the SC of the skin model around the MN tip earlier to cause rupture during dynamic insertion, compared to quasi-static insertion. During quasi-static insertion of a MN, the stress was distributed across a larger region of the skin (up to a radius >1.5 mm from the MN tip), and the displacement of the MN into the skin to reach the critical strain to cause SC failure was significantly higher. However, since skin is a viscoelastic material whose mechanical responses are strain-rate dependent, the findings presented in Figure 25 were contradictory to the theory of viscoelasticity – at high v_{imp}, a higher strain-rate of the skin would have yielded a larger F_{ins} and E_{ins}. Therefore, along with reaching the UTS of the skin faster, it was observed that increasing v_{imp} would lead to changing the mode of fracture of the SC from mode-II fracture (typical for blunt-tipped structures and observed during quasi-static insertions) to mode-I fracture (typical for sharp-tipped structures). Since the fracture toughness of skin to mode-I fracture is significantly lower

than mode-II fracture, a significant decrease in the F_{ins} and E_{ins} was observed during dynamic insertions.

4.2.3. Influence of Momentum

The influence of p_{imp} on MN insertion was assessed by using a constant E_o at 1.2 mJ, and increasing *m* from 6 g to 36 g to reduce of v_{imp} from 0.64 m s^{-1} to 0.26 m s^{-1}, respectively. This resulted in a p_{imp} range from 0.004-0.009 kg m s^{-1}. During this increase in p_{imp}, F_{ins} increased from 0.49 N to 0.74 N (P=0.006) and E_{ins} increased from 0.07 mJ to 0.09 mJ (P=0.45), but no significant influence of p_{imp} on the MN insertion were observed (Figure 26). This suggested that MN insertions were more influenced by changing E_o of the system than by changing the momentum of the moving MN. Further investigations into the role of p_{imp} at higher E_o will be helpful to confirm the differences in the effects between v_{imp} and p_{imp} on MN insertion.

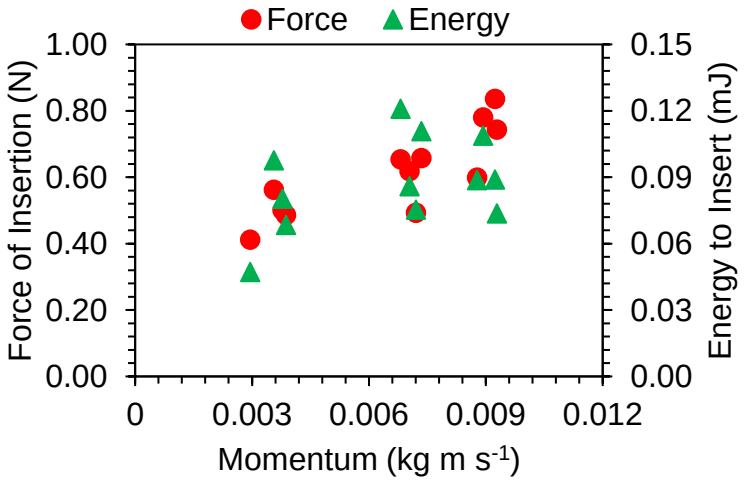

Figure 26 Impact of momentum on the insertion of a single microneedle into skin. Force and energy required to insert a single microneedle of 100 µm outer tip diameter into the artificial skin model were determined (n=12) at a constant total energy of 1.2 mJ. The momentum was altered by changing the moving mass *m* of the microneedle.

4.2.4. Influence of Microneedle Geometry

The effect of MN tip area on the F_{ins} and E_{ins} was assessed using three MN tip areas: $2.83x10^{-9}$ m^2 (60 µm tip OD), $7.85x10^{-9}$ m^2 (100 µm tip OD), and $1.13x10^{-8}$ m^2 (120 µm tip OD). Each MN tip area was tested at three levels of total energy (E_o=0 mJ, 20 mJ, and 53 mJ; n=4 per test condition) using a 3x3 factorial design. The mean F_{ins} and E_{ins} from the MN insertions are provided in Table 8, which shows a significant increase in the F_{ins} and E_{ins} as the MN tip area increased ($P<0.001$). Table 16 provides the ANOVA results for this factorial design (see Appendix C in page 171). Due to the increased area of the MN tip acting on the skin, a larger force needed to be applied to the skin to rupture through the SC. Increasing the E_o, which also increased the v_{imp}, decreased the F_{ins} and E_{ins} significantly ($P<0.001$) for all tip areas (Figure 27A and B). For example, during quasi-static insertion (E_o=0 mJ), increasing the tip area from $2.89x10^{-9}$ m^2 to $1.13x10^{-8}$ m^2 led to a significant increase in F_{ins} from 0.23 N to 0.88 N, respectively; however, dynamic insertions (E_o=53 mJ) caused a relatively reduced effect on the F_{ins} from 0.11 N to 0.37 N, respectively. Since the energy required per unit area of the MN tip to cause a crack was determined by the slope of the linear best fit in Figure 27B, it provided an indirect indication of the fracture toughness of skin; the slope in Figure 27B decreased from 10.1 J m^{-2} to 2.8 J m^{-2} as E_o increased from 0-53 mJ. This suggested that all MNs tested could rupture the SC at lower F_{ins} and E_{ins} as the energy introduced to the system increased, thereby reducing the deformation of the skin prior to rupture. This finding has a significant implication to the development of MN insertion protocols, since the introduction of E_o to the MN system will allow drastic reduction in the effort required to penetrate the SC of the skin for repeatable insertions for all MN tip areas.

Table 8. Effect of energy of the system (E_o) and the microneedle tip area on the force and energy required to insert a single microneedle into skin. The least significant difference (LSD, P=0.05) is provided at a 95% confidence interval (significantly different means are indicated by superscripted a, b, c, and d next to the mean value).

Force of insertion, F_{ins} (N)						
Energy, E_o (mJ)	Microneedle tip area (m^2)					
	$2.83x10^{-9}$		$7.85x10^{-9}$		$1.13x10^{-8}$	
	Mean	SD	Mean	SD	Mean	SD
0	0.230	0.089	0.655	0.064	0.878^{b}	0.018
20	0.182	0.045	0.375	0.036	0.545	0.054
53	0.112^{a}	0.025	0.117^{a}	0.041	0.367	0.043
LSD (P=0.05)	0.730					
MSE	0.003					
Error df	27					
n	4 each					
CV%	13.07					
Energy to insert, E_{ins} (mJ)						
Energy, E_o (mJ)	Microneedle tip area (m^2)					
	$2.83x10^{-9}$		$7.85x10^{-9}$		$1.13x10^{-8}$	
	Mean	SD	Mean	SD	Mean	SD
0	0.036^{a}	0.016	0.043^{a}	0.013	0.138^{c}	0.032
20	0.018^{a}	0.011	0.046^{a}	0.032	0.077^{d}	0.007
53	0.011^{ab}	0.004	0.010^{ab}	0.007	0.038^{a}	0.014
LSD (P=0.05)	0.026					
MSE	0.000					
Error df	18					
n	4 each					
CV%	38.57					

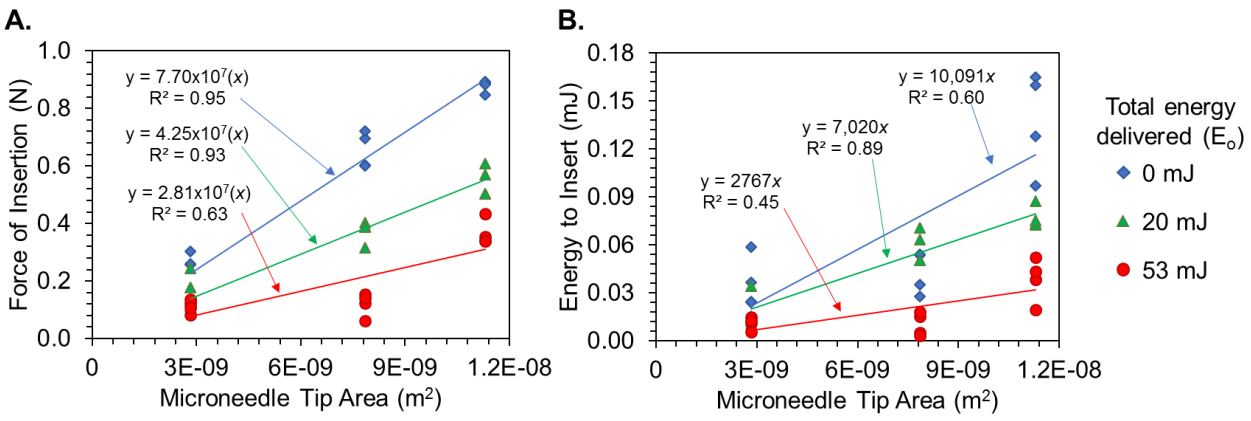

Figure 27. Impact of microneedle tip area on skin insertion. (A) Force and (E) energy required to insert a single microneedle as a function of the microneedle tip area at three levels of total energy delivered (E_o=0, 20, and 53 mJ).

4.2.5. Dynamic Insertion of Microneedle Arrays

The effect of the number of MN projections in an array, with projections separated by 1 mm distance, on insertion dynamics (i.e., F_{ins} and E_{ins}) was assessed using three MN array configurations: 1-MN, 6-MN, and 19-MN (Figure 28A). MN array insertions were assessed at E_o=20 mJ and 53 mJ, using a 3x2 factorial design. Table 9 presents the mean F_{ins} and E_{ins} values recorded during the MN insertion tests, while the ANOVA results can be found in Table 17 (see Appendix C on page 171).

For each MN configuration, increasing E_o from 20 mJ to 53 mJ led to a significant reduction in F_{ins} and E_{ins} ($P<0.001$), as discussed earlier for single MN insertions. As the number of MNs increased from 1 to 19, the mean F_{ins} increased linearly from 0.38 N to 11.29 N (E_o=20 mJ) and 0.12 N to 7.83 N (E_o=53 mJ). Similarly, the mean E_{ins} increased linearly from 0.05 mJ to 2.32 mJ (E_o=20 mJ) and 0.01 N to 6.69 mJ (E_o=53 mJ). This can be further visualized in Figure 28B and

C, and suggested that MNs in arrays separated by 1 mm acted independently of each other and that the radius of deformation surrounding each MN was less than 0.5 mm during dynamic conditions. As a result, a significant interaction between the MN array size and the E_o was observed in Table 9 for F_{ins} and E_{ins}, demonstrating their synergistic effect on successful rupturing of the SC layer.

Table 9. Effect of energy of the system (E_o) and the number of microneedles in an array on the force and energy required to insert a single microneedle into skin. The least significant difference (LSD, P=0.05) is provided at a 95% confidence interval (significantly different means are indicated by superscripted a, b, c, d, and e next to the mean value).

Force of insertion, F_{ins} (N)						
Energy, E_o (mJ)	Number of microneedles					
	1		6		19	
	Mean	SD	Mean	SD	Mean	SD
20	0.375^a	0.037	5.703^b	0.789	11.293^d	0.529
53	0.118^a	0.040	2.080^c	0.293	7.833^e	0.855
LSD (P=0.05)	0.796					
MSE	0.287					
Error df	18					
n	4 each					
Energy to insert, E_{ins} (mJ)						
Energy, E_o (mJ)	Number of microneedles					
	1		6		19	
	Mean	SD	Mean	SD	Mean	SD
20	0.046^a	0.032	1.080^b	0.485	2.320^c	0.189
53	0.010^a	0.007	0.215^a	0.033	0.688^d	0.167
LSD (P=0.05)	0.332					
MSE	5.0×10^{-5}					
Error df	18					
n	4 each					

In contrast, skin deformation surrounding a MN during quasi-static insertion tests provided visual confirmation that the radius of the deformed area increased up to 1.5 mm with MN displacement (up to 700 µm). It is therefore probable that MNs separated by only 1 mm would be acting independently during dynamic insertions, but not during quasi-static MN insertion. It is also possible that the correlation between the F_{ins} or E_{ins} and the number of MNs will deviate from linearity beyond a certain threshold number of projections per array during quasi-static insertions. Therefore, developing MN insertion protocols using dynamic conditions appeared to be more favorable in ensuring successful insertion of MN arrays, compared to quasi-static insertions. Further investigation into the nature of MN interactions in an array during MN insertion will be beneficial.

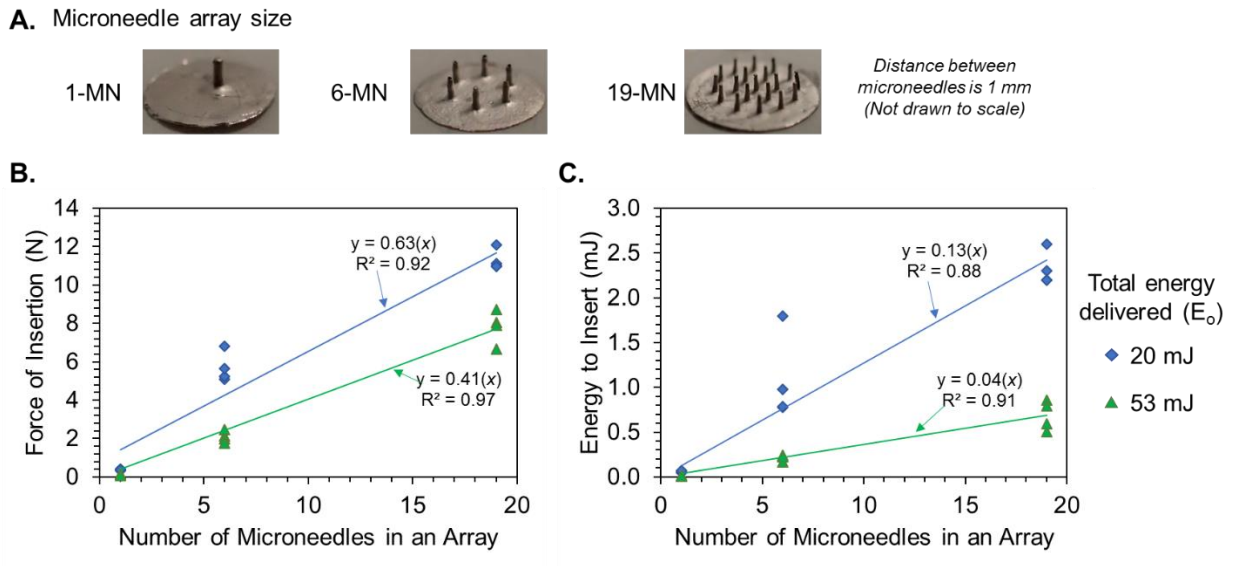

Figure 28. Impact of the number of microneedles in an array on skin insertion. (A) Microneedle array sizes used in the study consisted of 1 (1-MN), 6 (6-MN), and 19 (19-MN) projections with 100 µm tip outer diameter. CB) Force and (C) energy required to insert microneedle arrays as a function of the number of microneedle projections in an array, measured at two levels of total energy delivered (20 and 53 mJ).

4.3. Conclusions

Using an artificial skin model that was previously validated for mechanical similarity to human skin, the dynamics of MN insertions have been characterized. Using extremely high rates of data acquisition, this study provided insight on key factors that significantly influenced successful MN insertions passed the skin's SC layer, including E_o, v_{imp}, MN tip area, and the number of projections. By increasing E_o, the v_{imp} of the MN device increased, which helped to significantly decrease the force and energy required to insert the MN device into the skin. Reducing the tip area of the MN led to the reduction in force and energy to insert the MNs. Increasing the number of microneedles in an array led to a linear increase with the number of needles in force and energy to insert the MNs during dynamic insertions. The understanding of these mechanical relationships will facilitate the development MN devices and insertion protocols to increase the success of intradermal drug delivery and biosensing approaches.

5. PRECISE MEASUREMENT OF INTRADERMAL FLUID DELIVERY

Accurately quantifying the volume of fluid that can be delivered to the skin is a challenging task due to skin's thin and opaque nature, high resistance to flow, fluid backflow, and large spread of the bolus liquid deposition in the dermis. Typically, ID devices are assessed during skin injections for dose accuracy and fluid wastage using gravimetric analyses, which do not provide sufficient resolution and accuracy to capture fluid delivered to the skin and fluid back-flowed due to the skin's high resistance to flow. The objectives of this chapter are to develop a high-resolution ID fluid delivery characterization technique using a $^{99m}TcO_4^-$ radiotracer, and to determine the fluid delivery potential into the skin with several ID delivery devices.[4] The proposed characterization method is tested in *ex vivo* and *in vivo* models.

5.1. Materials and Methods

5.1.1. Materials

A number of methods and devices were assessed for their ID fluid delivery capacity: the Mantoux technique using a 31-gauge needle (31G; BD Ultra-Fine™ short pen needle; 31-gauge, 8 mm; product no. 320109, Becton, Dickinson and Company, Franklin Lakes, NJ, USA), a 26-gauge ID bevel needle (26G; BD Precision-Glide™ needle; 26-gauge, 9.53 mm; product no. 305110; Becton, Dickinson and Company, Franklin Lakes, NJ, USA); and a single hollow metallic MN (ML1; 700 µm height, 100 µm tip diameter) and a 3×2 hollow metallic MN array (ML6; 700 µm

[4] A version of chapter 5 has been prepared for publication:

Ranamukhaarachchi S.A., Esposito T.V., Raeiszadeh M., Stoeber B., Häfeli U.O. Precise measurement of intradermal fluid delivery using a low activity technetium-99m pertechnetate tracer.

height, 100 µm tip diameter, 1 mm distance between MNs in an array) devices mounted to a custom female Luer adapter. The ML1 and ML6 devices were fabricated according to Mansoor et al. [16] and inserted perpendicular to the skin using the spring-loaded applicator shown in Figure 22 and Figure 23 in chapter 4 .

The radioisotope technetium-99m pertechnetate ($^{99m}TcO_4^-$) with a half-life of 6 h was used to evaluate the ID fluid delivery performance of aforementioned methods/devices. The $^{99m}TcO_4^-$ was obtained from the Vancouver General Hospital and diluted in 9 mg mL^{-1} sodium chloride (Hospira, Lake Forest, IL, USA) to 740 kBq mL^{-1} using a CRC-55tR dose calibrator (Capintec, Florham Park, NJ, USA). This diluted solution is hereforth referred to as the $^{99m}TcO_4^-$ solution. During *in vivo* injections, a green tattoo ink (Millennium Colorworks Inc., New York, NY, USA) was incorporated into the $^{99m}TcO_4^-$ solution to aid in identification of the injection site. The devices to be tested were attached via a Luer connector to a 1 mL BD syringe (product no. 309628, Becton, Dickinson and Company, Franklin Lakes, NJ, USA) containing 0.2-0.4 mL of the $^{99m}TcO_4^-$ solution and primed before injection.

5.1.2. Ex Vivo Skin Injections

Freshly excised skin from the abdomen of female miniature Yucatan pigs weighing 20-30 kg (Sinclair Bio-resources, Columbia, MO, USA) was immediately frozen at -80ºC for 48 h, and thawed for 1 h before testing. Porcine skin samples were prepared as described in Section 2.2.1.

Injection of 0.1 mL $^{99m}TcO_4^-$ solution was performed using the ID delivery devices in 4-6 porcine skin samples per device to assess the fluid delivery efficiency (Figure 29A**)**. As a control, 0.1 mL of the $^{99m}TcO_4^-$ solution was applied topically to the skin using a 20-200 µL micropipette

(PIPETTEMAN Classic™, product no. F123601; Gilson Inc., Middleton, WI, USA). Prior to injection or topical fluid application, the weight of the needle-syringe injection device or the pipette was measured on a B120S balance (Sartorius GmbH, Göttingen, Germany). The 31G and 26G needles (according to the Mantoux method [143]) and MN devices were inserted into the skin by a person trained in these injections, followed by manual delivery of 0.1 mL $^{99m}TcO_4^-$ solution in under 10 s. The ML6 device was also assessed for delivery of a larger volume of $^{99m}TcO_4^-$ solution (0.3 mL $^{99m}TcO_4^-$ solution under 30 s) to determine the performance differences as the fluid delivery target increased.

Post-administration, the needle-syringe injection devices were removed from the skin and weighed to determine the net mass released. The net mass was converted to net volume released using the density of normal saline (ρ_{saline}=1.005 mg μL^{-1}). This gravimetric measurement was compared to the total radioactivity released from the syringe for validation of the method. The skin surface was wiped using a series of cotton swabs, as illustrated in Figure 29B, to collect and capture any $^{99m}TcO_4^-$ solution that back-flowed to the surface of the skin during or after the injection. Since $^{99m}TcO_4^-$ is water- and ethanol-soluble, the initial dry swab was followed by a swab dipped in water, a swab dipped in 70 vol% ethanol, and a second dry swab to ensure that no radiotracer was present on the surface of the skin. Another swab was used to collect the $^{99m}TcO_4^-$ remaining on the surface of the needle device. All swabs were transferred to plastic test tubes for measurement in an automatic gamma counter (2470 WIZARD^2, Perkin Elmer, Waltham, MA, USA) as shown in Figure 29C. The skin sample was unmounted from its support structure and transferred to a plastic test tube for measurement in the gamma counter, as well.

5.1.3. In Vivo Skin Injections

ID injections were performed on Sprague Dawley rats (Charles River Laboratories, Sherbrooke, QC, Canada) under general anesthesia, using the ML1 single MN device with a spring-loaded applicator at the Center for Comparative Medicine at the University of British Columbia. Sprague Dawley rats have a similar skin thickness to humans. The experiments were conducted under the approved protocol A12-0172 by the University of British Columbia's Animal Care Committee. The skin on the dorsal surface of the rat was shaved and then treated with a depilatory cream (Nair; Church & Dwight Co. Inc., Trenton, NJ, USA). The dorsal skin was stretched over a plastic vial cap to provide a rigid support to facilitate the MN insertion. The ML1 device was connected to a BD 1 mL syringe containing the $^{99m}TcO_4^-$ solution mixed with green tattoo ink, and 0.1 mL of $^{99m}TcO_4^-$ solution was injected manually in under 10 s at three separate sites on the rat. Similarly, 0.3 mL of $^{99m}TcO_4^-$ solution was injected manually in under 30 s at three separate sites on the rat, as well. Backflow on the surface of the skin and ML1 device were removed using swabs as described for the *ex vivo* experiments. All fluid injection sites were outlined using a permanent marker, photographed, and removed by deep excision to the fascia. The excised injection sites and backflow swabs were placed in plastic test tubes and measured in the gamma counter as described above.

5.1.4. Measurement and Data Analysis

All test tubes were placed in the gamma counter and measured for 30 seconds in triplicate. The readout from the gamma counter in cpm was converted to SI units (kBq) using a calibration factor (51,600 cpm per kBq). Radioactivity from the skin (A_{Skin}) provided a precise measurement of all fluid that successfully entered the skin, while radioactivity from the cotton swabs ($A_{Backflow}$, test

tubes 1-5 in Figure 29C) provided a measurement of all fluid that back-flowed out of the skin. The summation of radioactivity measurements (A_{Total}) from all test tubes in Figure 29C captured all fluid released from the syringe, which was also confirmed by gravimetric measurement to determine the total volume released (V_{Total}, µL). Summation of the total radioactivity measured in kBq provided direct and precise measurements of volume successfully delivered to the skin (equation 9) and volume back-flowed (equation 10).

$$V_{Skin} = \left(\frac{A_{Skin}}{A_{Total}}\right) \times V_{Total} \quad (9)$$

$$V_{Backflow} = \left(\frac{A_{Backflow}}{A_{Total}}\right) \times V_{Total} \quad (10)$$

The volume delivered to the skin as a percentage of total volume released from the syringe (equation 11) and the relative volume back-flowed (equation 12) were calculated of each ID delivery device to compare the delivery efficiencies:

$$\%\, V_{Skin} = \left(\frac{V_{Skin}}{V_{Total}}\right) \times 100 \quad (11)$$

$$\%\, V_{Backflow} = \left(\frac{V_{Backflow}}{V_{Total}}\right) \times 100 \quad (12)$$

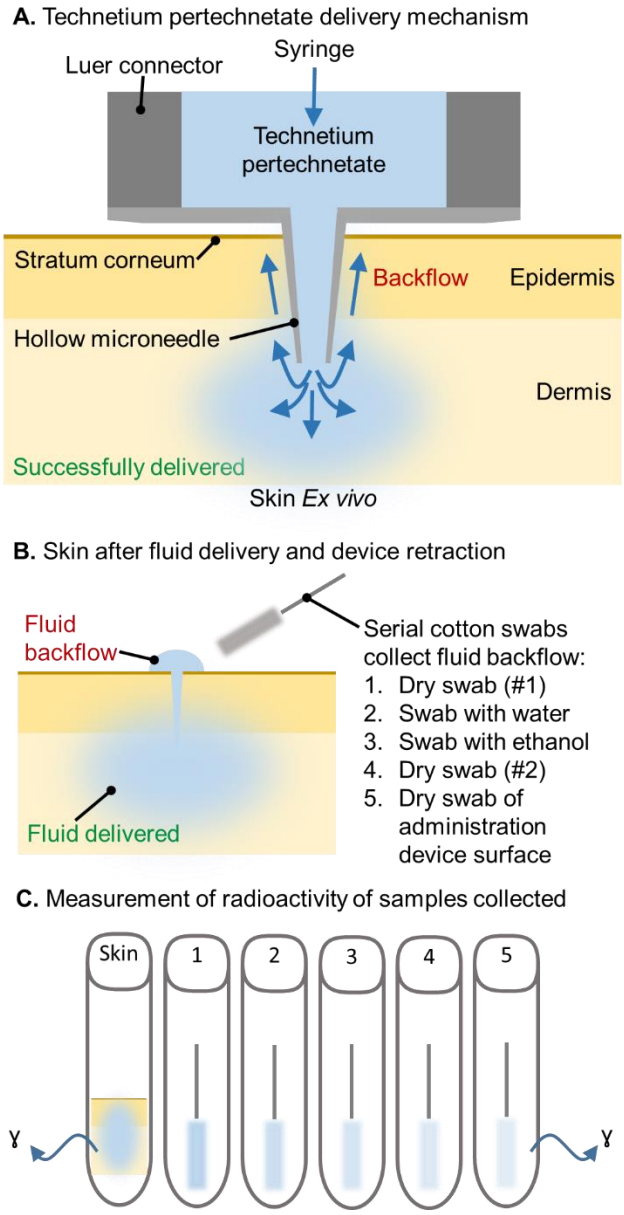

Figure 29. Fluid delivery and measurement methodology. (A) A highly dilute $^{99m}TcO_4^-$ solution is administered using ID delivery devices. (B) Fluid backflow to the skin surface post-administration is captured by cotton swabs. (C) Gamma radiation present in skin and cotton swabs is measured using a gamma counter.

5.3. Results and Discussion

5.3.1. Device Performance Ex Vivo

The injection performance of the ID delivery devices and topical control for the *ex vivo* tests are presented in Figure 30 and in more detail in Table 10. The ML6 MN device yielded the highest fluid delivery efficiency with 92.9 ± 6.0% of the total fluid released from the syringe reservoir, followed by the 31G needle at 88.6 ± 9.5%. The lowest delivery efficiency was reported by the 26G needle at 68.7 ± 1.7%, which was significantly different from the ML6 ($P<0.001$) and 31G ($P<0.002$) devices at a 95% confidence interval. This lack of delivery efficiency by the 26G needle, which is the conventionally used ID delivery device in clinical settings, may be attributed to the larger fluid backflow path that is created during the insertion and retraction of the needle to and from the skin, allowing fluid to flow back out of the skin more easily to relieve the pressure built up inside the dermis; and the small number of repetitions performed in this study. The control, where a 0.1 mL droplet of the $^{99m}TcO_4^-$ solution was topically applied to the skin surface, showed that only 1.1 ± 0.4% of fluid was left on or adhered to the skin surface. The ability to remove 98.9% of the fluid from the skin surface using the swabbing technique described in Figure 29B showed that the remaining $^{99m}TcO_4^-$ adhering to the skin surface was negligible compared to the volume in the skin or volume removed by swabs.

It was suspected that delivery of fluid deeper into the reticular dermis with conventional hypodermic needles due to their higher length may allow more accurate volume injections with less fluid backflow, compared to shallower injections into the papillary dermis with MNs. This was predominantly due to the ability of the reticular dermis to accommodate and expand with the incoming fluid in its hydrogel-like, elastic structure better compared to the upper papillary dermis

[144]. However, shallower intradermal injections using the ML6 device yielding more accurate dermal injections with less fluid backflow refuted that hypothesis.

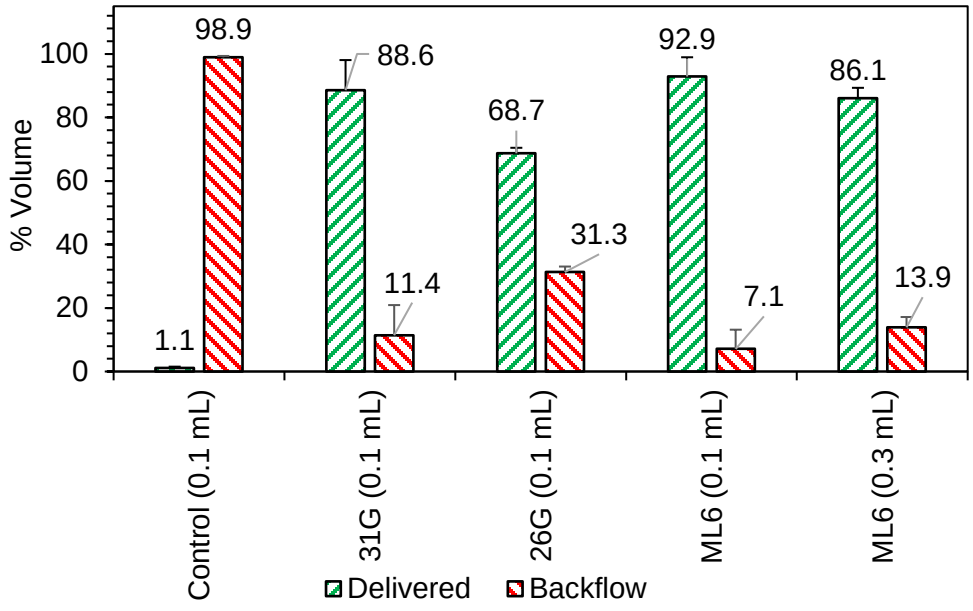

Figure 30. Comparison of ID fluid delivery methods ex vivo for successful fluid delivery and fluid backflow resulting in wastage (n=5 for the control, 31G needle, and 26G needle for 0.1 mL injections; n=6 for 0.1 mL injections using ML6; n=4 for 0.3 mL injections using ML6; error bars represent standard deviation).

A higher target fluid delivery volume of 0.3 mL was tested in excised porcine skin with the ML6 device, resulting in a decrease in the delivery efficiency from 92.9% to 86.1% compared to delivery of 0.1 mL, and an increase in the fluid backflow from 7.1% to 13.9%. The decrease in the fluid delivery efficiency arose due to limitations in the fluid absorption by the dermal layer of the skin and the skin's capability to seal off the injection site against the high pressure built up underneath the skin [106]. It was likely that the excised skin had undergone mechanical and structural changes, since it was previously frozen [70, 145], which may have affected the fluid delivery efficiency as larger delivery volumes were injected. Injections *in vivo* into live skin may improve the delivery

efficiency due to increased elasticity of skin layers, as described in chapter 2. Nonetheless, the volume delivery efficiency with the ML6 device suggested that *ex vivo* porcine skin was able to accommodate 0.3 mL volumes of fluid with dosing accuracies that comply with ISO 11608-1:2000 standard that requires at least 80% fluid delivery efficiency [126].

5.3.2. Device Performance In Vivo

The *in vivo* injection performance of the ML1 device was assessed in a Sprague Dawley rat with the $^{99m}TcO_4^-$ solution to determine the fluid delivery efficiency (Figure 31) with 0.1 mL and 0.3 mL injection volumes. The green tattoo ink mixed into the $^{99m}TcO_4^-$ solution clearly helped to visualize the injection site and the bleb formation. Quantification of the amount of radioactivity in the injection sites post-excision showed a 92.5% fluid delivery efficiency and a 7.5% backflow for 0.1 mL volume. An improvement between *ex vivo* injections in porcine skin and *in vivo* injections in rat skin was not seen for 0.1 mL injections. However, injections of 0.3 mL *in vivo* yielded an improved delivery efficiency of 94.4% and backflow of 5.6%, compared to *ex vivo* porcine skin injections. This improvement was possibly attributed in part to the mechanical properties of *in vivo* rat skin that allowed the skin to expand during fluid delivery more easily, possibly due to higher elasticity. The other reason for the improved fluid delivery efficiency was likely the use of a single hollow MN projection *in vivo*, compared to six projections *ex vivo*. When six projections were used *ex vivo*, six micro-pores were created on the skin, which likely provided more paths for fluid backflow to the surface. Whereas, fluid could only backflow through one micro-pore during injection using a single MN, thereby potentially maximizing the fluid delivery efficiency. The effect of MN array size on the fluid delivery efficiency and backflow will need to be characterized in future studies.

5.3.3. Comparison of Methodologies

The performance of this $^{99m}TcO_4^-$ injection methodology was significantly superior compared to the conventional gravimetric measurements in many aspects. The sensitivity of the measurement was determined to be 39,441 cpm kBq^{-1} from the slope of the $^{99m}TcO_4^-$ calibration curve in the gamma counter. The background within the energy window for ^{99m}Tc (140 ± 28 keV) on the gamma counter that was used for measurements was 0.9 ± 0.2 Bq (35.9 ± 8.3 cpm), and detection resolution, calculated as ten times the standard deviation of the background, was 2 Bq (83 cpm). During this study, radioactivity per volume of fluid injected ranged between 0.33-1.30 kBq μL^{-1}; and thus, the volume detection resolution was determined to be between 1.61-6.41 nL, where the higher radioactivity per volume corresponded to the smaller resolution value. Therefore, the use of the proposed volume determination method allowed quantifying the fluid volumes at a significantly higher resolution than the gravimetric method, since the resolution of the gravimetric method is 0.1 µL.

During gravimetric measurements, the weight of the syringe and connected device is measured during each step of the process, as described previously. Many challenges of the gravimetric method, including lower measurement sensitivity, potential errors caused by fluid evaporation prior to measurement, and the inability to accurately capture fluid backflow have been addressed by the proposed method of evaluating fluid delivery using $^{99m}TcO_4^-$ solution. Accurate quantification of fluid backflow has not been addressed to date, due to the difficulty of collecting only the fluid back-flowed, and not any other liquids present on the skin surface, such as sweat, oil and interstitial fluid [125]. With the $^{99m}TcO_4^-$ method, the presence of interfering substances did not affect the fluid backflow measurements by the gamma counter.

The total volume released from the syringe during each injection was evaluated by radioactivity (summation of all collected radioactivity using the swabbing technique) and gravimetric measurement of the syringe before and after injection. The two methods were comparable and consistent in evaluating the total volume released from the syringe, with less than ± 1% difference between the two methods (Table 10).

The proposed methodology of injecting extremely low activities of $^{99m}TcO_4^-$ solution into the skin could be potentially used in clinical settings for dose accuracy determinations of ID and other delivery devices without posing a significant safety risk to the patients. The radiation dose levels employed in this study would already be significantly lower than occupational limits recommended by the International Commission on Radiological Protection (ICRP), Federal Aviation Administration (FAA), and the National Council on Radiation Protection and Measurements (NCRP). Using dosimetric OLINDA/EXM code estimates, an injection of the highest $^{99m}TcO_4^-$ activity concentrations used in this study (6.29 MBq mL^{-1}) and the highest volume injected (300 µL) would give a full body radiation dose of 8.15 µSv if the assumption that the radioactivity is distributed equally throughout the system and is not eliminated until complete decay is made (worst case scenario) [146]. This radiation dose is exactly one tenth of the dose that a flight passenger receives from the cosmic radiation during a transatlantic flight at 10,000 m [147]. However, given the extremely high sensitivity and low limit of detection of this methodology for quantifying fluid delivery into skin, the total activity used in a measurement can be significantly reduced, while still achieving far superior measurements compared to the gravimetric method.

Table 10. Comparison of volume delivery efficiency of intradermal delivery devices. Each injection into *ex vivo* porcine skin using the topical control, 30G needle, 26G needle, and the ML6 device was captured by radioactivity measurements (cpm and kBq units) of fluid delivered to the skin and fluid backflow. The mass released by the syringe was gravimetrically measured as a comparison to the radioactivity measurements. Activity per volume (kBq µL^{-1}) was measured before each $^{99m}TcO_4^-$ injection.

ID Delivery Method	N	Skin	Volume released from syringe		Radioactivity Measurements					Volume Delivered		% Difference	% Volume		% Volume Delivered	% Volume Backflow
			Intended volume (µL)	Gravimetric Measure (mg)	Skin (cpm)	Backflow (cpm)	Skin (kBq)	Backflow (kBq)	Activity per Volume (kBq µL^{-1})	Skin (µL)	Backflow (µL)	Radioactive volume vs. gravimetric	Skin	Backflow	Mean ± SD	Mean ± SD
Topical application (pipette)	1	Porcine, ex vivo	100	102.7	4814	523343	0.94	102.62	1.02	0.93	101.07	-0.7%	0.91	99.09	1.1 ± 0.4	98.9 ± 0.4
	2			99.1	3002	500257	0.59	98.09	1.00	0.59	98.41	-0.1%	0.60	99.40		
	3			101.1	4401	514644	0.86	100.91	1.01	0.86	100.14	-0.1%	0.85	99.15		
	4			90.3	9693	588164	1.90	115.33	1.30	1.46	88.54	-0.3%	1.62	98.38		
	5			98.8	7024	468810	1.38	91.92	0.95	1.45	96.55	-0.8%	1.48	98.52		
30G ID Mantoux	1	Porcine, ex vivo	100	100.6	433547	16853	85.01	3.30	0.87	97.22	3.78	0.4%	96.26	3.74	88.6 ± 9.5	11.4 ± 9.5
	2			78.4	421012	47738	82.55	9.36	1.18	70.06	7.94	-0.5%	89.82	10.18		
	3			93.6	418965	119438	82.15	23.42	1.14	72.37	20.63	-0.6%	77.82	22.18		
	4			104.9	196318	1950	38.49	0.38	0.37	102.98	1.02	-0.9%	99.02	0.98		
	5			99.2	142448	35737	27.93	7.01	0.35	78.82	19.78	-0.6%	79.94	20.06		
26G ID Mantoux	1	Porcine, ex vivo	100	123.4	2183470	1142683	42.81	22.41	0.53	81.07	42.43	0.1%	65.65	34.35	68.7 ± 1.7	31.3 ± 1.7
	2			87.8	1790398	809802	35.11	15.88	0.58	60.59	27.41	0.2%	68.86	31.14		
	3			118.7	2486423	1082542	48.75	21.23	0.59	82.90	36.10	0.3%	69.67	30.33		
	4			105.5	1235135	539517	24.22	10.58	0.33	73.91	32.29	0.7%	69.60	30.40		
	5			96.9	1548399	673475	30.36	13.21	0.45	67.04	29.16	-0.7%	69.69	30.31		
ML6	1	Porcine, ex vivo	100	126.8	411840	89755	80.75	17.60	0.78	103.75	22.61	-0.3%	82.11	17.89	92.9 ± 6.0	7.1 ± 6.0
	2			101.4	441870	26423	86.64	5.18	0.91	94.83	5.67	-0.9%	94.36	5.64		
	3			119.6	468682	12739	91.90	2.50	0.78	117.12	3.18	0.6%	97.35	2.65		
	4			104.6	404932	6429	79.40	1.26	0.77	103.36	1.64	0.4%	98.44	1.56		
	5			97.7	381547	19519	74.81	3.83	0.81	92.18	4.72	-0.8%	95.13	4.87		
	6			126.5	465297	52081	91.23	10.21	0.80	113.35	12.69	-0.4%	89.93	10.07		
	7		300	317.2	1077858	148598	211.34	29.14	0.76	279.03	38.47	0.1%	87.88	12.12	86.1 ± 3.2	13.9 ± 3.2
	8			315.1	1057624	239607	207.38	46.98	0.81	257.55	58.35	0.3%	81.53	18.47		
	9			311.9	1105820	139491	216.83	27.35	0.78	277.32	34.98	0.1%	88.80	11.20		
	10			288.5	1031274	166168	202.21	32.58	0.81	249.07	40.13	0.2%	86.12	13.88		

A. *In vivo* injection of ^{99m}Tc solution using ML1 hollow microneedle device to dorsal skin of a Sprague Dawley rat

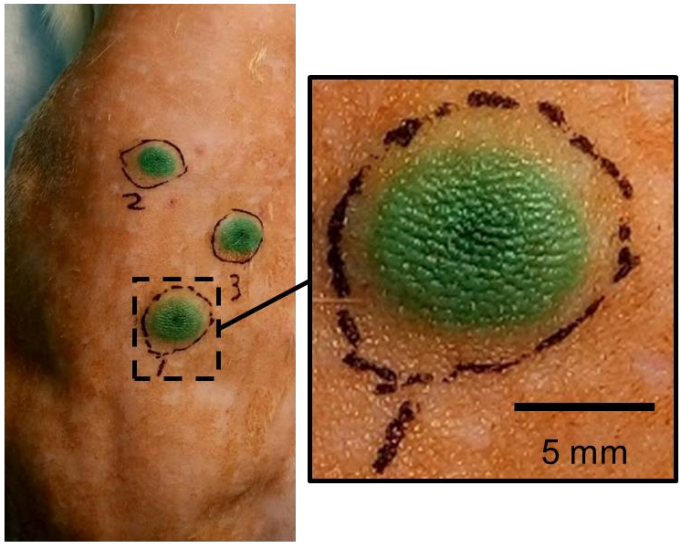

B. *In vivo* fluid delivery profile in Sprague Dawley rats

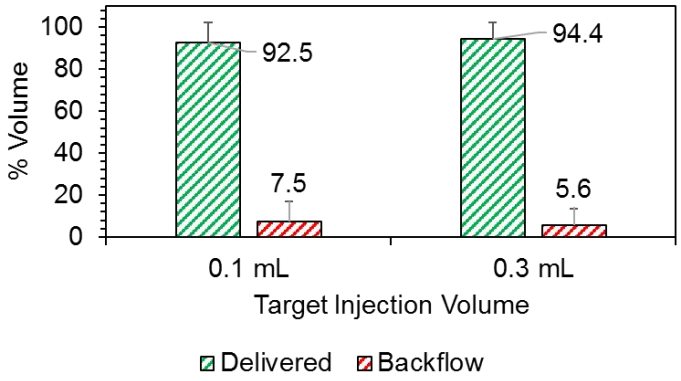

Figure 31. In vivo delivery of $^{99m}TcO_4^-$ solution using the ML1 single microneedle device in Sprague Dawley rats (n=3 for the 0.1 mL injections; n=3 for 0.3 mL injections; error bars represent standard deviation).

5.4. Conclusions

A novel method has been developed to accurately measure fluid paths during ID delivery of pharmaceutical formulations into the skin to determine fluid delivery efficiency and fluid wastage. The use of aqueous formulations with extremely low activities of $^{99m}TcO_4^-$ allowed highly accurate

and sensitive determinations of fluid delivery into the skin as well as the fluid backflow onto the skin surface with lower limits of detection, compared to the conventional gravimetric method. The new method was assessed in *ex vivo* porcine skin and *in vivo* rat skin, and showed that MN devices could accurately deliver more than 86% of intended volume into the dermis. Using $^{99m}TcO_4^-$ will allow assessment of ID delivery devices and methodologies in an optimal and fast way to enable the development of more effective, painless, and potentially self-administrable therapies for patients. The method was effective at demonstrating that mechanically bypassing the SC layer with a minimally invasive device allowed successful ID delivery of fluid; and allowing precise comparison between the performances of ID delivery devices. The MN devices yielded higher fluid delivery efficiencies than hypodermic needles with the Mantoux technique.

6. DESIGN AND DEVELOPMENT OF A HOLLOW MICRONEEDLE-OPTOFLUIDIC BIOSENSOR INCORPORATING ENZYME-LINKED ASSAYS

The work presented in this chapter describes and demonstrates the design considerations for a novel MN-optofluidic biosensing system, assesses the individual components of such a complex system, and demonstrates the potential for a biosensing platform capable of collecting, trapping, and analyzing biological molecules in sub-nanoliter volumes of sample at nano- to micro-molar concentrations, which are the concentrations encountered in ISF samples of a patient that takes TDM drugs.[5] This study utilized streptavidin-horseradish peroxidase (Sav-HRP) as a model biomolecule to interact with a biotinylated MN lumen surface. Sav-HRP bound to biotin on the MN lumen with high affinity was quantified by determining the concentration of the HRP enzyme on the MN lumen using an enzyme-linked absorbance assay. The biotin-streptavidin platform will facilitate the immobilization of specific recognition elements to adapt the sensor for the detection of a plethora of drug candidates.

6.1. Materials and Methods

6.1.1. Materials

The following materials were purchased for this study:

[5] A version of chapter 3 has been has been prepared for publication:

Ranamukhaarachchi S.A., Padeste C., Häfeli U.O., Stoeber B., Cadarso V.J. Design considerations of a hollow microneedle-optofluidic biosensing platform incorporating enzyme-linked assays. (submitted on November 17, 2016).

Thiol-PEG-biotin (mol. wt. 5 kDa, purity > 95%) and thiol-methoxy PEG (thiol-mPEG, mol. wt. 5 kDa, purity > 95%) from Nanocs Inc. (Boston, MA, USA); streptavidin (Sav) from *Streptomyces avidinii* (lyophilized powder, mol. wt. 60 kDa), and 3,3'5,5'-tetramethylbenzidine (TMB, purity ≥ 95% NT, mol. wt. 240.34 Da) from Sigma-Aldrich (Buchs, Switzerland); Sav-HRP conjugate (2.5 mg mL^{-1}, mol. wt. 110 kDa) from Invitrogen Corporation (Camarillo, CA, USA); hydrogen peroxide (30% H_2O_2, Perhydrol®) from Merck (Darmstadt, Germany); SU-8 2075 photo-curable polymer resist and the propylene glycol methyl ether acetate (PGMEA) developer from MicroChem (Newton, MA, USA); and PDMS (Sylgard 184) from Dow Corning Corp (Midland, MI, USA).

Single hollow metallic MN devices were fabricated as described in Section 1.2.1.2. Electroplated metal sheets with MNs were cut into smaller circular pieces (3 mm diameter, and 7.1 mm^2 area). Hereforth, a "MN backside" refers to the backside surface of such a 3 mm diameter circular sheet of gold-coated nickel containing a single out-of-plane hollow MN (the side of the metal sheet opposite the protruding MN). The surface area of the MN backside and inner lumen are 7.1 mm^2 and 0.06 mm^2, respectively. All surfaces were cleaned using UV irradiation at a 170 nm wavelength for 10 min using a flat excimer Ex-Mini source (Hamamatsu, Japan).

6.1.2. Microneedle Surface Functionalization

6.1.2.1. Self-assembled monolayers

The well-understood Sav-biotin binding was used to assess the ability to perform bio-recognition assays on MN surfaces. The Sav-biotin interaction has been widely used to construct functional

surfaces due to its high affinity binding and bond stability. It can act as a linking platform to build surfaces with a large variety of functional moieties, in a step-wise fashion.

Thiol-PEG-biotin and thiol-mPEG conjugates were employed to construct self-assembled monolayers (SAM) on gold surfaces [148, 149]. A 5,000 Da PEG chain (PEG-5000) was selected due to its ability to reduce non-specific adsorption of proteins in biological fluids [150]. Thiol-PEG-biotin and thiol-mPEG solutions were prepared fresh by dissolving in milliQ water to a concentration of 1 mM. Thiol-PEG-biotin to thiol-mPEG molar fractions ranging from 0-1.0 (referred to as "PEG-biotin solutions" hereforth) were obtained and tested to determine the optimum surface density of biotin on the gold-coated substrates for Sav binding. Droplets of 5 µL from each PEG-biotin solution were incubated on the MN backside surfaces for 2 h at room temperature (Figure 32A). The gold-surfaces were withdrawn from the PEG-biotin solutions, and washed with phosphate buffer. Sav-HRP (2.5 mg mL^{-1}) was diluted with phosphate buffered saline (PBS) to a concentration of 10 µg mL^{-1} (0.1 µM). Biotin-functionalized MN backside surfaces were incubated with 5 µL droplets of 0.1 µM Sav-HRP for 1 h at room temperature, followed by three PBS washing steps. Sav-HRP was quantified using the 3,3'5,5'-tetramethylbenzidine (TMB) assay, as described below.

6.1.2.2. Streptavidin-HRP Binding

MN backside surfaces functionalized with a SAM of 0.1 molar ratio of thiol-PEG-biotin to thiol-mPEG were incubated with 5 µL droplets of Sav-HRP (concentrations ranging from 1.9-192 µM) for 1 h at room temperature to determine the level of bound Sav-HRP. At the end of the incubation

period, the MN bases were washed with PBS and assessed for the Sav-HRP levels using the TMB assay.

6.1.3. 3,3'5,5'-Tetramethylbenzidine (TMB) Assay

The enzyme-linked TMB assay is used to quantify the activity of the enzyme HRP. HRP oxidizes 3,3'5,5'-tetramethylbenzidine (colorless) in the presence of hydrogen peroxide, changing the color of the TMB solution to blue, which can be detected at a wavelength of 635 nm (as shown in Figure 32). The Sav-HRP conjugate is used as a model drug to quantify binding concentrations of molecules to the MN surfaces. The absorbance of the TMB oxidation end-product correlates to the concentration of Sav-HRP conjugate present on a surface.

6.1.3.1. Conventional TMB Assay

After binding the Sav-HRP conjugate to the MN backside, a 10 µL droplet of the TMB stock solution (0.4 mM TMB, 0.04 mM H_2O_2 in 0.1 M citrate buffer, pH 6.8) was placed on top of the functionalized MN backside, and incubated for 10 min at room temperature to allow the HRP to produce the TMB oxidation end-product. After 10 min, a 2 µL volume of the TMB solution was extracted from the MN backside surface, and its absorbance at 635 nm was determined using a NanoDrop ND-1000 spectrometer (ThermoFischer Scientific, Waltham, MA, USA).

6.1.4. Preparation of Masters and Molds for the Optofluidic Device

Two masters (a master 1 for the optical waveguide and fiber alignment, and master 2 for the integration of surface functionalized MN bases to the optofluidic devices) were fabricated with a SU-8 negative photoresist using photolithography according to manufacturer recommendations with minor modifications. SU-8 2075 was spin-coated on a SiO_2-coated silicon wafer at 1700 rpm

for 35 s to obtain a 150 µm thick layer for master 1. Following a soft-baking step at 95°C for 30 min, the SU-8 was exposed to UV light (240 mJ cm^{-2}) through a photomask. An immediate post-exposure baking step was conducted directly at 95 °C for 5 min, followed by SU-8 development in PGMEA for 12 min.

Master 2 was fabricated using two SU-8 2025 layers aligned on top of each other for MN placement and attachment to the optofluidic device. Layer 1 was spin coated to obtain a 50 µm feature height (1750 rpm), followed by a soft-baking step at 65°C for 3 min and 95°C for 9 min. Layer 1 was exposed to UV light (240 mJ cm^{-2}) through a photomask. An immediate post-exposure baking step was conducted at 65°C for 2 min and at 95°C for 7 min. Layer 2 was spin coated to obtain a 20 µm feature (4000 rpm) and soft-baked on top of layer 1 at 65°C for 3 min and 95°C for 6 min; and exposed to UV light (240 mJ cm^{-2}) through a photomask with precise alignment to the first exposure. Another post-exposure baking step was conducted at 65°C for 1 min and at 95°C for 6 min, followed by SU-8 development in PGMEA for 10 min.

A Sylgard 184 PDMS kit was used to weigh and mix thoroughly 30 g of its base solution to 3 g of its cross-linking agent (10:1 wt:wt base to cross-linker ratio). The PDMS mixture was degassed under vacuum, poured onto the SU-8 masters, and cured at 80°C for 1 h to obtain 3 mm thick PDMS slabs with transferred structural features. Once peeled off of the masters, PDMS replicates from master 1 and master 2 were aligned and bonded to each other using PDMS catalyst bonding, according to Samel et al. [151] to securely seal the optofluidic channels and prevent leaking.

6.1.5. Integrating the Microneedle to Optofluidic Sensing Device

To create a continuous biosensing system without major and time-consuming moving parts, a surface functionalized MN was integrated into an optical sensing unit that acts simultaneously as a microfluidic detection chamber and as an optical waveguide, forming an optofluidic device (OFD; Figure 33). It was designed to measure in situ the absorbance of end-products from enzymatic reactions that take place on the MN surface, using a simple diode laser and a photodetector. The MN was attached to the OFD transducer made of PDMS (Figure 33A and B). The area surrounding the microfluidic inlet, where the surface-functionalized MN base was attached, was first treated for a few seconds with an atmospheric-pressure helium plasma to decrease the surface contact angle. The MN base was aligned with the microfluidic inlet and placed on the PDMS surface, followed by application of an instant-bonding cyanoacrylate adhesive around the circular MN base perimeter. The adhesive completely cured within 10 min, allowing the use of the MN-integrated OFD device for biosensing experiments.

The detection chamber/optical waveguide (hereforth referred to as the "OFD waveguide"), which is the main component of the device, was fabricated with dimensions of 150 µm height, 50 µm and 100 µm widths, and 0.1 to 5 mm lengths. Light was coupled in and out of the OFD using a luminescent diode laser (635 nm, 1 mW), which was coupled to a 4 µm diameter single-mode optical input fiber. A 50 µm diameter multi-mode output fiber was connected to a silicon PIN photodiode (PM100D compact power and energy meter console; Thorlabs, NJ, USA) and was placed 30 µm away from the opposite end of the OFD waveguide to collect the output light from the waveguide at a frequency of 1 Hz. The fluid inlet to the OFD was through the MN base, while the outlet was connected to a syringe pump to improve fluid flow control.

The optical properties of the devices were characterized using methyl green, a dye which absorbs light at 635 nm, similar to the TMB oxidation end-product. Methyl green was diluted to an absorbance reading of 2.5 AU per 10 mm path length.

6.1.6. Microneedle-Optofluidic Device Performance

Biosensing tests using the MN-OFD biosensor were conducted as follows:

1. To assess the performance of MN backsides, a 5 μL volume of Sav-HRP (concentration ranging from 4.8 nM to 57.7 μM) was placed on the MN outer surface and gradually pulled into the reaction chamber (MN backside and lumen), allowing the Sav-HRP to interact with surface-bound biotin. Similarly, to assess the performance of MN lumens only, a 1 μL volume of Sav-HRP was placed on a glass slide, and the MN tip was brought in contact with the droplet for 30 s to allow capillary flow of 0.6 nL of Sav-HRP into the MN lumen.
2. After 10 minutes of incubation, the Sav-HRP solution was removed from the MN by flushing the device with 20 μL of phosphate buffer (using the syringe pump).
3. A 10 μL droplet of the TMB solution (0.4 mM TMB, 0.04 mM H_2O_2) was placed on the MN outer surface. The TMB solution was guided through the Sav-HRP on the MN lumen and backside into the waveguide at a flow rate of 10 nL s^{-1} for 240 s.
4. After 240 s, the remaining TMB solution from the MN outer surface was removed and replaced by 50 μL phosphate buffer, which was flushed through the system to terminate the enzymatic reaction and the biosensing process.

In the case of performing multiple TMB biosensing cycles in one device, steps 2-3 were repeated (at same or different TMB concentrations). From the data collected, average absorbance (at

635 nm) of the TMB oxidation end-product was determined during the 196 s to 205 s time interval to compute the TMB calibration curves in the biosensor.

6.2. Results and Discussion

6.2.1. Surface Functionalization

SAMs containing thiol-PEG-biotin were formed and optimized on the gold-coated backside surfaces of MN bases to accommodate optimal binding of Sav. Thiol-PEG-biotin to thiol-mPEG fractions, including 0, 10, 20, 50 and 100 mol% were tested for Sav binding. The highest level of Sav binding was found for surfaces functionalized with a 10 mol% thiol-PEG-biotin and 90 mol% thiol-mPEG (0.63 ± 0.05 AU). This was three-fold greater than the level of Sav binding in a surface functionalized with 100 mol% thiol-PEG-biotin (0.19 ± 0.05 AU). As a result, a 10 mol% thiol-PEG-biotin to 90 mol% thiol-mPEG was used in all further SAM formations on MN backsides and lumens.

MN backsides functionalized with thiol-PEG-biotin were tested for Sav-HRP binding to determine the specific Sav-biotin binding behavior, including the linear binding range and binding saturation levels (Figure 32A and B). A conventional TMB assay was conducted on MN backsides to determine the level of bound Sav (Figure 32C). Sav-HRP binding to the biotinylated MN backside was linear up to 38.5 nM at a sensitivity of s=8.59 AU μM^{-1} and a LoD of 0.83 nM (Figure 32D). The measurement sensitivity was determined by the slope of the linear binding range in Figure 32D.The LoD

$$LoD = \frac{3 \times \sigma_{blank}}{s} \qquad (13)$$

was calculated from the standard deviation of a blank measurement σ_{blank} and the measurement sensitivity s. The highest Sav-HRP binding was observed at 38.5 nM (0.36 ± 0.05 AU), after which the signal decreased, and then stabilized around 0.15 to 0.20 AU (data not shown).

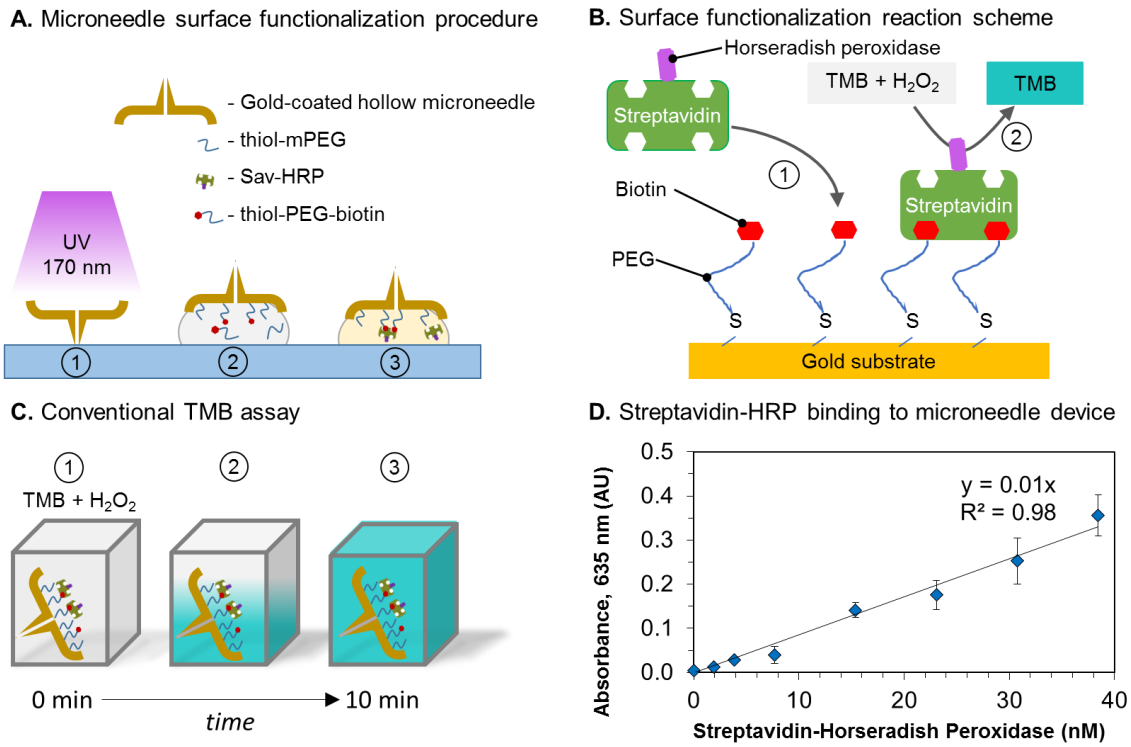

Figure 32. Microneedle surface functionalization. (A) Microneedle devices were functionalized with thiol-PEG-biotin to determine and optimize the functionalization process and streptavidin binding. The backside of gold-coated hollow single microneedle devices (7.1 mm² area) were cleaned by UV irradiation (A-1), incubated with PEG-biotin solutions (A-2), and bound with Sav-HRP (A-3) at 22°C for 1 h. (B) The model-biosensing reaction scheme involved binding Sav-HRP (B-1) and quantifying the bound Sav-HRP level by using the enzyme-catalyzed TMB oxidation (B-2). (C) The conventional TMB assay parameters were optimized using a NanoDrop UV spectrometer (1 mm path length). A colorless TMB solution was converted by HRP in the presence of H_2O_2 (C-1) to a TMB oxidation end-product (blue color) over a 10 min reaction period (C-2 and C-3), absorbance of which was quantified at 635 nm. (D) The amount of Sav-HRP bound to the microneedle device surface was quantified using the TMB assay to provide a direct binding curve.

The decrease and stabilization in the signal may be attributed to effects from the competition between free Sav and bound Sav on the biotinylated surface at high Sav concentration; an effect of the four-fold biotin-binding capability per Sav; and/or the conformational differences in Sav binding to biotin on the surface at concentrations higher than 38.5 nM. The linear Sav binding range presented in Figure 32D indicated that molecule binding and detection can be performed on the biotinylated MN surfaces.

6.2.2. Optofluidic Device Optimization

The OFD's sensing characteristics were optimized prior to performing binding and detection of Sav-HRP. A number of parameters of the sensing system, including the integration of air mirrors, and the OFD waveguide width and length were manipulated to enhance the sensitivity of detection, while ensuring that the sensing occurred in the linear detection range for the TMB assay at given reactant concentrations. The OFD waveguide was designed to enhance the interaction between the light and the colored fluid in the sensing chamber. In principle, the reflection of the light at the chamber (n_{water}=1.33) and PDMS (n_{PDMS}=1.41) interface is based on hollow waveguide confinement [152], since n_{water} is smaller than n_{PDMS}. However, a significant optical signal was lost in this form of light refraction out of the waveguide (up to 23 dB). The intrinsic optical losses were significantly reduced to 17 dB by engineering air-mirrors along the waveguide to reflect optical transmissions back towards the OFD waveguide (Figure 33) that would otherwise be unrecoverable and continue to propagate away from the OFD waveguide and the optical output fiber. Air mirrors introduced the total internal reflection phenomenon to reflect a large amount of incident light back to the OFD waveguide, to minimize optical losses from the OFD system. The self-aligning feature for optical fibers and air-mirrors helped to increase the SNR of the OFD.

During the optimization of the OFD, the optical signal transmission through the citrate flow buffer (at a 10 nL s^{-1} flow rate) was measured in OFD waveguides of varying dimensions with length and width ranging from 0.1-5.0 mm and 50-100 µm, respectively (Figure 34A). From the 1 mW diode laser input power at 635 nm that was fed into the OFD waveguide, the mean power of noise from the OFD was ± 50 pW, while the optical output power through the buffer-filled OFD waveguide ranged from 1-443 µW. This provided the biosensor with a high SNR between 44.5-69.5 dB for reliable optical measurements. The optical losses through the buffer-filled OFD waveguide increased linearly as a function of its length. At very short lengths (0.1-0.5 mm), the 50 µm OFD waveguide channel width yielded lower optical losses compared to the 100 µm channels. Beyond 1 mm channel length, the 50 µm channel width provided higher optical losses than the 100 µm width.

Methyl green (0.001 vol%), a dye absorbing light at 635 nm wavelength similar to the oxidation product of TMB, was used to characterize the absorbance in the OFD waveguide due to the presence of a dye (Figure 33B). A linear increase in the absorbance of methyl green was observed as a function of the OFD waveguide length for both 50 µm and 100 µm width levels, as expected by the Beer-Lambert law. The absorbance sensitivity determined in the OFD waveguide with a 50 µm width was slightly higher compared to a device with 100 µm width. The 5 mm long and 50 µm wide OFD waveguide yielded the highest absorbance in the linear range for methyl green (2.3 AU). Beyond 5 mm in length, absorbance values deviated from linearity for both widths (data not shown). As a result, an OFD waveguide with 5 mm length and 50 µm width was chosen to integrate a surface functionalized MN for proof-of-concept biosensing using the Sav-biotin scheme in

Figure 32B. This waveguide also provided an extremely low fill volume of ~40 nL of TMB end-product for measurement, which allowed for rapid measurement with minimal reagent use.

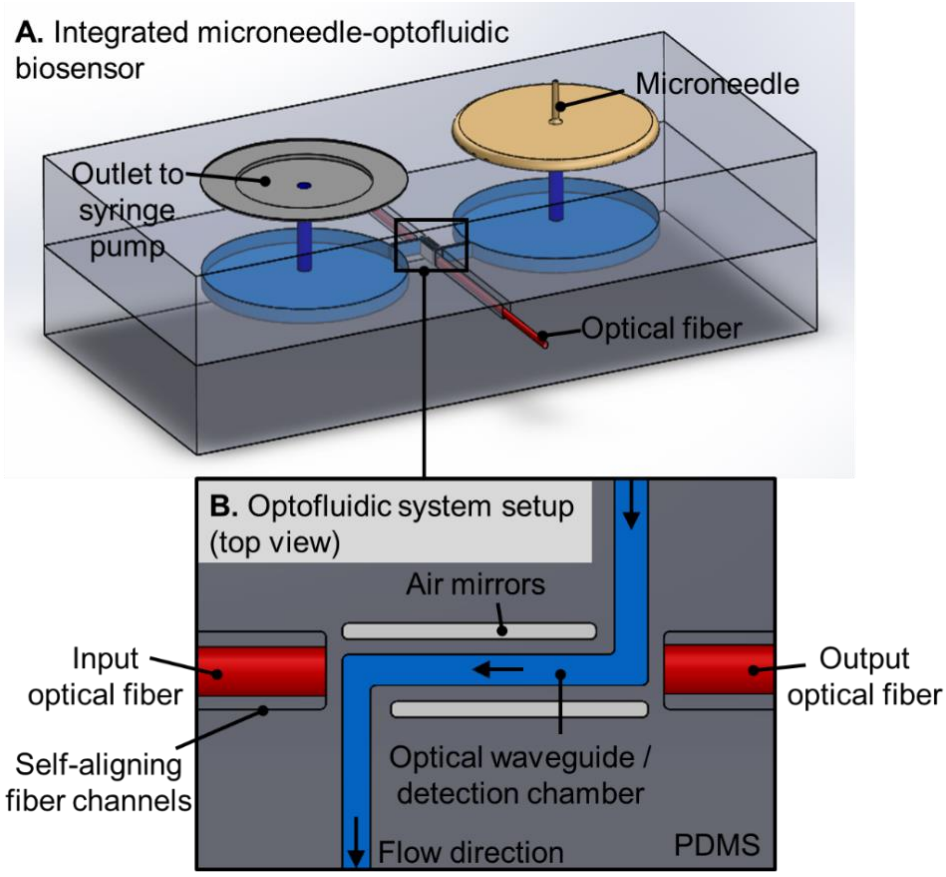

Figure 33. Conceptualization of the microneedle-optofluidic biosensor and its components. (A) A hollow gold-coated microneedle that was surface-functionalized for analyte collection, binding, and detection was integrated to an optofluidic sensing system for analyte concentration determination. (B) Top view of the optofluidic device, illustrating the TMB end-product flow direction through the optical waveguide/detection chamber, locations of the optical fibers, and the position of the air mirrors. Refractive indices of the optofluidic components are n_{air} = 1.0, n_{water} = 1.33, and n_{PDMS} = 1.41.

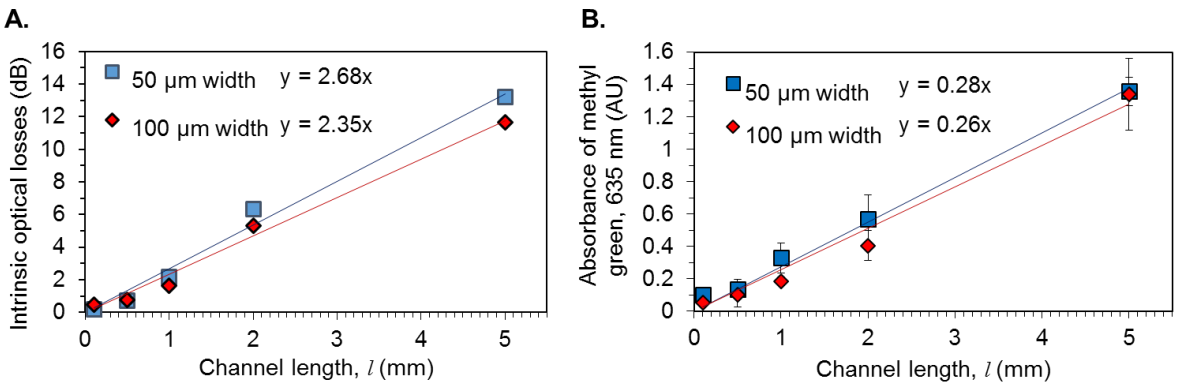

Figure 34. Optimization of the optofluidic device. (A) The width and length dimensions of the OFD waveguide were modified and tested for intrinsic optical losses using citrate buffer. (B) The absorbance of 0.001 vol% methyl green dye in absorbance units (AU), a TMB oxidation-product simulant, as a function of channel dimensions.

6.2.3. Performance of the Integrated Microneedle-Optofluidic Biosensor

The MN-OFD was first used to assess the binding of Sav-HRP to the entire surface of the MN backside (Figure 35A and B). To utilize the functionalized MN backside (7.1 mm^2 area), a 5 µL droplet of Sav-HRP with concentrations up to 58 nM was brought into the MN base through the MN lumen by suction flow generated using a syringe pump. After 1 min of incubation, the Sav-HRP was removed from the MN backside. A TMB droplet was placed on the MN and flowed into the OFD through the MN lumen at a rate of 10 nL s^{-1}, providing time for contact between the TMB reactants and the HRP bound to the MN backside and producing the colored end-product that was measured in the OFD waveguide (Figure 35A).

The rate of TMB conversion to its oxidation end-product reached a plateau within 2-3 minutes due to enzyme saturation and/or activity depreciation. The average absorbance at 200 ± 5 s after the reaction started was used to establish a calibration curve for the binding of Sav-HRP to the MN backside (Figure 35B). Sav-HRP binding and detection in the biosensor yielded a linear detection

range from 1.14-38.5 nM at a sensitivity of 10.6 AU μM^{-1}, providing a comparable translation of the conventional TMB assay that was conducted on the MN backside surface (Figure 32D) to the biosensor with about 2/3 reduced measurement time. Given that the volume of the OFD waveguide was ~40 nL and the TMB measurement only required ~3 minutes of flow through the MN surface at 10 nL s^{-1}, the measurement could be performed with less than 5 µL of the TMB stock solution in the biosensor. The LoD in the biosensor (1.14 nM Sav-HRP, determined using equation 1) was comparable to the conventional TMB assay (0.83 nM Sav-HRP); while the biosensor yielded a higher sensitivity (10.6 AU μM^{-1}) compared to the conventional TMB assay for the MN backside (8.59 AU μM^{-1}).

To demonstrate the specificity of Sav binding to the modified MN backside surface, a biotin-less self-assembled monolayer (100 mol% thiol-mPEG) was incubated with the highest concentration of Sav-HRP (38.5 nM) and assessed using the TMB assay in the biosensor (Figure 35A). Lack of binding of Sav-HRP to the MN backside was evident by the absence of TMB oxidation (baseline result) in Figure 35A.

6.2.4. Biosensing in the Microneedle Lumen

Having confirmed the functionality of the biosensor, the potential to bind Sav-HRP only inside the MN lumen was assessed. During SAM formation on the MN base, the inner MN lumen containing an electrodeposited layer of gold was also functionalized with the biotinylated thiol-PEG layer. During Sav-HRP binding, capillary forces were used to fill the MN lumen without allowing the sample to come in contact with the backside surface of the MN device, ensuring that only 0.6 nL of volume filled the MN lumen and interacted with the 0.06 mm^2 surface area. Significantly higher

Sav-HRP concentrations (>0.5 µM) were needed to achieve a detectable signal from the MN lumen only due to a significant reduction in the active surface area where biotin molecules were present for bio-recognition and binding of Sav-HRP; and the extremely low quantity of Sav-HRP molecules present in the 0.6 nL sample volume at concentrations lower than 0.5 µM. Above 0.5 µM, Sav-HRP bound to biotin in the MN lumen in sufficient quantities to allow detection using TMB (Figure 35C and D). Sav-HRP binding in the MN lumen followed a linear trend up to 7.21 µM at a detection sensitivity of 0.17 AU μM^{-1} and a LoD of 60.2 nM. Beyond 7.21 µM, Sav-HRP binding saturated the surface and hindered further binding. The linear Sav-HRP detection range and the LoD in the MN lumen was significantly higher than for the MN backside surface, while the detection sensitivity was significantly lower than for the MN backside. Nonetheless, the binding and detection of Sav-HRP in a MN lumen with only 0.6 nL is the smallest reported biosensing volume used in a MN-based assay. In comparison, other MN-based technologies required more than 1000 times higher sensing fluid volumes (> 1 µL) [26, 45, 51].

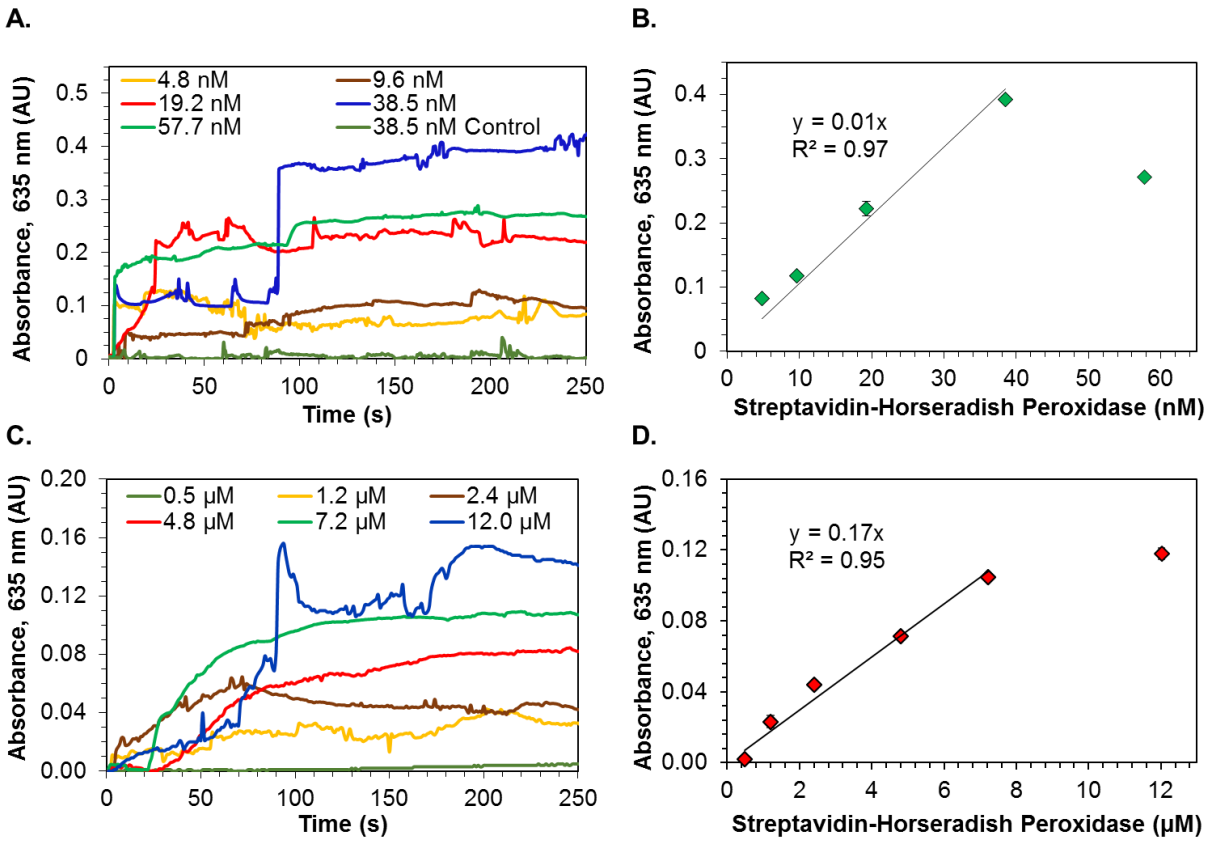

Figure 35. Detection of Sav-HRP in microliter volumes in the microneedle-optofluidic biosensor. (A) The level of Sav-HRP bound to the microneedle backside (5 µL volume, 7.1 mm^2 area) was measured by the biosensor from TMB absorbance between 196-205 s to produce (B) a direct Sav-HRP binding curve (n=10 data absorbance points; and error bars represent standard deviations). The "38 nM Control" in A refers to unlabeled Sav without conjugated HRP. (C) The level of Sav-HRP bound to the microneedle lumen (0.6 nL volume, 0.06 mm^2 area) was measured from TMB absorbance between 196-205 s to produce (D) a direct binding curve (n=10 and error bars represent standard deviations).

A summary of key results from the MN-OFD biosensor is presented in Table 11.

Table 11. Performance summary for the microneedle optofluidic biosensor and the conventional biosensing assay.

Detection of Sav-HRP	**Conventional assay**	**Microneedle-optofluidic biosensor**	
Functionalized surface	Microneedle backside	Microneedle backside	Microneedle lumen
Sample volume	5.0 µL	5.0 µL	0.6 nL
Sensing area	7.10 mm^2	7.10 mm^2	0.06 mm^2
Maximum detectable concentration (in the linear range)	38.50 nM	38.50 nM	7.21 µM
Sensitivity	8.59 AU μM^{-1}	10.60 AU μM^{-1}	0.17 AU μM^{-1}
Limit of detection	0.83 nM	1.14 nM	60.20 nM
Time	10 min reaction 1 min measurement	3.5 min reaction and measurement	

6.2.5. Additional Utility of the Biosensor

The MN-OFD biosensor can also be used as an enzyme sensor to study enzyme kinetics and dynamics, and to optimize enzyme reaction conditions. As an example, the relationship between one reactant (H_2O_2) and an enzyme's turnover was determined by binding 38 µM Sav-HRP to the MN (Figure 36A). A linear dependency of the measured absorbance on the concentration of H_2O_2 was observed up to about 0.08 mM. Above that concentration, the enzymes saturated and thereby limited the progress of the TMB reaction. In addition, the stability of Sav-HRP on the MN surface was demonstrated in Figure 36B**,** where repeated TMB measurements yielded consistent absorbance values with no visible decrease in the TMB signal.

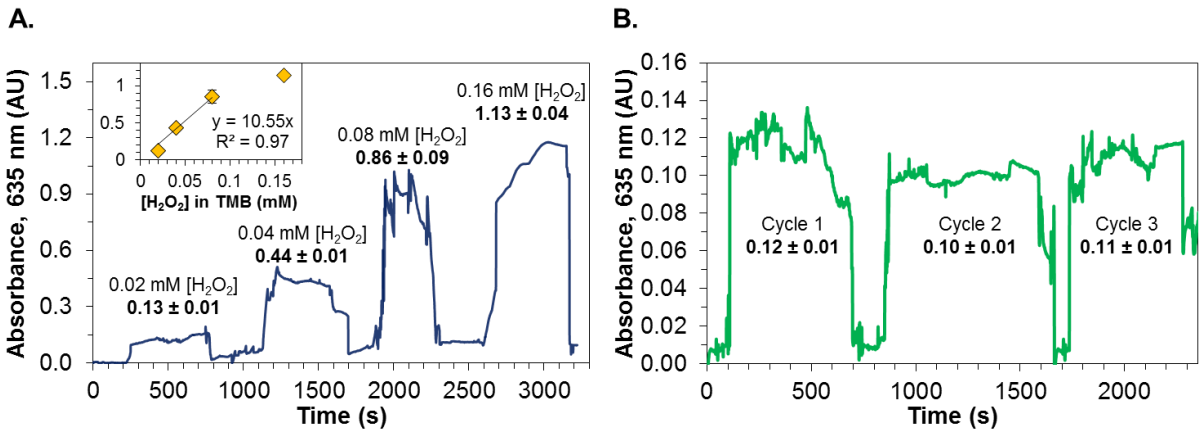

Figure 36. Utility of the microneedle-optofluidic sensor as an enzyme sensor. (A) Response of the HRP enzyme to increasing levels of hydrogen peroxide from 0.02-0.16 mM to determine the optimal reactant concentrations (38 µM Sav-HRP). A calibration curve of TMB absorbance versus H_2O_2 concentration (A-inset) showed the linear range for H_2O_2. (B) Repeatability of the TMB assay measurements in the sensor over multiple TMB cycles (9.6 µM Sav-HRP, 0.04 mM H_2O_2). Peaks represent activity of the HRP to produce the colored TMB end-product, while valleys represent washing of the microneedle surface with phosphate buffer to remove reactants from the system.

6.3. Conclusions

The process of developing a proof-of-concept biosensor integrating surface-functionalized hollow metallic MNs and an OFD sensor was demonstrated using the universal Sav-biotin platform that can be adapted to the detection of a myriad of highly relevant analytes such as TDM drugs. Different components of the biosensor have been optimized to obtain a highly performing OFD capable of sensing analytes in volumes below 1 nL. The biosensor was validated *in vitro* by detecting the binding of Sav-HRP to a biotinylated thiol-PEG monolayer on the MN surface at extremely low LoD ranging from 1.1-60.2 nM. Furthermore, this detection was performed in real-time using extremely low sample volumes that are not otherwise possible with conventional assays, which usually require more than 1 µL of sample for analysis. All components of the biosensor provided great flexibility and avenues for optimization of the performance of the sensing

system for specific TDM drug candidates and applications. Drug-specific biotinylated ligands may be used to recognize and detect drug candidates in extremely low volumes of biological fluids and bind them to the Sav inside the MN lumen. This biosensing platform will pave the way to the development of patient-friendly, painless, minimally-invasive, and point of care diagnostic tools for specific TDM applications.

7. THERAPEUTIC DRUG MONITORING WITH AN INTEGRATED HOLLOW MICRONEEDLE-OPTOFLUIDIC BIOSENSOR

This chapter utilized the MN-OFD biosensor designed in chapter 6 to develop a TDM system for vancomycin (VAN), since VAN is a TDM candidate that can be detected in ISF, as described in section 1.2.1.3.[6] As an important antibiotic against gram-positive bacteria, such as Staphylococcus *Aureus*, VAN exerts its antibacterial effects by binding to peptides terminating with the C-terminal lysine-d-alanine-d-alanine (KAA) tripeptide motif in the bacterial cell wall [43, 153] with moderate affinity (K_D=1-100 μM), leading to bacterial termination [43]. In this chapter, we functionalized the MN lumen surface with the acetyl-lysine-d-alanine-d-alanine (AcKAA) peptide by building on the existing thiol-PEG-biotin and Sav bound surface from chapter 6, as shown in Figure 37. A competitive binding scheme was used to bind and detect unlabeled and native VAN, where a VAN-HRP conjugate was pre-bound to the AcKAA surface. VAN in a sample of interest competed for AcKAA ligands with pre-bound VAN-HRP and displace them in a concentration dependent manner. The VAN concentration in the sample of interest was determined indirectly, by quantifying the remaining HRP concentration using the TMB assay.

[6] A version of chapter 7 has been published:

Ranamukhaarachchi S.A., Padeste C., Dübner M., Häfeli U.O., Stoeber B., Cadarso V.J. Integrated hollow microneedle-optofluidic biosensor for therapeutic drug monitoring in sub-nanoliter volumes. Scientific Reports 6, Article number: 29075 (2016) doi:10.1038/srep29075.

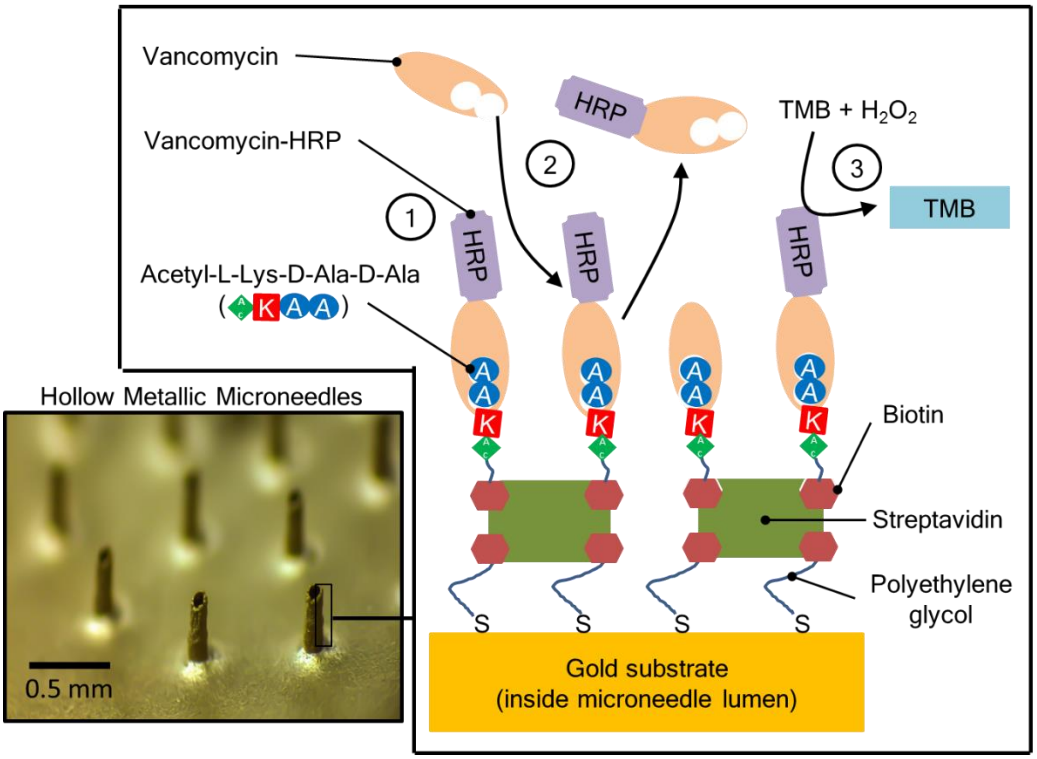

Figure 37. The chemical reaction scheme for the detection of vancomycin in low volume samples inside microneedle lumens. Vancomycin-HRP was pre-loaded to the microneedle surface (1). Vancomycin present in the sample competed for the acetyl-L-lysine-D-alanine-D-alanine binding sites on the microneedle surface and displaced vancomycin-HRP (2). The enzyme-linked TMB assay was used to quantify (in the optofluidic detection chamber/waveguide) the level of bound vancomycin-HRP remaining on the surface (3).

7.1. Materials and Methods

7.1.1. Materials

In addition to the materials listed in section 6.1.1, the following materials were obtained. Acetyl-lysine-d-alanine-d-alanine (AcKAA, mol. wt. 330.38 Da) peptide (purity ≥ 95% HPLC), vancomycin hydrochloride (100 mg mL^{-1} in DMSO, 0.2 µm filtered, mol. wt. 1449.25 Da), Sav from *Streptomyces avidinii* (lyophilized powder, mol. wt. 60 kDa), 3,3'5,5'-tetramethylbenzidine (TMB, purity ≥ 95% NT, mol. wt. 240.34 Da), and biotin-labelled bovine serum albumin (biotin-

BSA; 8-16 mol biotin per mol BSA) were purchased from Sigma-Aldrich (Buchs, Switzerland). The vancomycin-horseradish peroxidase conjugate (VAN-HRP, 1 mg mL^{-1}, mol. wt. 45 kDa) was purchased from Cal Bioreagents (San Mateo, CA, USA); and the EZ-Link sulfo-NHS-LC-biotin was purchased from ThermoFischer Scientific (Waltham, MA, USA).

7.1.2. Microneedle Fabrication

MNs employed in this study were fabricated as described in section 1.2.1.2, and cleaned as described in section 6.1.2.

7.1.3. 3,3'5,5'-Tetramethylbenzidine Assay

In this study, Sav-HRP and VAN-HRP conjugates were used to quantify binding concentrations of biomolecules to the respective surfaces. The absorbance of the TMB oxidation product correlated to the concentration of HRP-conjugate present on a surface and thus the concentration of analyte bound (i.e., Sav-HRP or VAN-HRP).

The TMB assay reagent concentrations were optimized to provide a maximum absorbance of 3.0 AU throughout the study. The TMB assay consisted of two solutions: Solution A contained TMB at 0.4 mM, prepared by dissolving 0.1 g of TMB in 2 mL acetone and 18 mL of methanol. Solution B was the TMB reaction buffer solution, which was prepared by dissolving 22.06 g citric acid monohydrate (0.1 M), 5.6 g potassium hydroxide (0.1 M), and 20 µL of 30% hydrogen peroxide (0.4 mM) in 500 mL of milliQ water. Immediately prior to conducting the TMB assay, 50 µL of solutions A and 1 mL of solution B were pre-mixed to obtain the TMB stock solution.

After binding a HRP-conjugate to a MN base, the conventional TMB assay was conducted according to section 6.1.3.1.

7.1.4. Microneedle Surface Functionalization

7.1.4.1. Self-assembled monolayers

MN surfaces were cleaned and functionalized with a SAM containing thiol-PEG-biotin as described in sections 6.1.2.1 and 6.1.2.2, respectively. MN base inner surfaces containing a SAM of 10% molar ratio of biotin-PEG-S: mPEG-SH were incubated with 5 µL droplets of free Sav (2.4 µg mL^{-1}, 0.1 µM) on Parafilm-coated glass slides for 1 h at room temperature, to allow the high-affinity binding of Sav to biotin. Sav was used as a stable anchor, as described in 6.1.2, for subsequent immobilization of drug-specific ligands on MN surfaces (i.e., AcKAA peptide for VAN binding; Figure 36). At the end of the incubation period, the MN bases were removed from the incubation slides, and washed three times with PBS.

7.1.4.2. Vancomycin-HRP Binding

A sulfo-NHS-LC-biotin linker (6.24 mM, 4.18 mg mL^{-1}) was mixed with a 6.24 mM AcKAA in PBS (2.04 mg mL^{-1}) at a volumetric ratio of 1:1, and incubated for 30 min at room temperature to produce the biotin-AcKAA conjugate. MN bases functionalized with Sav were incubated with 5 µL of the 6.24 mM Biotin-AcKAA conjugate for 1 h at room temperature to immobilize the surface ligand to promote vancomycin binding (Figure 37). The MN base surfaces were washed with PBS buffer three times.

To minimize non-specific binding of VAN-HRP to the MN base surface and to promote binding to the AcKAA peptides, the surfaces were further treated with BSA (1 mg mL^{-1}) for 30 min at room temperature. The MN base surfaces were washed with PBS buffer three times.

VAN-HRP concentrations ranging from 0.02-2.20 μM (1-100 μg mL^{-1}) were made from a stock solution at 22 μM (1 mg mL^{-1}). Each VAN-HRP concentration level was tested on five MN bases (n=5) that were functionalized with the AcKAA peptide to determine the VAN-HRP binding behavior as a function of concentration. A 5 μL volume of each VAN-HRP solution was incubated on the MN base for 10 min at room temperature, allowing VAN-HRP to bind to the AcKAA peptide. At the end of the incubation, the MN bases were washed with PBS and tested using the TMB assay to quantify the bound VAN-HRP content. From the absorbance data obtained, a calibration curve (absorbance versus VAN-HRP concentration) was constructed for VAN-HRP binding to the MN base at a 7.1 mm^2 area (discussed later in section 7.2.1).

7.1.4.3. Vancomycin Binding

In MN bases that were incubated with VAN-HRP, a subsequent binding of VAN at concentrations ranging from 0-72.6 μM was performed. VAN concentrations ranging from 0.07-72.6 μM (0.11-105 μg mL^{-1}) were made from a stock solution at 69 mM (100 mg mL^{-1}). A 5 μL volume of each VAN concentration level was incubated on the MN base surface for 10 min at room temperature, allowing VAN to bind to unoccupied AcKAA peptides on the surface or displace bound VAN-HRP from the AcKAA peptides. At the end of the incubation, the MN bases were washed with PBS and tested using the TMB assay to quantify the effect of VAN concentration on the competitive displacement of bound VAN-HRP from the MN base. From the absorbance data

measured during the TMB assay, a VAN competitive binding curve was constructed for MN bases at a 7.1 mm^2 area (discussed later in section 7.2.1).

7.1.5. Performance of the Microneedle-Optofluidic Sensor

The setup and optimization of the OFD, as well as the MN integration to the OFD was done as described in 6.1.5. A 5 mm long and 50 µm wide waveguide was selected for the OFD sensing device.

Biosensing tests using the MN-OFD biosensor were conducted according to Figure 38. MN tips of integrated biosensor devices equipped with optical fibers were brought in contact with 1 µL droplets of 0.22-2.20 µM VAN-HRP on a Parafilm-coated glass slide for 60 s, allowing sufficient time for the MN lumen to fill via capillary action (Figure 38A). VAN-HRP was incubated inside the MN lumen for 10 min at room temperature, followed by washing the MN lumen with PBS (Figure 38B). During the washing step with PBS, the optical output power collection process was initiated to obtain a baseline stabilized optical readout for PBS flow through the optical waveguide and MN lumen. A 50 µL droplet of the TMB stock solution was placed on the MN base. A suction-flow of 10 nL s^{-1} was established through the MN and the waveguide using a syringe pump that was attached to the fluid outlet of the biosensor. The TMB stock solution was flown through the biosensor for 300 s, and afterwards replaced with 50 µL of PBS to wash away any unreacted TMB stock solution from the biosensor.

MN lumen was pre-loaded with 0.70 µM VAN-HRP; and subsequently MN tips were brought in contact with 1 µL droplets of VAN ranging from 0.07-72.6 µM on a Parafilm-coated glass slide for 60 s, allowing the MN lumen to fill via capillary action (Figure 38C). VAN was incubated

inside the MN lumen for 10 min at room temperature, followed by washing the MN lumen with PBS (Figure 38D). As done previously in chapter 6, a 10 µL droplet of the TMB stock solution was placed on the MN base and a suction-flow of 10 nL s^{-1} was established through the MN and the waveguide to conduct the TMB assay in the biosensor (Figure 38E and F). During the TMB assay, the HRP enzyme converts the TMB solution to a colored end-product in a time-dependent manner, as shown in Figure 39C and D. The increase in the absorbance of the TMB end-product due to increasing concentration of VAN-HRP during the TMB assay was continuously monitored by the biosensor (shown in Figure 39C). A steady state (i.e., plateau of the AU vs. time plot) was reached for most concentration levels of VAN-HRP after 150-200 s from the start of the TMB reaction. Absorbance values at 200 ± 5 s were used for further evaluations, including to establish calibration curves (Figure 39A), as this window presented the best linearity of the calibration curve for the given biosensing parameters (i.e., TMB solution flow rate and TMB reagent concentrations).

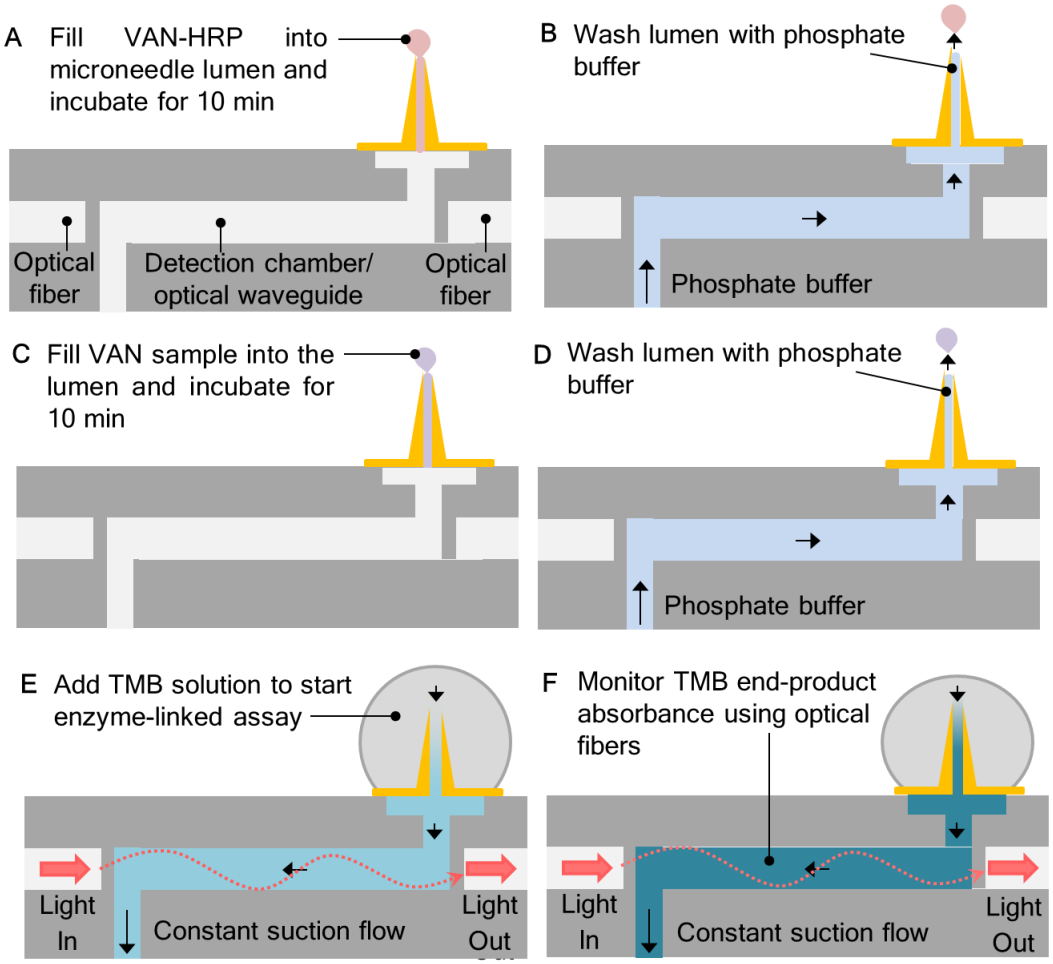

Figure 38. Process of conducting the biosensing process in the microneedle-optofluidic device. Microneedle lumens were pre-loaded with vancomycin-HRP before binding the vancomycin in an unknown sample. The enzyme-linked TMB assay was used to quantify the remaining vancomycin-HRP in the microneedle lumen surface.

7.2. Results

7.2.1. Vancomycin Binding Assay on Microneedle Base Surface

The absorbance measurements of a TMB assay (data provided in absorbance units (AU)) following VAN-HRP binding to AcKAA immobilized on the MN base surfaces followed a sigmoidal curve over a concentration range from 0.02 to 2.20 μM (Figure 39A).

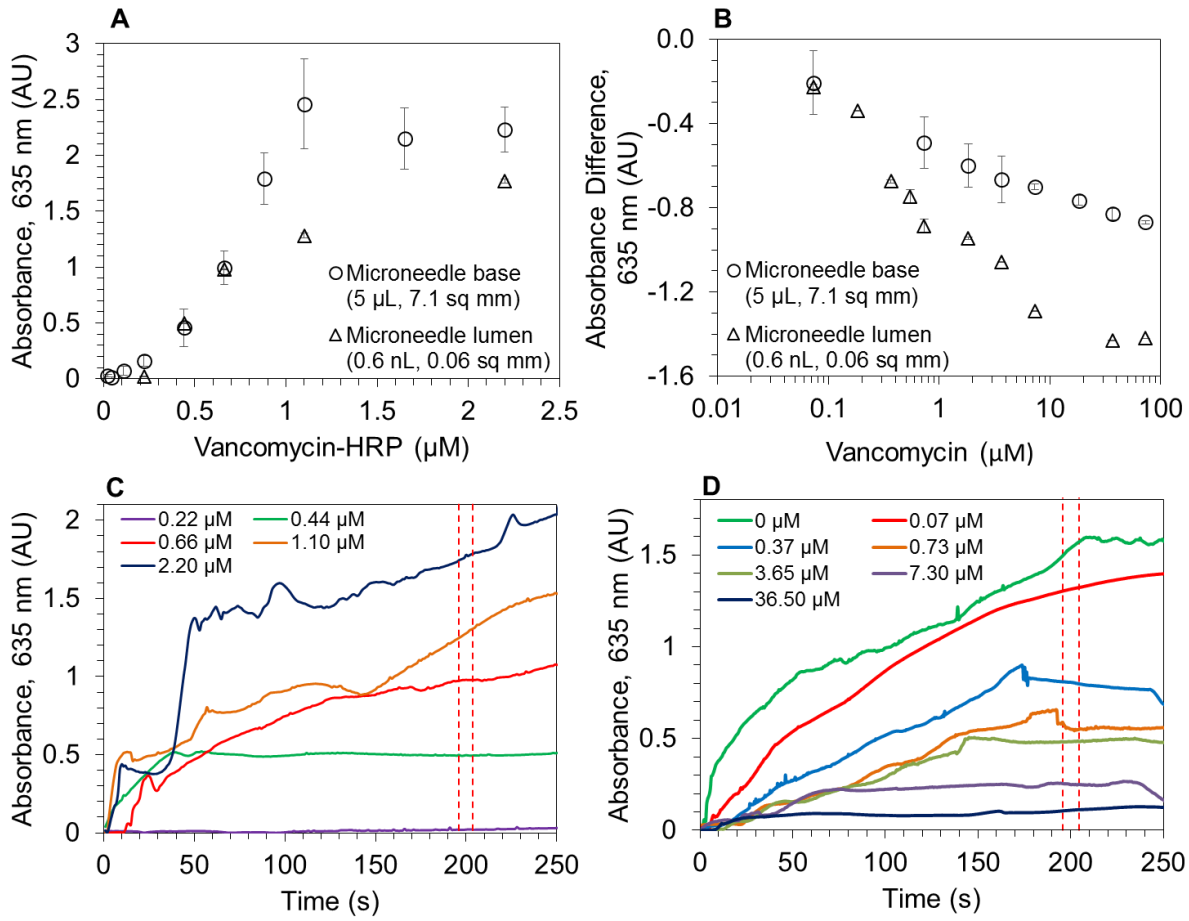

Figure 39. Detection of vancomycin in microliter-to-sub nanoliter volumes in the microneedle-optofluidic biosensor. The vancomycin detection scheme was initially tested on microneedle bases to verify the functionality, prior to transferring to microneedle lumens in the optofluidic device. VAN-HRP binding curve to the microneedle base (5 μL volume, 7.1 mm^2 area; absorbance measured by NanoDrop ND-1000) and microneedle lumen (0.6 nL volume, 0.06 mm^2 area; measured by the biosensor from absorbance between 196-205 s from Figure 39C) (A); Vancomycin competitive binding curve to VAN-HRP pre-loaded microneedle base (5 μL volume, 7.1 mm^2 area; absorbance measured by NanoDrop ND-1000) and microneedle lumen (0.6 nL volume, 0.06 mm^2 area; measured by the biosensor from absorbance between 196-205 s from Figure 39D) constructed on a semi-log plot (B); absorbance measured with the TMB assay for concentration-dependent VAN-HRP binding to the microneedle-lumen (C) and concentration-dependent competitive vancomycin binding to VAN-HRP pre-loaded microneedle lumen (D) over time ; (n=10; error bars represent standard deviations). The reference was normalized to have the maximum absorbance for a concentration of 0 μM vancomycin; hence, increasing the concentration of vancomycin reduced the absorbance in an inverted absorbance sensor (B).

Strictly monotonic behavior was observed over the range 0.11-1.10 µM VAN-HRP (5-50 µg mL^{-1}; R^2=0.98), with an average sensitivity of 2.7 AU $µM^{-1}$ VAN-HRP. Based on the near-linear range in Figure 39A, the concentration 0.70 µM VAN-HRP was selected for pre-loading the MN base for competitive binding with VAN.

The VAN-HRP pre-loaded MN bases were exposed 10 minutes to VAN concentration in the range from 0.07 to 72.6 µM (corresponding to a 0.1-100 molar ratio of VAN: VAN-HRP) for competitive binding. The remaining VAN-HRP bound to the surface was quantified using the TMB assay, as shown in Figure 39B. The semi-log linear detection range for VAN is 0.24-72.6 µM with a detection sensitivity of -0.16 AU/decade VAN concentration. The LoD (calculated as three times the blank standard deviation divided by the sensitivity) were determined to be 0.24 µM, using the standard deviation of the blank sample (± 0.01 AU; no VAN; only 0.70 µM VAN-HRP present in sample).

7.2.2. Competitive Vancomycin Binding Assay in Extremely Low Volume Microneedle Lumens

Biosensing tests using the MN-OFD biosensor were conducted according to Figure 38, where the analyte solutions - by capillary action - were brought in contact with the MN lumen only. A concentration dependent linear increase in binding levels from 0.22-0.70 µM VAN-HRP (R^2 = 0.98) was observed in the MN lumens. The sensitivity of the MN-OFD sensor to detect a change in the VAN-HRP concentration was 2.2 AU $µM^{-1}$ VAN-HRP. Based on the linear detection range, a VAN-HRP concentration of 0.70 µM was again selected for pre-loading the MN lumen to achieve a maximum absorbance of ~ 1 AU from VAN-HRP inside the MN lumen without competitive binding with VAN.

VAN in a concentration range from 0.07 to 72.6 μM (corresponding to a 0.1-100 molar ratio of VAN: VAN-HRP) was competitively bound to VAN-HRP pre-loaded MN lumen surfaces by capillary action (pulling ~0.6 nL volume into the lumen), simulating the MN behavior in therapeutic applications. The TMB signal decreased for increasing VAN concentrations as shown in Figure 39B and D following the competitive binding of VAN to the AcKAA peptide inside the MN lumen (analyte volume < 1 nL) by displacing VAN-HRP. Extrapolating from the linear region of the sigmoidal curve in a semi-logarithmic plot in Figure 39B, a VAN detection range from 0.3-40 μM was determined with a higher VAN detection sensitivity of 0.41 ± 0.03 AU/decade VAN and lower LoD of 84 nM VAN (calculated as done in section 6.2.1), compared to MN base surfaces.

7.3. Discussion

MN-integrated OFD biosensors have an immense potential to tackle most of the challenges that face TDM in one convenient and compact package. In clinical use, the device in this study would eliminate the need for conventional blood-draws using hypodermic needles in TDM patients. At the moment, this device would work directly for TDM drugs that have recently been shown to have a direct correlation between blood and ISF concentration, such as vancomycin, mycophenolate, phenobarbital, methotrexate, and theophylline [23]. By extracting ISF present in the skin, many TDM drugs could be directly analyzed in minimally-invasive and painless procedures with hollow MN insertions into the skin and binding the drug inside the MN lumens. This is expected to significantly improve patient compliance, speed up TDM, and eliminate anxiety and pain. Furthermore, point of care approaches can be easily envisioned that are user-friendly and

avoid the use of complex lab equipment to perform TDM, minimize the amount of reagents, and are very user-friendly.

The OFD sensing device was optimized to directly perform absorbance measurements of the TMB end-product after exiting the MN lumen towards the optical waveguide. The system was specifically designed for the extremely low volume reaction conducted directly inside the MN lumen (0.6 nL volume, 0.06 mm^2 area), where conventional laboratory tools that are used in TDM, such as bench-top spectrophotometers, do not provide sufficient detection and analytical capabilities. The optical detection chamber dimensions were optimized to obtain sufficient light absorbance for the typical high-concentrated TMB end-product (>1 AU). Channel lengths shorter than 5 mm result in lower absorbance values than 1 AU (resulting in lower detection sensitivity). Channel lengths greater than 5 mm deviated from linearity in the calibration curve for absorbance versus channel length due to loss of light from the system. During optical sensing in the selected channel, light was confined in the detection chamber of the OFD device as it was designed to simultaneously behave as a waveguide [152].

The gold coating of the MN surfaces allowed thiol-based functionalization with “ligands” that can trap various target molecules by both direct and competitive binding schemes. The VAN trapping and detection scheme described in Figure 36 involved a combination of chemo-selective gold-thiol surface modification, and high-affinity Sav-biotin binding to immobilize and stabilize biotinylated AcKAA ligands on the MN surface that attracted VAN. Compared to the expensive antibody-based methods of VAN detection performed in clinical settings, including the VANC Flex® cartridge, QMS® VANCO, and Emit® 2000 assay kits, the protocol presented herein was designed

with consideration to cost and stability of the surfaces, while maintaining appropriate binding characteristics (i.e., high binding affinity). The compounds used for surface functionalization of MN lumens provides flexibility to modify the surface chemistries based on the target-drug candidate, while being low-cost, robust, and stable during long-term storage. Further, the use of a VAN-HRP conjugate for competitively binding the AcKAA ligands on the MNs allowed for a simple enzyme-linked TMB assay to be used to quantify VAN in the analyte. Similarly, the availability of other peptide/drug candidates with HRP conjugates, such as gentamycin-HRP, makes the proposed biosensing system a platform technology to be used for TDM of a multitude of drug candidates.

The biotin-AcKAA immobilized surface for VAN binding was protected from non-specific binding of analyte and other compounds by a simple BSA treatment (1 mg mL^{-1} BSA for 30 min), which reduced non-specific binding of VAN-HRP on the MN base surface significantly (Figure 41B in page 173). MN surfaces functionalized with only PEG-biotin/Sav observed a high degree of non-specific binding of VAN-HRP (0.7 μM) with 0.62 ± 0.05 AU, which was reduced by the BSA treatment (0.04 ± 0.02 AU). Similarly, in the absence of BSA, VAN-HRP (at 0.70 μM) bound to the AcKAA-functionalized surface yielded a TMB end-product absorbance of 1.58 ± 0.28 AU, which decreased to 1.00 ± 0.43 AU in the presence of BSA-protection on the surface. Further, MN surfaces that were not functionalized with biotin-AcKAA, but were instead functionalized with biotin-BSA show strong prevention of VAN-HRP binding (0.04 ± 0.02 AU). Other surface protection strategies explored less successfully to limit non-specific binding of VAN-HRP on the surface included binding BSA prior to biotin-AcKAA immobilization and using caseins instead of BSA.

Vancomycin in the VAN-HRP conjugate was initially bound to the AcKAA peptide on large MN base surfaces to test the binding behavior. The resulting sigmoidal curve (Figure 39A) was explicable by the relatively low affinity binding between VAN-HRP and AcKAA peptide (1-100 µM affinity [153]). Pre-loading of VAN-HRP (0.70 µM) onto MN base surfaces was performed in a reproducible process to obtain 1.0 ± 0.2 AU during the TMB assay (n=5). This reproducibility was an important prerequisite to demonstrate the accuracy in quantifying the dynamic displacement of VAN-HRP by unlabelled VAN. According to Kiang et al. [23], VAN concentration in the ISF can vary between 3.2-32 µg mL^{-1} (2.2-22 µM) from peak to trough concentrations, which was accommodated by the linear dynamic range for competitive binding of VAN on MN bases above the detection limit presented in Figure 39B **(**0.24-72.6 µM). The outcome of the competitive VAN binding tests to the MN base (7.1 mm^2 area, 5 µL analyte volume) supported the use of the MN lumen only (0.06 mm^2, 0.6 nL volume) to perform VAN binding and detection.

Analyzing the drug in the MN lumen only has advantages over using the MN base. The VAN-HRP binding curve to the MN lumen was similar to the curve for the MN base (Figure 39A), but the LoD for VAN-HRP was significantly improved for the MN lumen compared to the MN base. A larger linear VAN-HRP binding range but lower sensitivity was obtained for the MN base compared to the MN lumen, due to the higher number of AcKAA peptide moieties on the larger MN base surface. The highest concentration of VAN-HRP that binds to the ligands inside the MN lumen before saturation (0.70 µM VAN-HRP) was used for pre-loading, which resulted in a TMB end-product absorbance of 0.98 ± 0.002 AU (similar to the MN base). In the MN lumen, VAN displaced VAN-HRP from the ligands at a significantly higher sensitivity (0.41 AU per decade

VAN concentration) compared to the MN base (0.16 AU per decade VAN concentration), as shown in Figure 39B. This increase in sensitivity inside the MN lumen was due to lower number of ligands present in the small surface area of 0.06 mm^2, where every displacement of a VAN-HRP from the surface had a significant impact on the resulting concentration of the TMB end-product. Because of the small area inside the MN lumen, the linear VAN detection range decreased from 0.7-72.6 µM (7.1 mm^2) to 0.3-40 µM (0.06 mm^2), but it could still accommodate the clinically relevant VAN detection range. The LoD for VAN in the MN lumen (84 nM VAN) was significantly lower than the MN base, and was the lowest value reported to date. Further, using capillary action to fill MN lumens with VAN-HRP and VAN ensured that the analyte sample volumes were repeatable, remain solely inside the lumen, and did not come in contact with the MN base surface, which could be verified by visual inspection from the backside of the MN base.

In comparison, the commercially-available and clinically-used QMS® VANCO assay kit provided a VAN detection range of 1.35-67.3 µM with a sensitivity of 0.77 AU μM^{-1} and a LoD of 1.35 µM; while the Emit® 2000 kit provided a detection range of 1.35-34 µM with a sensitivity of 0.70 AU μM^{-1} and a LoD of 1.35 µM. Both assay kits required 50-100 µL of blood/serum for analysis, but yielded significantly higher LoD compared to the MN-OFD device. With the LoD being orders of magnitude lower than the clinically relevant detection range for VAN and the LoD of other commercial assay kits, the performance of the MN-OFD device was highly superior to currently used methods for TDM.

The potential of the OFD sensing unit to provide real-time rapid detection of surface bound VAN-HRP at high sensitivity by measuring the absorbance of less than 40 nL of the TMB end-product

at a time using optical fibers (volume capacity of the optical waveguide is 40 nL; experiments performed at a constant flowrate of 10 nL s^{-1}) was shown in Figure 39. In conventional TMB assay protocols performed using bench-top spectrometers, the TMB reaction is allowed to develop the colored end-product for more than 10 min [154]. Due to the small diffusion distances between the TMB reactants and the HRP inside the MN lumen, the color development occurred significantly faster to reach saturation (under 200 s for all VAN-HRP concentrations). With a high optical SNR between 42.6-59.4 dB, the OFD biosensor provided reliable, reproducible, and accurate data during VAN detection and analysis. Features of the OFD sensing device, such as the possibility to change waveguide dimensions to improve sensitivity and LoD, added to the flexibility and adaptability of this platform sensing technology. Finally, the ability of MNs to collect extremely low volumes of ISF inside their lumens directly, the lack of need for analyte transfer from the collection site to testing site, and the lack of need for microscopes or other sophisticated lab equipment for analysis makes this biosensing platform very portable and easy to use in TDM.

7.4. Conclusions

This integrated MN-OFD biosensor for medical applications used surface functionalized gold-coated hollow MNs. It allowed the immobilization of ligands on the inner lumen surface that attract specific drug candidates present in a sub-nanoliter analyte volume. The enzyme assay combined with the OFD sensing system for vancomycin detection provided high sensitivity (0.41 AU/decade) and low LoD (84 nM) in clinically relevant ranges (from 0.3-40 µM), for extremely low volume (0.6 nL), and rapid measurements (<5 min in total) of drug binding levels to MNs. Using vancomycin as a target drug, the potential of the MN-OFD biosensor for TDM in ISF was demonstrated for point of care applications using a minimally invasive sample extraction and

limited needs for external equipment (only a diode laser and a photodetector were required). These results demonstrated the potential of the proposed integrated sensors for the development of portable devices that can be used by patients to perform TDM with many drug candidates present in ISF.

8. SUMMARY AND FUTURE WORK

8.1. Summary

This dissertation presented research and development towards understanding the mechanical performance of hollow MNs, evaluating their ID fluid delivery potential, and developing a powerful hollow MN-based TDM platform.

A comprehensive side-by-side micromechanical comparison between human and porcine skins showed that there were significant differences between the two skin types during microindentation and MN insertion. It also provided insight into structural differences affecting the mechanical properties between human and porcine skins, as well as the degradation of the skin due to freezing for preservation purposes. An artificial mechanical skin model was successfully developed and validated based on the mechanical properties of human skin that can be readily and cost-effectively manufactured for testing and quality control of MN technologies. The validated skin model can be effectively used in determining the appropriate MN insertion protocols that can be introduced to MN applicators and auto-injectors. The artificial skin model was used with a spring-loaded MN applicator to determine that MN insertion is a dynamic process, where the total energy of the applicator system, velocity of impact, microneedle tip area, and number of projections in an array significantly affect the force and energy required to insert MNs. These findings provide significant input into the design and development of MN applicator devices that can be used for self-administration of MN technologies.

Hollow MN devices integrated with spring-loaded MN applicators and syringes demonstrated their ability to accurately inject fluids intradermally at greater than 90% volume delivered into the skin. The novel methodology involving $^{99m}TcO_4^-$ injections led to extremely sensitive measurements of injection dose accuracy at sub-nanoliter resolution, which allowed evaluating the injection performance of ID delivery devices.

Finally, a novel MN-biosensor platform capable of collecting, binding, and detecting TDM drugs, such as Vancomycin, demonstrated high sensitivity detection at low limit of detection using extremely low sample volumes. Further developments of this MN-biosensing system can potentially revolutionize point-of-care TDM applications.

8.2. Future Work

Several aspects of the hollow MN technology presented herein can be improved in the future to facilitate the growth of MN applications.

8.2.1. Improvements to the Artificial Skin Model

Though the current AMSM developed in chapter 3 is only a mechanical simulant of skin, it is possible to customize the AMSM further for specific applications in transdermal drug delivery. For example, the epidermal/dermal layers of the AMSM can be constructed with porous materials modelled based on their mechanical properties and diffusion coefficients for transdermal drug-diffusion and fluid extraction studies. As such, the AMSM could be used as a representative model tissue for optimization of ID drug delivery systems. Long term studies of MN patches with continuous or discontinuous delivery of drugs and under varying stress conditions (i.e., flexing of the patch-ASMS system) could be simulated to allow a better understanding of long-term

efficiency of such devices. Further, adding simulants of the underlying tissue layers (subcutaneous fat and muscle) to the AMSM can help optimize MN insertion protocols based on the area of MN application (areas with different muscle tone and fat deposition).

8.2.2. Optimizing Microneedle Design and Insertion

Using the setup developed in chapter 4, a more extensive and comprehensive assessment of the factors influencing MN insertions can be conducted. Factors that can be evaluated include MN tip shape and bevel, tip sharpness, MN taper angle (or base diameter to tip diameter ratio), MN height, distance between each projection in an array, and more. Once the MN geometries are optimized, the insertion protocol can be optimized to ensure repeatability in MN insertion with minimal force requirements for rupturing the SC layer of skin.

8.2.3. Optimize Intradermal Delivery Using Hollow Microneedles

Many of the factors affecting successful fluid delivery using hollow MNs are still unknown. A comprehensive study aiming to evaluate these factors, including pressure and flow rate required to inject fluid into the ID space, will be beneficial for designing auto-injectors for hollow MNs. The work presented in 4 and 5 will be useful in designing such a study.

8.2.4. Clinical Assessment of Intradermal Delivery Using Microneedles

With optimized MN geometries, insertion protocols, and a thorough understanding of what leads to successful ID delivery of fluids, the MNs can be assessed pre-clinically and clinically for *in vivo* performance with various drug candidates, such as vaccines, that can potentially have elevated biological responses when delivered ID. Evidence showing superior performance of vaccines and

therapeutics when delivered ID exists. Using the hollow MN technology presented here will make the injection simpler and might improve the pharmacokinetic profiles of many drugs and vaccines.

8.2.5. Clinical Assessment of the Microneedle-Optofluidic Biosensing System

The MN-OFD biosensing system developed in 6 and 7 should be evaluated in pre-clinical and clinical studies to validate the technology. With *in vitro* validation of its performance for detecting Vancomycin using a competitive binding assay, the system can be prepared for *in vivo* evaluations in a small animal model treated intravenously with VAN. The biosensor will collect dermal ISF after application, which can be evaluated rapidly for the bound VAN concentration.

The MN-OFD biosensor can also be modified to bind and detect other TDM drugs that show a good correlation between blood and ISF concentrations. The relevant TDM drugs include mycophenolate mofetil, phenobarbital, methotrexate, theophylline, and cisplatin [23]. Furthermore, given that the hollow MNs are metallic, they can also be used in amperometric biosensing applications.

A tremendous amount of work has been done to date, exploring methodologies to utilize MNs for minimally-invasive biosensing. With predominant benefits of painless insertions, ability to extract ISF, presence of many biomolecules in ISF, and already identified correlations between ISF and blood for some biomolecules, MN-integrated biosensing devices have the potential to revolutionize diagnostics and TDM.

REFERENCES

[1] A. M. van der Aar, R. de Groot, M. Sanchez-Hernandez, E. W. Taanman, R. A. van Lier, M. B. Teunissen, E. C. de Jong, and M. L. Kapsenberg, "Cutting edge: Virus selectively primes human langerhans cells for CD70 expression promoting CD8+ T cell responses," *The Journal of Immunology,* vol. 187, pp. 3488-3492, 2011.

[2] I. Encyclopedia Britannica. (2010). *Sebaceous gland: Human skin cross section* [Web]. Available: http://kids.britannica.com/comptons/art-120217/Two-of-the-exocrine-glands-within-human-skin-are-sweat

[3] T. W. Prow, J. E. Grice, L. L. Lin, R. Faye, M. Butler, W. Becker, E. M. Wurm, C. Yoong, T. A. Robertson, and H. P. Soyer, "Nanoparticles and microparticles for skin drug delivery," *Advanced Drug Delivery Reviews,* vol. 63, pp. 470-491, 2011.

[4] M. R. Prausnitz, S. Mitragotri, and R. Langer, "Current status and future potential of transdermal drug delivery," *Nature Reviews Drug Discovery,* vol. 3, pp. 115-124, 2004.

[5] S. Al-Zahrani, M. Zaric, C. McCrudden, C. Scott, A. Kissenpfennig, and R. F. Donnelly, "Microneedle-mediated vaccine delivery: Harnessing cutaneous immunobiology to improve efficacy," *Expert Opinion on Drug Delivery,* vol. 9, pp. 541-550, 2012.

[6] S. M. Bal, Z. Ding, G. F. A. Kersten, W. Jiskoot, and J. A. Bouwstra, "Microneedle-based transcutaneous immunisation in mice with n-trimethyl chitosan adjuvanted diphtheria toxoid formulations," *Pharmaceutical Research,* vol. 27, pp. 1837-1847, 2010.

[7] M. Han, D. K. Kim, S. H. Kang, H. R. Yoon, B. Y. Kim, S. S. Lee, K. D. Kim, and H. G. Lee, "Improvement in antigen-delivery using fabrication of a grooves-embedded microneedle array," *Sensors and Actuators B: Chemical,* vol. 137, pp. 274-280, 2009.

[8] A. Kumar, X. Li, M. A. Sandoval, B. L. Rodriguez, B. R. Sloat, and Z. Cui, "Permeation of antigen protein-conjugated nanoparticles and live bacteria through microneedle-treated mouse skin," *International Journal of Nanomedicine,* vol. 6, p. 1253, 2011.

[9] D. V. McAllister, M. G. Allen, and M. R. Prausnitz, "Microfabricated microneedles for gene and drug delivery," *Annual Review of Biomedical Engineering,* vol. 2, pp. 289-313, 2000.

[10] M. Pearton, C. Allender, K. Brain, A. Anstey, C. Gateley, N. Wilke, A. Morrissey, and J. Birchall, "Gene delivery to the epidermal cells of human skin explants using microfabricated microneedles and hydrogel formulations," *Pharmaceutical Research,* vol. 25, pp. 407-416, 2008.

[11] M. R. Prausnitz, "Microneedles for transdermal drug delivery," *Advanced Drug Delivery Reviews,* vol. 56, pp. 581-587, 2004.

[12] S. P. Sullivan, D. G. Koutsonanos, M. del Pilar Martin, J. W. Lee, V. Zarnitsyn, S. O. Choi, N. Murthy, R. W. Compans, I. Skountzou, and M. R. Prausnitz, "Dissolving polymer microneedle patches for influenza vaccination," *Nature Medicine,* vol. 16, pp. 915-920, 2010.

[13] S. Henry, D. V. McAllister, M. G. Allen, and M. R. Prausnitz, "Microfabricated microneedles: A novel approach to transdermal drug delivery," *Journal of Pharmaceutical Sciences,* vol. 87, pp. 922-925, 1998.

[14] B. Stoeber and D. Liepmann, "Arrays of hollow out-of-plane microneedles for drug delivery," *Journal of Microelectromechanical Systems,* vol. 14, pp. 472-479, 2005.

[15] J. D. Zahn, N. H. Talbot, D. Liepmann, and A. P. Pisano, "Microfabricated polysilicon microneedles for minimally invasive biomedical devices," *Biomedical Microdevices,* vol. 2, pp. 295-303, 2000.

[16] I. Mansoor, Y. Liu, U. Häfeli, and B. Stoeber, "Arrays of hollow out-of-plane microneedles made by metal electrodeposition onto solvent cast conductive polymer structures," *Journal of Micromechanics and Microengineering,* vol. 23, p. 085011, 2013.

[17] R. F. Donnelly, T. R. R. Singh, and A. D. Woolfson, "Microneedle-based drug delivery systems: Microfabrication, drug delivery, and safety," *Drug Delivery,* vol. 17, pp. 187-207, 2010.

[18] I. Mansoor, U. O. Hafeli, and B. Stoeber, "Hollow out-of-plane polymer microneedles made by solvent casting for transdermal drug delivery," *Journal of Microelectromechanical Systems,* vol. 21, pp. 44-52, 2012.

[19] J.-H. Park, M. G. Allen, and M. R. Prausnitz, "Biodegradable polymer microneedles: Fabrication, mechanics and transdermal drug delivery," *Journal of Controlled Release,* vol. 104, pp. 51-66, 2005.

[20] W. Groenendaal, G. von Basum, K. A. Schmidt, P. A. Hilbers, and N. A. van Riel, "Quantifying the composition of human skin for glucose sensor development," *Journal of Diabetes Science and Technology,* vol. 4, pp. 1032-1040, 2010.

[21] U. O. Häfeli, M. H. Ensom, T. K. Kiang, B. Stoeber, B. A. Chua, M. Pudek, and V. Schmitt, "Comparison of vancomycin concentrations in blood and interstitial fluid: A possible model for less invasive therapeutic drug monitoring," *Clinical Chemistry and Laboratory Medicine,* vol. 49, pp. 2123-2125, 2011.

[22] T. K. Kiang, U. O. Häfeli, and M. H. Ensom, "A comprehensive review on the pharmacokinetics of antibiotics in interstitial fluid spaces in humans: Implications on

dosing and clinical pharmacokinetic monitoring," *Clinical Pharmacokinetics,* vol. 53, pp. 695-730, 2014.

[23] T. K. Kiang, V. Schmitt, M. H. Ensom, B. Chua, and U. O. Häfeli, "Therapeutic drug monitoring in interstitial fluid: A feasibility study using a comprehensive panel of drugs," *Journal of Pharmaceutical Sciences,* vol. 101, pp. 4642-4652, 2012.

[24] R. H. Champion, J. L. Burton, D. A. Burns, and S. M. Breathnach, *Textbook of dermatology*. London, UK: Blackwell Science, 1998.

[25] A. Arora, M. R. Prausnitz, and S. Mitragotri, "Micro-scale devices for transdermal drug delivery," *International Journal of Pharmaceutics,* vol. 364, pp. 227-236, 2008.

[26] E. Mukerjee, S. Collins, R. Isseroff, and R. Smith, "Microneedle array for transdermal biological fluid extraction and in situ analysis," *Sensors and Actuators A: Physical,* vol. 114, pp. 267-275, 2004.

[27] E. W. Smith and H. I. Maibach, *Percutaneous penetration enhancers*: CRC Press, 1995.

[28] S. P. Davis, W. Martanto, M. G. Allen, and M. R. Prausnitz, "Hollow metal microneedles for insulin delivery to diabetic rats," *Biomedical Engineering, IEEE Transactions,* vol. 52, pp. 909-915, 2005.

[29] M. Niraj, H. Gupta, S. Varshney, S. Pandey, and S. Singh, "Sensors for diabetes: Glucose biosensors by using different newer techniques: A review," *International Journal of Therapeutic Applications,* vol. 6, pp. 28-37, 2012.

[30] M. K. Haleyur Giri Setty and I. K. Hewlett, "Point of care technologies for hiv," *AIDS Research and Treatment,* vol. 2014, 2014.

[31] A. A. P. Ferreira, A. V. Benedetti, C. V. Uliana, C. S. Fugivara, G. P. dos Santos, H. Yamanaka, M. V. Foguel, M. de Souza Castilho, and N. C. Pesquero, *Amperometric biosensor for diagnosis of disease*: INTECH Open Access Publisher, 2013.

[32] E. B. Bahadır and M. K. Sezgintürk, "Applications of electrochemical immunosensors for early clinical diagnostics," *Talanta,* vol. 132, pp. 162-174, 2015.

[33] E. B. Bahadır and M. K. Sezgintürk, "Applications of commercial biosensors in clinical, food, environmental, and biothreat/biowarfare analyses," *Analytical Biochemistry,* vol. 478, pp. 107-120, 2015.

[34] D. Touw, C. Neef, A. Thomson, and A. Vinks, "Cost-effectiveness of therapeutic drug monitoring: A systematic review," *Therapeutic Drug Monitoring,* vol. 27, pp. 10-17, 2005.

[35] S.-W. Kim, "Therapeutic drug monitoring (tdm) of antimicrobial agents," *Infection and Chemotherapy,* vol. 40, pp. 133-139, 2008.

[36] D. C. Klonoff, "Continuous glucose monitoring roadmap for 21st century diabetes therapy," *Diabetes Care,* vol. 28, pp. 1231-1239, 2005.

[37] D. H. Keum, H. S. Jung, T. Wang, M. H. Shin, Y. E. Kim, K. H. Kim, G. Ahn, and S. K. Hahn, "Microneedle biosensor for real-time electrical detection of nitric oxide for in situ cancer diagnosis during endomicroscopy," *Advanced Healthcare Materials,* vol. 4, pp. 1153-1158, 2015.

[38] S. R. Corrie, G. J. Fernando, M. L. Crichton, M. E. Brunck, C. D. Anderson, and M. A. Kendall, "Surface-modified microprojection arrays for intradermal biomarker capture, with low non-specific protein binding," *Lab on a Chip,* vol. 10, pp. 2655-2658, 2010.

[39] P. R. Miller, S. A. Skoog, T. L. Edwards, D. M. Lopez, D. R. Wheeler, D. C. Arango, X. Xiao, S. M. Brozik, J. Wang, and R. Polsky, "Multiplexed microneedle-based biosensor array for characterization of metabolic acidosis," *Talanta,* vol. 88, pp. 739-742, 2012.

[40] M. Marinova, C. Artusi, L. Brugnolo, G. Antonelli, M. Zaninotto, and M. Plebani, "Immunosuppressant therapeutic drug monitoring by lc-ms/ms: Workflow optimization through automated processing of whole blood samples," *Clinical Biochemistry,* vol. 46, pp. 1723-1727, 2013.

[41] S. Seemann and A. Reinhardt, "Blood sample collection from a peripheral catheter system compared with phlebotomy," *Journal of Infusion Nursing,* vol. 23, pp. 290-297, 2000.

[42] W. R. Jarvis, "Epidemiology, appropriateness, and cost of vancomycin use," *Clinical Infectious Diseases,* vol. 26, pp. 1200-1203, 1998.

[43] P. J. Loll, J. Kaplan, B. S. Selinsky, and P. H. Axelsen, "Vancomycin binding to low-affinity ligands: Delineating a minimum set of interactions necessary for high-affinity binding §," *Journal of Medicinal Chemistry,* vol. 42, pp. 4714-4719, 1999.

[44] W. Hierholzer, J. S. Garner, A. B. Adams, D. Craven, D. Fleming, S. Forlenza, M. Gilchrist, D. Goldmann, E. Larson, and C. Mayhall, "Recommendations for preventing the spread of vancomycin resistance: Recommendations of the hospital infection control practices advisory committee (hicpac)," *American Journal of Infection Control,* vol. 23, pp. 87-94, 1995.

[45] P. M. Wang, M. Cornwell, and M. R. Prausnitz, "Minimally invasive extraction of dermal interstitial fluid for glucose monitoring using microneedles," *Diabetes Technology and Therapeutics,* vol. 7, pp. 131-141, 2005.

[46] K. Sakaguchi, Y. Hirota, N. Hashimoto, W. Ogawa, T. Sato, S. Okada, K. Hagino, Y. Asakura, Y. Kikkawa, and J. Kojima, "A minimally invasive system for glucose area under the curve measurement using interstitial fluid extraction technology: Evaluation of the

accuracy and usefulness with oral glucose tolerance tests in subjects with and without diabetes," *Diabetes Technology and Therapeutics,* vol. 14, pp. 485-491, 2012.

[47] R. F. Donnelly, K. Mooney, E. Caffarel-Salvador, B. M. Torrisi, E. Eltayib, and J. C. McElnay, "Microneedle-mediated minimally invasive patient monitoring," *Therapeutic Drug Monitoring,* vol. 36, pp. 10-17, 2014.

[48] E. Caffarel-Salvador, A. J. Brady, E. Eltayib, T. Meng, A. Alonso-Vicente, P. Gonzalez-Vazquez, B. M. Torrisi, E. M. Vicente-Perez, K. Mooney, and D. S. Jones, "Hydrogel-forming microneedle arrays allow detection of drugs and glucose in vivo: Potential for use in diagnosis and therapeutic drug monitoring," *PloS One,* vol. 10, p. e0145644, 2015.

[49] A. V. Romanyuk, V. N. Zvezdin, P. Samant, M. I. Grenader, M. Zemlyanova, and M. R. Prausnitz, "Collection of analytes from microneedle patches," *Analytical Chemistry,* vol. 86, pp. 10520-10523, 2014.

[50] S. Zimmermann, D. Fienbork, A. W. Flounders, and D. Liepmann, "In-device enzyme immobilization: Wafer-level fabrication of an integrated glucose sensor," *Sensors and Actuators B: Chemical,* vol. 99, pp. 163-173, 2004.

[51] L. Strambini, A. Longo, S. Scarano, T. Prescimone, I. Palchetti, M. Minunni, D. Giannessi, and G. Barillaro, "Self-powered microneedle-based biosensors for pain-free high-accuracy measurement of glycaemia in interstitial fluid," *Biosensors and Bioelectronics,* vol. 66, pp. 162-168, 2015.

[52] D. A. Muller, S. R. Corrie, J. Coffey, P. R. Young, and M. A. Kendall, "Surface modified microprojection arrays for the selective extraction of the dengue virus ns1 protein as a marker for disease," *Analytical Chemistry,* vol. 84, pp. 3262-3268, 2012.

[53] J. R. Windmiller, G. Valdés-Ramírez, N. Zhou, M. Zhou, P. R. Miller, C. Jin, S. M. Brozik, R. Polsky, E. Katz, and R. Narayan, "Bicomponent microneedle array biosensor for minimally-invasive glutamate monitoring," *Electroanalysis,* vol. 23, pp. 2302-2309, 2011.

[54] A. Jina, M. J. Tierney, J. A. Tamada, S. McGill, S. Desai, B. Chua, A. Chang, and M. Christiansen, "Design, development, and evaluation of a novel microneedle array-based continuous glucose monitor," *Journal of Diabetes Science and Technology,* vol. 8, pp. 483-487, 2014.

[55] B. Chua, S. P. Desai, M. J. Tierney, J. A. Tamada, and A. N. Jina, "Effect of microneedles shape on skin penetration and minimally invasive continuous glucose monitoring in vivo," *Sensors and Actuators A: Physical,* vol. 203, pp. 373-381, 2013.

[56] S. K. Garg, M. Voelmle, and P. A. Gottlieb, "Time lag characterization of two continuous glucose monitoring systems," *Diabetes Research and Clinical Practice,* vol. 87, pp. 348-353, 2010.

[57] L. P. O. Norlen, "The skin barrier — structure and physical function," Ph.D. dissertatoin, Karolinska Institute, Stockholm, Sweden, 1999.

[58] K. Subramanyan, M. Misra, S. Mukherjee, and K. P. Ananthapadmanabhan, "Advances in the materials science of skin: A composite structure with multiple functions," *MRS Bulletin,* vol. 32, 2007.

[59] M. H. Ross, W. Pawlina, and G. I. Kaye, *Histology : A text and atlas* vol. 4: Lippincott Williams & Wilkins, 2003.

[60] C. A. Brohem, L. B. da Silva Cardeal, M. Tiago, M. S. Soengas, S. B. de Moraes Barros, and S. S. Maria-Engler, "Artificial skin in perspective: Concepts and applications," *Pigment Cell and Melanoma Research,* vol. 24, pp. 35-50, 2011.

[61] G. Ajani, N. Sato, J. A. Mack, and E. V. Maytin, "Cellular responses to disruption of the permeability barrier in a three-dimensional organotypic epidermal model," *Experimental Cell Research,* vol. 313, pp. 3005-3015, 2007.

[62] W. Martanto, J. S. Moore, O. Kashlan, R. Kamath, P. M. Wang, J. M. O'Neal, and M. R. Prausnitz, "Microinfusion using hollow microneedles," *Pharmaceutical Research,* vol. 23, pp. 104-113, 2006.

[63] M. Balasubramani, T. R. Kumar, and M. Babu, "Skin substitutes: A review," *Burns,* vol. 27, pp. 534-544, 2001.

[64] R. Meijer, L. F. A. Douven, and C. W. J. Oomens, "Characterisation of anisotropic and non-linear behaviour of human skin in vivo," *Computer Methods in Biomechanics and Biomedical Engineering,* vol. 2, pp. 13-27, 1999.

[65] G. A. Holzapfel, "Biomechanics of soft tissue," *The handbook of materials behavior models,* vol. 3, pp. 1049-1063, 2001.

[66] P. A. Payne, "Measurement of properties and function of skin," *Clinical Physics and Physiological Measurement,* vol. 12, p. 105, 2000.

[67] N. Roxhed, T. C. Gasser, P. Griss, G. A. Holzapfel, and G. Stemme, "Penetration-enhanced ultrasharp microneedles and prediction on skin interaction for efficient transdermal drug delivery," *Journal of Microelectromechanical Systems,* vol. 16, pp. 1429-1440, 2007.

[68] R. H. Wildnauer, J. W. Bothwell, and A. B. Douglass, "Stratum corneum biomechanical properties i. Influence of relative humidity on normal and extracted human stratum corneum," *Journal of Investigative Dermatology,* vol. 56, pp. 72-78, 1971.

[69] F. M. Hendriks, D. Brokken, C. W. J. Oomens, D. L. Bader, and F. P. T. Baaijens, "The relative contributions of different skin layers to the mechanical behavior of human skin in

vivo using suction experiments," *Medical Engineering and Physics,* vol. 28, pp. 259-266, 2006.

[70] S. A. Ranamukhaarachchi, T. Schneider, S. Lehnert, L. Sprenger, J. R. Campbell, I. Mansoor, J. C. Y. Lai, K. Rai, J. Dutz, U. O. Häfeli, and B. Stoeber, "Development and validation of an artificial mechanical skin model for the study of interactions between skin and microneedles," *Macromolecular Materials and Engineering,* vol. 301, pp. 306-314, 2016.

[71] R. Dahlgren and W. Elsnau, "Measurement of skin condition by sonic velocity," *Journal of the Society of Cosmetic Chemists,* vol. 35, pp. 1-9, 1986.

[72] K. Koutroupi and J. Barbenel, "Mechanical and failure behaviour of the stratum corneum," *Journal of Biomechanics,* vol. 23, pp. 281-287, 1990.

[73] K. S. Wu, W. W. van Osdol, and R. H. Dauskardt, "Mechanical properties of human stratum corneum: Effects of temperature, hydration, and chemical treatment," *Biomaterials,* vol. 27, pp. 785-795, 2006.

[74] Y. Yuan and R. Verma, "Measuring microelastic properties of stratum corneum," *Colloids and Surfaces B: Biointerfaces,* vol. 48, pp. 6-12, 2006.

[75] C. Pailler-Mattei, S. Bec, and H. Zahouani, "In vivo measurements of the elastic mechanical properties of human skin by indentation tests," *Medical Engineering and Physics,* vol. 30, pp. 599-606, 2008.

[76] A. Delalleau, G. Josse, J.-M. Lagarde, H. Zahouani, and J.-M. Bergheau, "Characterization of the mechanical properties of skin by inverse analysis combined with the indentation test," *Journal of Biomechanics,* vol. 39, pp. 1603-1610, 2006.

[77] P. G. Agache, C. Monneur, J. L. Leveque, and J. Rigal, "Mechanical properties and young's modulus of human skin in vivo," *Archives of Dermatological Research,* vol. 269, pp. 221-232, 1980.

[78] R. Sanders, "Torsional elasticity of human skin in vivo," *Pflügers Archiv European Journal of Physiology,* vol. 342, pp. 255-260, 1973.

[79] J. F. M. Manschot and A. J. M. Brakkee, "The measurement and modelling of the mechanical properties of human skin in vivo—ii. The model," *Journal of Biomechanics,* vol. 19, pp. 517-521, 1986.

[80] P. F. F. Wijn, A. J. M. Brakkee, J. P. Kuiper, and A. J. H. Vendrik, "The alinear viscoelastic properties of human skin in vivo related to sex and age," *Bioengineering and the Skin,* p. 135, 1982.

[81] C. Escoffier, J. De Rigal, A. Rochefort, R. Vasselet, J.-L. Lévêque, and P. G. Agache, "Age-related mechanical properties of human skin: An in vivo study," *Journal of Investigative Dermatology,* vol. 93, pp. 353-357, 1989.

[82] O. A. Shergold and N. A. Fleck, "Mechanisms of deep penetration of soft solids, with application to the injection and wounding of skin," *Proceedings of the Royal Society of LondonSeries A: Mathematical, Physical and Engineering Sciences,* vol. 460, pp. 3037-3058, 2004.

[83] P. P. Purslow, "Measurement of the fracture toughness of extensible connective tissues," *Journal of Materials Science,* vol. 18, pp. 3591-3598, 1983.

[84] S. P. Davis, B. J. Landis, Z. H. Adams, M. G. Allen, and M. R. Prausnitz, "Insertion of microneedles into skin: Measurement and prediction of insertion force and needle fracture force," *Journal of Biomechanics,* vol. 37, pp. 1155-1163, 2004.

[85] O. A. Shergold and N. A. Fleck, "Experimental investigation into the deep penetration of soft solids by sharp and blunt punches, with application to the piercing of skin," *Transactions-American Society of Mechanical Engineers Journal of Biomechanical Engineering,* vol. 127, p. 838, 2005.

[86] P. Brett, T. Parker, A. Harrison, T. Thomas, and A. Carr, "Simulation of resistance forces acting on surgical needles," *Proceedings of the Institution of Mechanical Engineers, Part H: Journal of Engineering in Medicine,* vol. 211, pp. 335-347, 1997.

[87] P. O'Callaghan, M. Jones, D. James, S. Leadbeatter, C. Holt, and L. Nokes, "Dynamics of stab wounds: Force required for penetration of various cadaveric human tissues," *Forensic Science International,* vol. 104, pp. 173-178, 1999.

[88] S. Avon and R. Wood, "Porcine skin as an in vivo model for ageing of human bite marks," *Journal of Forensic Odontostomatology,* vol. 23, pp. 30-9, 2005.

[89] N. Vardaxis, T. Brans, M. Boon, R. Kreis, and L. Marres, "Confocal laser scanning microscopy of porcine skin: Implications for human wound healing studies," *Journal of Anatomy,* vol. 190, pp. 601-611, 1997.

[90] W. T. Humphries and R. H. Wildnauer, "Thermomechanical analysis of stratum corneum i. Technique," *Journal of Investigative Dermatology,* vol. 57, pp. 32-37, 1971.

[91] Y. S. Papir, K.-H. Hsu, and R. H. Wildnauer, "The mechanical properties of stratum corneum: I. The effect of water and ambient temperature on the tensile properties of newborn rat stratum corneum," *Biochimica et Biophysica Acta (BBA)-General Subjects,* vol. 399, pp. 170-180, 1975.

[92] A. N. Annaidh, M. Ottenio, K. Bruyère, M. Destrade, and M. Gilchrist, "Mechanical properties of excised human skin," in *6th World Congress of Biomechanics, August 1-6, 2010 Singapore*, pp. 1000-1003, 2010.

[93] M. Geerligs, "A literature review of the mechanical behaviour of the stratum corneum, the living epidermis and the subcutaneous fat tissue," *Technical Note PR-TN*, vol. 450, 2006.

[94] T. Foutz, E. Stone, and C. Abrams Jr, "Effects of freezing on mechanical properties of rat skin," *American Journal of Veterinary Research*, vol. 53, pp. 788-792, 1992.

[95] T. P. Sullivan, W. H. Eaglstein, S. C. Davis, and P. Mertz, "The pig as a model for human wound healing," *Wound Repair and Regeneration*, vol. 9, pp. 66-76, 2001.

[96] R. M. Lavker, G. Dong, P. Zheng, and G. F. Murphy, "Hairless micropig skin. A novel model for studies of cutaneous biology," *The American Journal of Pathology*, vol. 138, p. 687, 1991.

[97] C. L. Silva, D. Topgaard, V. Kocherbitov, J. Sousa, A. A. Pais, and E. Sparr, "Stratum corneum hydration: Phase transformations and mobility in stratum corneum, extracted lipids and isolated corneocytes," *Biochimica et Biophysica Acta (BBA)-Biomembranes*, vol. 1768, pp. 2647-2659, 2007.

[98] G. Gray and H. Yardley, "Lipid compositions of cells isolated from pig, human, and rat epidermis," *Journal of Lipid Research*, vol. 16, pp. 434-440, 1975.

[99] A. A. Gurjarpadhye, "Effect of localized mechanical indentation on skin water content evaluated using oct," *Journal of Biomedical Imaging*, vol. 2011, p. 17, 2011.

[100] L. M. Russell, S. Wiedersberg, and M. B. Delgado-Charro, "The determination of stratum corneum thickness an alternative approach," *European Journal of Pharmaceutics and Biopharmaceutics*, vol. 69, pp. 861-870, 2008.

[101] L. E. Berrutti, A. J. Singer, and S. A. McClain, "Histopathologic effects of cutaneous tape stripping in pigs," *Academic Emergency Medicine*, vol. 7, pp. 1349-1353, 2000.

[102] W. Meyer, R. Schwarz, and K. Neurand, "*The skin of domestic mammals as a model for the human skin, with special reference to the domestic pig*," Karger Publishers, pp. 39-52, 1978.

[103] G. Morris and J. Hopewell, "Epidermal cell kinetics of the pig: A review," *Cell Proliferation*, vol. 23, pp. 271-282, 1990.

[104] E.-J. Suh, Y.-A. Woo, and H.-J. Kim, "Determination of water content in skin by using a ft near infrared spectrometer," *Archives of Pharmacal Research*, vol. 28, pp. 458-462, 2005.

[105] M. S. Micozzi, "Experimental study of postmortem change under field conditions: Effects of freezing, thawing, and mechanical injury," *Journal of Forensic Sciences,* vol. 31, pp. 953-961, 1986.

[106] I. Mansoor, J. Lai, S. A. Ranamukhaarachchi, V. Schmitt, D. Lambert, J. Dutz, U. O. Häfeli, and B. Stoeber, "A microneedle-based method for the characterization of diffusion in skin tissue using doxorubicin as a model drug," *Biomedical Microdevices,* vol. 17, pp. 1-10, 2015.

[107] G. B. Kasting and L. A. Bowman, "Electrical analysis of fresh, excised human skin: A comparison with frozen skin," *Pharmaceutical Research,* vol. 7, pp. 1141-1146, 1990.

[108] P. M. Wang, M. Cornwell, J. Hill, and M. R. Prausnitz, "Precise microinjection into skin using hollow microneedles," *Journal of Investigative Dermatology,* vol. 126, pp. 1080-1087, 2006.

[109] J.-H. Park, M. G. Allen, and M. R. Prausnitz, "Polymer microneedles for controlled-release drug delivery," *Pharmaceutical Research,* vol. 23, pp. 1008-1019, 2006.

[110] P. Khanna, K. Luongo, J. A. Strom, and S. Bhansali, "Sharpening of hollow silicon microneedles to reduce skin penetration force," *Journal of Micromechanics and Microengineering,* vol. 20, p. 045011, 2010.

[111] O. Olatunji, D. B. Das, M. J. Garland, L. Belaid, and R. F. Donnelly, "Influence of array interspacing on the force required for successful microneedle skin penetration: Theoretical and practical approaches," *Journal of Pharmaceutical Sciences,* vol. 102, pp. 1209-1221, 2013.

[112] M. Yang and J. D. Zahn, "Microneedle insertion force reduction using vibratory actuation," *Biomedical Microdevices*, vol. 6, pp. 177-182, 2004.

[113] L. Leng, A. McAllister, B. Zhang, M. Radisic, and A. Guenther, "Mosaic hydrogels: Dynamic tessellation and coding of cells," in *Journal of Tissue Engineering and Regenerative Medicine*, pp. 370-370, 2012.

[114] A. Passot and G. Cabodevila, "Mechanical properties of an artificial vascularized human skin," in *SPIE Microtechnologies*, pp. 80680C-80680C-12, 2011.

[115] W. Koelmans, G. Krishnamoorthy, A. Heskamp, J. Wissink, S. Misra, and N. Tas, "Microneedle characterization using a double-layer skin simulant," *Mechanical Engineering Research,* vol. 3, p. p51, 2013.

[116] E. Larrañeta, J. Moore, E. M. Vicente-Pérez, P. González-Vázquez, R. Lutton, A. D. Woolfson, and R. F. Donnelly, "A proposed model membrane and test method for microneedle insertion studies," *International Journal of Pharmaceutics,* vol. 472, pp. 65-73, 2014.

[117] M. J. Garland, K. Migalska, T.-M. Tuan-Mahmood, T. R. R. Singh, R. Majithija, E. Caffarel-Salvador, C. M. McCrudden, H. O. McCarthy, A. D. Woolfson, and R. F. Donnelly, "Influence of skin model on in vitro performance of drug-loaded soluble microneedle arrays," *International Journal of Pharmaceutics,* vol. 434, pp. 80-89, 2012.

[118] D. Zhang, D. B. Das, and C. D. Rielly, "Microneedle assisted micro-particle delivery from gene guns: Experiments using skin-mimicking agarose gel," *Journal of Pharmaceutical Sciences,* vol. 103, pp. 613-627, 2014.

[119] D. Qin, Y. Xia, and G. M. Whitesides, "Soft lithography for micro-and nanoscale patterning," *Nature Protocols,* vol. 5, pp. 491-502, 2010.

[120] C. McCarthy, M. Hussey, and M. Gilchrist, "On the sharpness of straight edge blades in cutting soft solids: Part i–indentation experiments," *Engineering Fracture Mechanics,* vol. 74, pp. 2205-2224, 2007.

[121] P. E. Laurent, S. Bonnet, P. Alchas, P. Regolini, J. A. Mikszta, R. Pettis, and N. G. Harvey, "Evaluation of the clinical performance of a new intradermal vaccine administration technique and associated delivery system," *Vaccine,* vol. 25, pp. 8833-8842, 2007.

[122] L. B. Poppe, S. W. Savage, and S. F. Eckel, "Assessment of final product dosing accuracy when using volumetric technique in the preparation of chemotherapy," *Journal of Oncology Pharmacy Practice,* vol. 22, pp. 3-9, 2016.

[123] M. Krzywon, T. van der Burg, U. Fuhr, M. Schubert-Zsilavecz, and M. Abdel-Tawab, "Study on the dosing accuracy of commonly used disposable insulin pens," *Diabetes Technology and Therapeutics,* vol. 14, pp. 804-809, 2012.

[124] Y. Luijf and J. DeVries, "Dosing accuracy of insulin pens versus conventional syringes and vials," *Diabetes Technology and Therapeutics,* vol. 12, pp. S-73-S-77, 2010.

[125] P. Laurent, R. Pettis, W. Easterbrook, and J. Berube, "Evaluating new hypodermic and intradermal injection devices," *Medical Device Technology,* vol. 17, pp. 16-19, 2006.

[126] T. Asakura, H. Seino, M. Kageyama, and N. Yohkoh, "Dosing accuracy of two insulin pre-filled pens," *Current Medical Research and Opinion,* vol. 24, pp. 1429-1434, 2008.

[127] R. Alvarez-Román, A. Naik, Y. Kalia, H. Fessi, and R. H. Guy, "Visualization of skin penetration using confocal laser scanning microscopy," *European Journal of Pharmaceutics and Biopharmaceutics,* vol. 58, pp. 301-316, 2004.

[128] M. Schwarz, M. Omar, A. Buehler, J. Aguirre, and V. Ntziachristos, "Implications of ultrasound frequency in optoacoustic mesoscopy of the skin," *IEEE Transactions on Medical Imaging,* vol. 34, pp. 672-677, 2015.

[129] F. E. Pearson, C. L. McNeilly, M. L. Crichton, C. A. Primiero, S. R. Yukiko, G. J. Fernando, X. Chen, S. C. Gilbert, A. V. Hill, and M. A. Kendall, "Dry-coated live viral vector vaccines delivered by nanopatch microprojections retain long-term thermostability and induce transgene-specific T cell responses in mice," *PloS One,* vol. 8, p. e67888, 2013.

[130] A. M. Kligman and E. Christopers, "Preparation of isolated sheets of human stratum corneum," *Archives of Dermatology,* vol. 88, p. 702, 1963.

[131] A. Park and C. Baddiel, "Rheology of stratum corneum-i: A molecular interpretation of the stress-strain curve," *Journal of the Society of Cosmetic Chemists,* vol. 23, pp. 3-12, 1972.

[132] W. C. Oliver and G. M. Pharr, "Improved technique for determining hardness and elastic modulus using load and displacement sensing indentation experiments," *Journal of Materials Research,* vol. 7, pp. 1564-1583, 1992.

[133] M. Doerner, D. Gardner, and W. Nix, "Plastic properties of thin films on substrates as measured by submicron indentation hardness and substrate curvature techniques," *Journal of Materials Research,* vol. 1, pp. 845-851, 1986.

[134] X. Liu, J. Cleary, and G. German, "The global mechanical properties and multi-scale failure mechanics of heterogeneous human stratum corneum," *Acta Biomaterialia,* 2016.

[135] M. Haftek, S. Callejon, Y. Sandjeu, K. Padois, F. Falson, F. Pirot, P. Portes, F. Demarne, and V. Jannin, "Compartmentalization of the human stratum corneum by persistent tight junction-like structures," *Experimental Dermatology,* vol. 20, pp. 617-621, 2011.

[136] C. Harding, A. Watkinson, A. Rawlings, and I. Scott, "Dry skin, moisturization and corneodesmolysis," *International Journal of Cosmetic Science,* vol. 22, pp. 21-52, 2000.

[137] J. Bouwstra, G. Gooris, W. Bras, and D. Downing, "Lipid organization in pig stratum corneum," *Journal of Lipid Research,* vol. 36, pp. 685-695, 1995.

[138] J. A. Bouwstra, A. de Graaff, G. S. Gooris, J. Nijsse, J. W. Wiechers, and A. C. van Aelst, "Water distribution and related morphology in human stratum corneum at different hydration levels," *Journal of Investigative Dermatology,* vol. 120, pp. 750-758, 2003.

[139] G. Wilkes, A.-L. Nguyen, and R. Wildnauer, "Structure-property relations of human and neonatal rat stratum corneum i. Thermal stability of the crystalline lipid structure as studied by x-ray diffraction and differential thermal analysis," *Biochimica et Biophysica Acta (BBA)-General Subjects,* vol. 304, pp. 267-275, 1973.

[140] M. Liu, J. Sun, Y. Sun, C. Bock, and Q. Chen, "Thickness-dependent mechanical properties of polydimethylsiloxane membranes," *Journal of Micromechanics and Microengineering,* vol. 19, p. 035028, 2009.

[141] M. Geerligs, "Skin layer mechanics," Technische Universiteit Eindhoven, 2010.

[142] M. Heverly, P. Dupont, and J. Triedman, "Trajectory optimization for dynamic needle insertion," in *Proceedings of the 2005 IEEE International Conference on Robotics and Automation*, 2005, pp. 1646-1651.

[143] C. Mantoux, "L'intradermo-réaction a la tuberculine et son interprétation clinique," *Presse Medicale,* vol. 18, pp. 10-13, 1910.

[144] V. F. Achterberg, L. Buscemi, H. Diekmann, J. Smith-Clerc, H. Schwengler, J.-J. Meister, H. Wenck, S. Gallinat, and B. Hinz, "The nano-scale mechanical properties of the extracellular matrix regulate dermal fibroblast function," *Journal of Investigative Dermatology,* vol. 134, pp. 1862-1872, 2014.

[145] S. A. Ranamukhaarachchi, S. Lehnert, S. L. Ranamukhaarachchi, L. Sprenger, T. Schneider, I. Mansoor, K. Rai, U. Häfeli, and B. Stoeber, "A micromechanical comparison of human and porcine skin before and after preservation by freezing for medical device development," *Scientific Reports,* vol. 6, 2016.

[146] M. G. Stabin, R. B. Sparks, and E. Crowe, "Olinda/exm: The second-generation personal computer software for internal dose assessment in nuclear medicine," *Journal of Nuclear Medicine,* vol. 46, pp. 1023-1027, 2005.

[147] "Ionising radiation: Dose comparisons," P. H. England, Ed., 2011.

[148] F. Frederix, K. Bonroy, W. Laureyn, G. Reekmans, A. Campitelli, W. Dehaen, and G. Maes, "Enhanced performance of an affinity biosensor interface based on mixed self-assembled monolayers of thiols on gold," *Langmuir,* vol. 19, pp. 4351-4357, 2003.

[149] C. Canaria, J. Maloney, C. Yu, J. Smith, S. Fraser, and R. Lansford, "Formation of biotinylated alkylthiolate self-assembled monolayers on gold," *NSTI-Nanotech,* vol. 2, pp. 1-4, 2005.

[150] B. Zhu, T. Eurell, R. Gunawan, and D. Leckband, "Chain-length dependence of the protein and cell resistance of oligo (ethylene glycol)-terminated self-assembled monolayers on gold," *Journal of Biomedical Materials Research,* vol. 56, pp. 406-416, 2001.

[151] B. Samel, M. K. Chowdhury, and G. Stemme, "The fabrication of microfluidic structures by means of full-wafer adhesive bonding using a poly (dimethylsiloxane) catalyst," *Journal of Micromechanics and Microengineering,* vol. 17, p. 1710, 2007.

[152] V. J. Cadarso, C. Fernández-Sánchez, A. Llobera, M. Darder, and C. Domínguez, "Optical biosensor based on hollow integrated waveguides," *Analytical Chemistry,* vol. 80, pp. 3498-3501, 2008.

[153] N. Yao, C. Y. Wu, W. Xiao, and K. S. Lam, "Discovery of high-affinity peptide ligands for vancomycin," *Peptide Science,* vol. 90, pp. 421-432, 2008.

[154] C. Padeste and S. Neuhaus, *Polymer micro-and nanografting*: William Andrew, 2015.

APPENDICES

Appendix A – Statistical Data Supporting Chapter 2

To assess the differences between the mechanical properties of skin samples based on skin sources, skin state, RH conditions, and interactions thereof, student t-tests, ANOVA, and LSD were calculated according to the following equations.

The t-test was conducted to determine, using the t-statistic (*t*), significant differences between two groups of data, using group means (x_i), standard deviations (σ_i), and sample size (n_i):

$$t = \frac{x_1 - x_2}{\frac{\sigma_1}{\sqrt{n_1}} + \frac{\sigma_2}{\sqrt{n_2}}} \quad (14)$$

The *t* provides an indication of the separation of an estimated parameter from its population value or comparator value, and its standard error. The σ_i indicated the degree of deviation or spread in group of data points, per:

$$\sigma_i = \sqrt{\frac{\sum(x_i - X)^2}{n_i - 1}} \quad (15)$$

ANOVA was used to compare differences in means among more than two groups by looking at variation in the data and where variation is found. Sum of squares between groups (SSB) was calculated as follows, using overall population means (X):

$$SSB = n_1(x_1 - X)^2 + n_2(x_2 - X)^2 + n_3(x_3 - X)^2 \quad (16)$$

Similarly, sum of squares within groups (SSW) was calculated as follows:

$$SSW = \sigma_1^2(n_1 - 1) + \sigma_2^2(n_2 - 1) + \sigma_3^2(n_3 - 1) \qquad (17)$$

The F-ratio, a ratio of two variances indicating if the variation among group means is comparable to what is expected by chance, was calculated to determine the significance of each treatment:

$$F\ ratio = \frac{Mean\ SSB}{Mean\ SSW} \qquad (18)$$

The LSD was used to determine the threshold for statistical difference between means of groups. A difference between the means of two groups greater than the magnitude of the LSD indicated a statistically significant difference between the groups at a 95% confidence interval.

$$LSD_{1,2} = t_{0.05,.error\ df}\sqrt{MSSW\ (\frac{1}{n_1} + \frac{1}{n_2})} \qquad (19)$$

The following tables provide an anatomical/compositional comparison between human and porcine skins; the ANOVA from microindentation and MN insertion profiling; and further information on statistically significant interactions of skin treatments identified during ANOVA.

Table 12 Sources of variation, degree of freedom, and mean squares for the stratum corneum, epidermis/dermis composite, and full-thickness skin obtained from the analysis of variance (ANOVA) of microindentation results for human and porcine skin layers. Statistical significance (Sig) of each source of variation or interaction thereof is indicated by asterisks as per probability of F becomes significant (*P*<0.05*, *P*<0.01, *P*<0.001***).**

Source	df	Stratum Corneum			Epidermis/Dermis			Full-Thickness Skin		
		Mean Square	Sig[a]	*P* > F	Mean Square	Sig[a]	*P* > F	Mean Square	Sig[a]	*P* > F
Source	1	82186	***	<0.0001	13.28	*	0.0237	1.35		
State	1	8736	**	0.0052	20.65	**	0.0049	2.76		
Relative Humidity (RH)	1	66			1.11			0.98		
Source x State	1	47597	***	<0.0001	0.89			57.19	***	<0.0001
Source x RH	1	12898	***	0.0007	4.49			1.86		
State x RH	1	6087	*	0.0194	8.81		0.0649	2.00		
Source x State x RH	1	1819			0.65			5.01		0.0544
Error	248	1099			2.56			1.34		
CV%		33.43			87.10			63.83		

Table 13. Statistically significant interactions between treatments (skin source, state, and relative humidity) influencing the out-of-plane Young's modulus of skin layers determined by microindentation analysis at a 95% confidence interval (LSD=Least Significant Difference, SD=standard deviation; n=64).

Skin Layer	Source	State			
		Fresh	**SD**	**Frozen**	**SD**
Stratum Corneum	Human	124.91	41.48	109.33	40.84
	Porcine	61.81	18.01	100.76	30.78
	LSD	11.48			
	Source	**Relative Humidity**			
		35%	**SD**	**100%**	**SD**
	Human	123.71	44.38	110.53	38.13
	Porcine	73.67	30.28	88.89	31.75
	LSD	11.48			
	State	**Relative Humidity**			
		35%	**SD**	**100%**	**SD**
	Fresh	97.72	48.84	88.99	40.54
	Frozen	99.66	42.08	110.43	28.63
	LSD	11.48			
Epidermis/Dermis	**State**	**Relative Humidity**			
		35%	**SD**	**100%**	**SD**
	Fresh	1.67	1.4	1.43	1.02
	Frozen	1.87	1.11	2.37	2.47

Skin Layer	Source	State			
		Fresh	SD	Frozen	SD
	LSD	0.55			
Full-thickness	Source	State			
		Fresh	SD	Frozen	SD
	Human	1.31	0.73	2.46	1.36
	Porcine	2.11	1.46	1.37	0.94
	LSD	0.4			

Table 14. Sources of variation, degree of freedom, and mean squares for the stiffness (N m^{-1}), force at insertion (N), and displacement at insertion (µm) obtained from the analysis of variance (ANOVA) of microneedle insertion results for human and porcine skin layers. Statistical significance (Sig) of each source of variation or interaction thereof is indicated by asterisks as per probability of F becomes significant (*P*<0.05*, *P*<0.01, *P*<0.001***).**

Source	df	Stiffness			Force			Displacement		
		Mean Square	Sig[a]	*P* > F	Mean Square	Sig[a]	*P* > F	Mean Square	Sig[a]	*P* > F
Source	1	686.72	***	<0.0001	0.0041	***	0.0007	5944205	***	<0.0001
State	1	1079.73	***	<0.0001	0.0039	***	0.0009	1432205	***	<0.0001
Relative Humidity (RH)	1	129.65			0.0035	**	0.0017	3200332	***	<0.0001
Source x State	1	17.41			0.0019	*	0.0202	85328		
Source x RH	1	130.29			0.0010			177909		
State x RH	1	207.01			0.0070			198685		
Source x State x RH	1	91.43			0.0070			126803		
Error	120	38.42			0.0003			139799		
CV%		42.32			18.18			33.15		

Table 15. Statistically significant interactions between treatments (skin source, state, and relative humidity) influencing the force of microneedle insertion into skin determined by microneedle insertion profiling at a 95% confidence interval (LSD=Least Significant Difference, SD=standard deviation; n=8).

Source	**State**			
	Fresh	SD	Frozen	SD
Human	0.109	0.021	0.105	0.011
Porcine	0.105	0.027	0.086	0.01
LSD	0.006			

Appendix B – Skin Preparation and Testing Method in Chapter 3

B1 - Biological Skin Preparation

Skin samples were excised from the abdominal regions of abdominoplasty patients and pigs. The subcutaneous fatty tissue was removed from the skin. The skin areas were marked with known dimensions prior to excision from the subject. After excision, the skin samples were re-stretched to their original dimensions and further cut into smaller samples. These smaller samples were re-stretched and mounted on a flat substrate for mechanical testing and characterization.

The SC of some skin samples were separated (Figure 40) from the ED composite skin by a mild heat treatment of the FT skin specimen at 60^{o}C for 180 s inside a sealed plastic bag in a water bath [72, 130]. Upon separating the SC and the ED layers, they were stretched to their original dimensions, as described previously. The SC specimens used in tensile testing were pre-stretched and cut on the dissecting pad prior to testing. The thicknesses of all skin samples were measured using the Q400 TMA machine (TA Instruments, New Castle, DE, USA).

The stretched skin samples were tested under ambient RH condition in the testing laboratory, typically ranging between 33-38% RH (average ~ 35% RH), and at saturated moisture conditions (approximately 100% RH). The 100% RH condition was achieved by wetting the skin samples with water followed by incubation on a petri dish in a humid environment for at least 20 minutes. All skin samples were maintained at 20 ^{o}C prior to and during the mechano-analysis.

Figure 40. Sheets of human stratum cornea (*left*) separated from full-thickness skin specimens by mild heat treatment at 60 °C water bath for 180 s were re-stretched on flat rigid substrates (*right*).

B2 - Tensile Testing of the Stratum Corneum

The Q400 vertical tensile tester recorded the load-displacement data during the tensile test at a frequency of 10 Hz. For the tensile test, the SC layers were cut into 5 mm (width) × 8 mm (length) pieces using a stainless steel template. The SC film thicknesses varied between 10-40 μm. During tensile testing, the cross-sectional area of the SC layers changed as a function of applied force. To account for this change in cross-sectional area, true stress

$$\sigma_T = \sigma_i(1 + \varepsilon_i) \qquad (20).$$

and true strain values

$$\varepsilon_T = ln(1 + \varepsilon_i) \qquad (21)$$

were determined from given stress σ_i and strain ε_i values by using instantaneous values for the cross-sectional area, which led to more accurate measurements during tensile testing.

B3 - Statistical Analysis

Two-way ANOVA were performed to compare the following mechanical properties of different skin types (human, porcine, and artificial skin) at two RH conditions: Young's modulus, UTS, MN insertion force, displacement at insertion, and skin stiffness during insertion. The significance of the skin type and RH, and their interaction were declared when $P<0.05$ ($\alpha=0.05$). Multiple comparison t-tests were performed to determine the directional effects of significant differences between population means.

Appendix C – Methods and statistical data supporting Chapter 4

C1 - MATLAB Code for Image Processing

```
clear all
clc

% Video to Frames
a=VideoReader('video.avi');
numframes = a.NumberOfFrames;
% %%
% for img = 1:numframes;
%     filename=strcat('frame',num2str(img), '.jpg');
%     b=read(a,img);
%     imwrite (b, filename);
% end
%
% load handel;
% sound(y,Fs);

% Displacement Vector
% Calculation of displacement and velocity using binary pixel change in
% cropped images acquired.

pixelspermm = 52; % estimated

for    img = 1:numframes;
    filename=strcat('frame', num2str(img), '.jpg');
    gr = imread (filename);
    bw = im2bw(gr, 0.25);
    bwcrop = bw(1:100,1:10); % Adjust the column strip here (row numbers,
column numbers)
    mean_pix(img,:) = mean(numel(bwcrop(:, 1)) - sum(bwcrop, 1)); % Total
Black Pix = Total Pix - Total White Pix
    mean_mm(img,:) = mean_pix(img,:)/pixelspermm;
end

% Time and Velocity Vectors
fps = 10000; %frames per second for video (for .cine, not .avi)
time_vec_disp = (1:numframes)/fps;

% Force Vector
% Averaging and plotting force data
filename = 'data.xlsx'; %list your excel file
data = xlsread(filename);
frequency = 100000; % frequency of data collection;
ratio = frequency/fps;

force_data_required = (ratio)*numframes;% determine how many force samples
per displacement value
force = data(1:force_data_required,2); % select the column corresponding to
force data (i.e., 2)
```

```
% force = data(1:end,2);
time_vec_force = (1:numel(force))/frequency;%a time vector to represent the
number of mean data points

% Extrapolated Matrices
%Combine Time, Displacement, Velocity, and Force data into one matrix
%Intrapolate displacement data to match the frequency of force data
mean_mmi = interp1(time_vec_disp, mean_mm, time_vec_force, 'pchip');

%Velocity calculation
velocity = diff(mean_mmi)./diff(time_vec_force);
velocity(end+1) = velocity(end); % added an addition point to the velocity
vector to make it equal in length to other vectors



% Max points
[M, idx_disp] = max(abs(mean_mmi));
% [M, idx_vel] = max(abs(velocity));
[M, idx_force] = max(abs(force));
time_max_disp = time_vec_force(idx_disp);
% time_max_vel = time_vec_force (idx_disp);
time_max_force = time_vec_force (idx_force);

% finding starting index point based on min value
norm_force = force(1:idx_force)/max(force);
inverse_force = 1-norm_force;
[pks, peakLoc] = findpeaks(inverse_force,'MinPeakHeight',0.9);
start_idx= peakLoc(end);

% find starting point and crop vectors
mean_mmi_cropped = mean_mmi(start_idx:end);
disp_cropped = mean_mmi_cropped - mean_mmi_cropped(1);
velocity_cropped = velocity(start_idx:end);
force_cropped = force(start_idx:end);
time_cropped = time_vec_force(start_idx:end);
time_cropped = time_cropped - time_cropped(1); %zero time vector
velocity = diff(disp_cropped)./diff(time_cropped);
velocity(end+1) = velocity(end);

% Energy calculations
mass_g = 7;
mass_kg = mass_g/1000;%kg mass of moving object
velocity_m = velocity/1000;
v2 = power(velocity_m,2);
mass_v2 = (mass_kg)*(v2);
KE = 0.5*(mass_v2);

spring_ext_mm = disp_cropped(end) - disp_cropped;
spring_ext_m = spring_ext_mm/1000;
spring_ext2 = power(spring_ext_m, 2);
spring_constant = 485; %spring constant in N/m
constant_ext2 = spring_constant*spring_ext2;
```

```
PE = 0.5*(constant_ext2);

% Figures
figure(1); clf reset;
subplot(4,1,1);
plot(time_cropped, force_cropped, 'x-b', 'linewidth', 2); hold on;
xlim([0 0.004]); xlabel({'Time', '(s)'}); ylabel ({'Force', '(N)'});

subplot(4,1,2);
plot(time_cropped, disp_cropped, 'x-r', 'linewidth', 2); hold on;
xlim([0 0.004]);xlabel({'Time', '(s)'}); ylabel ({'Displacement', '(mm)'});

subplot(4,1,3);
plot(time_cropped, velocity, 'x-k', 'linewidth', 2); hold on;
xlim([0 0.004]); xlabel({'Time', '(s)'}); ylabel ({'Velocity', '(m/s)'});

subplot(4,1,4);
plot(time_cropped, KE, '*-k', 'linewidth', 2); hold on;
xlim([0 0.004]); xlabel({'Time', '(s)'}); ylabel ({'Kinetic Energy', '(J)'});

% figure(2); clf reset;
% [hAx, hLine1, hLine2] = plotyy(time_cropped, KE,time_cropped, PE);
% title ('Energy Balance');
% xlim([0 0.01]); xlabel({'Time', '(s)'});
% % ylabel(hAx(1),'Kinetic Energy', '(J)');
% % ylabel(hAx(2), 'Potential Energy', '(J)');

% make a matrix *i.e. table with cols: time, mena_mmi, force, velocity
combined_table = horzcat(time_cropped(:), force_cropped(:), disp_cropped(:),
velocity(:), KE(:), PE(:));
table_data = table(time_cropped(:), force_cropped(:), disp_cropped(:),
velocity(:), KE(:), PE(:));
writetable(table_data,'test_table_data.xlsx')


figure(2);
subplot(2,1,1);
plot(time_vec_force, mean_mmi, '*-k', 'linewidth', 2); hold on;
xlabel({'Time', '(s)'}); ylabel ({'Displacement', '(mm)'});
subplot(2,1,2);
plot(time_vec_force, force, '*r', 'linewidth', 2); hold on;
xlabel({'Time', '(s)'}); ylabel ({'Force', '(N)'});

new_table = horzcat(time_vec_force(:), mean_mmi(:), force(:));
table_data_2 = table(time_vec_force(:), mean_mmi(:), force(:));
writetable(table_data_2,'test_table_data_2.xlsx');
```

C2 - Statistical Analysis

The following tables provide the ANOVA results from dynamic MN insertions.

Table 16. Assessment of the microneedle tip outer diameter and energy on force of insertion (F_{ins}) and energy to insert (E_{ins}). Sources of variance and degrees of freedom for F_{ins} and E_{ins} as obtained from the analysis of variance. Single microneedles were used to assess the impact of the tip outer diameter (60, 100, and 120 µm), and the total energy (E_o=0, 20 and 53 mJ) using a 3 x 3 factorial design. The significance at the probability of p<0.05, 0.01 and 0.001 are indicated by *, ** and * indicate, respectively.**

Source of Variance	df	F_{ins}	E_{ins}
Tip outer diameter	2	0.5334***	1.33×10^{-8} ***
E_o (J)	2	0.455***	8.16×10^{-9} ***
Tip outer diameter x E_o (J)	2	0.058***	2.20×10^{-9} **
Error	18	0.0025	3.20×10^{-10}
CV%		13.07	38.57

Table 17. Assessment of the impact of microneedle projections and energy on force of insertion (F_{ins}) and energy to insert (E_{ins}). Sources of variance and degrees of freedom for F_{ins} and energy to insert E_{ins} as obtained from the analysis of variance. Microneedles with a tip outer diameter of 100 µm was used to assess the impact of the number of microneedles (1, 6, and 19) in an array, and the total energy (E_o=20 and 53 mJ) using a 3 x 2 factorial design. The significance at the probability of p<0.05, 0.01 and 0.001 are indicated by *, ** and * indicate, respectively.**

Source of Variance	df	F_{ins}	E_{ins}
Number of projections	2	176.324***	4.41×10^{-6} ***
E_o (J)	1	35.913***	4.31×10^{-6}***
Number of projections x E_o (J)	2	7.2***	1.28×10^{-6}***
Error	18	0.287	5.00×10^{-8}
CV%		11.73	30.75

Appendix D – Optimization of Microneedle-Optofluidic Biosensor Supporting Chapter 7

Optimization of the detection chamber/optical waveguide dimensions (channel length and width) using diode laser input light and methyl green dye (model dye for TMB end-product, absorbing at 635 nm) showed a linear relationship between the absorbance and the channel length independent of the channel width (Figure 41A). Figure 41B demonstrates the impact of blocking the AcKAA-functionalized surface with BSA to prevent non-specific binding of VAN-HRP at a concentration of 0.70 µM. The waveguide with 5 mm length and 50 µm width dimensions provided an absorbance measurement of over 1 AU within the observed linear calibration range for a typical TMB end-product. Beyond ~1.3 AU and ~5 mm channel length, absorbance values deviated from the linear range of the waveguide dimensions.

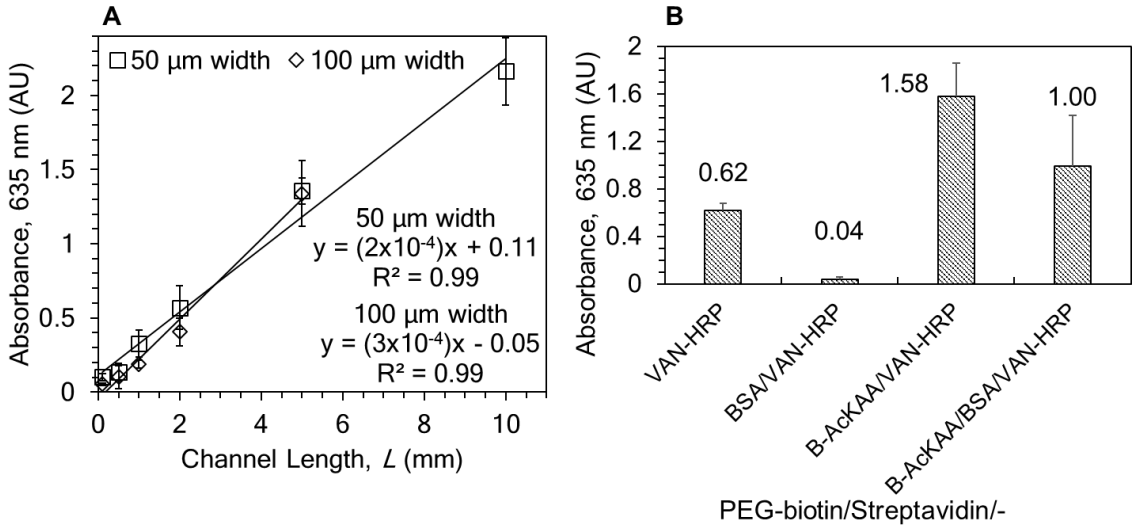

Figure 41. Absorbance of the TMB model-dye (methyl green) in the optofluidic sensing system as a function of optical waveguide length (0.1-10 mm) and width (50-100 µm) (A); and absorbance of the TMB end-product at 635 nm due to Vancomycin-HRP (VAN-HRP) activity at 0.7 µM in the microneedle base surfaces where bovine serum albumin (BSA) was used for surface blocking to prevent non-specific binding of VAN-HRP (B). For all measurements, n = 4 and error bars represent standard deviations.